CHARACTERIZATION AND DESIGN OF EMBEDDED PASSIVE CIRCUITS FOR APPLICATIONS UP TO MILLIMETER-WAVE FREQUENCY

A Dissertation
Presented to
The Academic Faculty

By

Seunghyun Eddy Hwang

In Partial Fulfillment
of the Requirements for the Degree
Doctor of Philosophy in the
School of Electrical and Computer Engineering

Georgia Institute of Technology
August 2011

CHARACTERIZATION AND DESIGN OF EMBEDDED PASSIVE CIRCUITS FOR APPLICATIONS UP TO MILLIMETER-WAVE FREQUENCY

Approved by:

Dr. Madhavan Swaminathan, Advisor
School of Electrical and Computer Engineering
Georgia Institute of Technology

Dr. John Papapolymerou
School of Electrical and Computer Engineering
Georgia Institute of Technology

Dr. Kevin Kornegay
School of Electrical and Computer Engineering
Georgia Institute of Technology

Dr. Bruno Frazier
School of Electrical and Computer Engineering
Georgia Institute of Technology

Dr. Suresh K. Sitaraman
School of Mechanical Engineering
Georgia Institute of Technology

Date Approved: [June 15, 2011]

Dedicated to

my father, Kijun Hwang
my mother, Heaok Hong
my wife, Yeonji No
and
my family
for their endless love

ACKNOWLEDGEMENTS

I would like to express my sincere appreciation to the people who have helped and inspired me during four years of my Ph.D. research in Georgia Tech. First, I would like to thank my academic advisor, Dr. Madhavan Swaminathan, for giving me an invaluable opportunity to work in *Mixed Signal Design* Group. I was very fortunate to start my graduate research under his discipline. Through his rigorous background and insight, my research could be directed in the right way. I cannot thank my professor enough for his continuous support, trust, encouragement, and guidance.

I would like to thank my committee members Prof. John Papapolymerou, Prof. Kevin Kornegay, Prof. Bruno Frazier, and Prof. Suresh Sitaraman for taking their invaluable time to give me important advices and comments. I owe special thanks to Prof. John Papapolymerou. Without his microwave class, a direction of my research would have been lost.

I will be always grateful to be in my *Mixed Signal Design* Group. I give my thanks to Dr. Wansuk Yun, Dr. Tae Hong Kim, Dr. Subramanian Lalgudi, Dr. Krishna Bharath, Dr. Ki Jin Han, Dr. Nevin Altunyurt, Vishal Laddha, Dr. Nithya Sankaran, Dr. Narayanan Terizhandur, Tapo Bandhopadyay, Janani Chandrashekar, Dr. Krishna Srinivasan, Ranjeeth Doppalapudi, Sukruth Pattanagiri, Aswani Kurra, Dr. Abhilash Goyal, and Beranard Yang. Especially, I would like to thank Nevin and Wansuk for guiding me to the microwave design area during the first year of my research. My special thanks go to Ki Jin who gave me invaluable discussions on my research ideas. I would also like to thank Myunghyun Ha, Suzanne Huh, and Jae Young Choi who joined Tech same year as me and endured hard time during preliminary examination period. I also wish all the best for new students and their friendship: Jianyong Xie, Kyuhwan Han, Satyan Telikepalli, and Biancun Xie.

The research faculty of my group has also been great supporters for all of us and I would like to thank Dr. Ege Engin, Dr. Sunghwan Min, Dr. Daehyun Chung and Dr. Andy Seo. I can never thank enough to Dr. Min who provided me so many guidance including filter design as well as journal writing techniques.

I also would like to acknowledge PRC people who fabricate my designs: Hunter Chan, Dr. Venky Sundaram, Vivek Sridharan, and Prof. Rao Tummala. I would like to thank *SAMEER* Engineers: Dr. Venkatesan Venkatakrishnan, K. Suresh, and Venkatesh Chelukkaramdas for collaborating material characterization work. I would like to express my gratitude to Dr. Benjamin Lacroix for collaborating millimeter-wave projects and providing good measurement data. I am also grateful to Sehun Kook and Hyunwoo Choi for fun times we shared as a lab neighbor. I am indebted to Dr. Yoonsu Choi for encouraging me to contact Prof. Swaminathan when I was looking for an academic advisor.

Finally, I am heartily thankful to my family and would like to give my sincere thank to my family. Every journey and accomplishments from Seattle to Atlanta has been realized and supported by my parent. My father, Dr. Kijun Hwang who sacrificed his career to provide me the best environment, showed me things that nobody can teach. His bright insight and wisdom always directed me to the right path while he gave me unconditional love whenever I needed. My positive attitude comes from my mother, Mrs. Heaok Hong who gave me endless love. Without my mom’s support, I could have not obtained my degree. I truly appreciate all the pray and love from sister, grandfather, and grandmother as well. I also would like to thank my father-in-law and mother-in-law for their kindness and thoughtful concern. Lastly, but not the least, I want to give special thanks to my dear wife, Yeonji No, for her endless love and support. Along with completing my Ph.D. degree, meeting her was the best present that Georgia Tech gave me. If I did not meet her, my life at Tech would have been miserable because she gave me joy and energy to survive everyday hardworking.

TABLE OF CONTENTS

ACKNOWLEDGEMENTS iv

LIST OF TABLES x

LIST OF FIGURES xi

SUMMARY xviii

CHAPTER 1 INTRODUCTION 1
- 1.1 Platforms for System Integration Technology 2
- 1.2 Material Characterization Methods 9
- 1.3 Filter Integration and Performance Problems 11
- 1.4 Completed Research 15
- 1.5 Dissertation Outline 19

CHAPTER 2 MATERIAL CHARACTERIZATION 20
- 2.1 Material Characterization Technique 22
  - 2.1.1 Cavity Resonator with Corner-to-Corner Probing Method 22
  - 2.1.2 Automated Extraction Modeling and Algorithm 25
  - 2.1.3 Inclusion of Surface Roughness Effect 30
  - 2.1.4 Extraction of Dielectric Thickness 34
- 2.2 Material Characterization Results up to Millimeter-Wave 36
  - 2.2.1 Extraction of RXP Material Properties up to 110 GHz 36
  - 2.2.2 Development of Causal Model 43
  - 2.2.3 Extraction of Ceramic Material Property up to 67 GHz 45
  - 2.2.4 Extraction of High-Loss Material Property up to 67 GHz 52
- 2.3 Summary 58

CHAPTER 3 EMBEDDED WLAN BANDPASS FILTERS 61
3.1 High-Rejection Bandpass Filter Topologies 64
3.1.1 Narrow-Band Bandpass Filter Topology 64
3.1.2 Wide-Band Bandpass Filter Topology 68
3.2 Filter Design Methodology and RXP Stack-Up 74
3.3 3D Stitched Capacitor 76
3.4 WLAN Bandpass Filter 79
3.4.1 Design of High-Rejection Second-Order WLAN Bandpass Filters 79
3.4.2 Miniaturization of High-Rejection Second-Order WLAN Bandpass Filters. 84
3.4.3 Design of High-Order WLAN Bandpass Filters 88
3.5 Summary 94

CHAPTER 4 DUAL-BAND BANDPASS FILTERS AND DUPLEXER IN RXP SUBSTRATE 97
4.1 Drawbacks of Dual-Band Filters using Transmission Line Based Method 99
4.2 Miniaturized Lumped-Element Dual-Band Bandpass Filter 102
4.3 High-Rejection WLAN Duplexer in RXP 113
4.4 Summary 119

CHAPTER 5 LUMPED-ELEMENT CIRCUITS AT MILLIMETER-WAVE FREQUENCY 120
5.1 Limitation of Self-Resonant Frequency 122
5.2 Realization of 60 GHz Lumped-Element Bandpass Filter 125
5.3 Realization of 60 GHz Lumped-Element Dual-Band Bandpass Filter 130
5.4 Design of 60 GHz Duplexer 137
5.5 Summary 139

CHAPTER 6 FILTER DESIGN IN SILICON INTERPOSER USING THROUGH-SILICON VIA (TSV) TECHNOLOGY 140
6.1 Effect of Substrate Loss on Conventional Filter Design 142
6.2 Filter Design in High-Loss Substrate 145
6.3 Validation using FR4 Substrate on PCB 148
6.4 RF Characteristics of Through-Silicon Via (TSV) 152
6.5 Filter Design in Silicon Interposer using TSV 156

6.6 Summary 159

CHAPTER 7 CONCLUSIONS 161
7.1 Contributions 162
7.2 Future Work 163
7.3 Publications 164
7.3.1 Refereed Journal Articles 164
7.3.2 Conference Papers 165
7.3.3 Invention Disclosure 166

APPENDIX 167

REFERENCES 168

VITA 177

LIST OF TABLES

Table 1. Comparison of system integration platforms. 8

Table 2. Frequency bands of wireless standards. 12

Table 3. Physical dimensions of resonators. 36

Table 4. Difference between extracted values and vendor. 42

Table 5. Measured parasitics and capacitances @ 2 GHz. 79

Table 6. Performance summary of measured RXP filters. 95

Table 7. Design rule for six-metal layer RXP substrate. 108

LIST OF FIGURES

Figure 1. Circuit board of populated cellphone. 3

Figure 2. A platform for system integration [5].. 3

Figure 3. Comparison of discrete versus embedded passives.. 4

Figure 4. Flexible RXP coupon and cross section of RXP substrate................................. 7

Figure 5. Block diagram of RF circuit in cellphone. 12

Figure 6. Cavity resonator. (a) Top view. (b) Side view. 22

Figure 7. Frequency response of the resonator. 23

Figure 8. Corner-to-corner probing method... 24

Figure 9. (a) Unit cell model of a single plane pair. (b) Electrical model of FDM [63]... 25

Figure 10. Flow chart of extraction process... 28

Figure 11. Correlation result from narrow-band simulation.. 28

Figure 12. Simulation result for the sensitivity of unit cell size. 29

Figure 13. Surface roughness measurement. (a) RXP1. (b) RXP4.................................. 31

Figure 14. Frequency-dependent conductivity for RXP1 and RXP4. 32

Figure 15. Surface roughness effect on RXP1. (a) Dielectric constant. (b) Loss tangent. 33

Figure 16. Thickness estimation and measured thickness. (a) Correlation for RXP1. (b) Correlation for RXP4. (c) Measured cross-section for RXP1. (d) Measured cross-section for RXP4. 35

Figure 17. Measured transfer impedance (Z_{12}). (a) 32.5mm resonator with RXP1. (b) 9.5mm resonator with RXP1. (c) 6.5mm resonator with RXP4. (d) 4.5mm resonator with RXP4. 37

Figure 18. Correlation result from microwave to millimeter-wave frequency. 38

Figure 19. RXP1 extracted results. (a) Dielectric constant. (b) Loss tangent. 40

Figure 20. RXP4 extracted results. (a) Dielectric constant. (b) Loss tangent. 41

Figure 21. Causal model with extracted results. (a) Dielectric constant. (b) Loss tangent. 44

Figure 22. Layout of the parallel-plate resonators for ceramic material. 46

Figure 23. Fabricated resonators on ceramic substrate. 47

Figure 24. Ceramic surface roughness measurement. 47

Figure 25. Measured return loss of four samples from (a) resonator 1 and (b) resonator 3. 48

Figure 26. Extracted dielectric constants. (a) Sample1 (b) Sample2 (c) Sample3 (d) Sample4 50

Figure 27. Extracted loss tangents. (a) Sample1 (b) Sample2 (c) Sample3 (d) Sample4 51

Figure 28. The resonator layout for high-loss material. 52

Figure 29. Corner-to-corner probing. 53

Figure 30. Comparison between resonator 1 and resonator 3. 54

Figure 31. Measured transfer impedance of resonator 1 from two samples. 54

Figure 32. Measured return loss of resonator 5 from two samples. 55

Figure 33. High-loss material extraction results from sample1. (a) Dielectric constant (b) Loss tangent 56

Figure 34. High-loss material extraction results from sample2. (a) Dielectric constant (b) Loss tangent ... 57

Figure 35. Material property of LCP and RXP up to 110 GHz: (a) dielectric constant, and (b) loss tangent. (Green: RXP1, blue:RXP4, red: LCP [24]) ... 59

Figure 36. Embedded passive and active module using RXP. ... 62

Figure 37. (a) Conventional capacitively-coupled topology. (b) Frequency response. ... 65

Figure 38. (a) Modified topology with grounding inductor. (b) Frequency response. ... 65

Figure 39. Equivalent circuit for modified topology. ... 66

Figure 40. (a) Unique resonator with grounding inductor. (b) Its equivalent circuit. ... 69

Figure 41. Filter response in S-parameters. ... 72

Figure 42. Location of transmission zeros and passband from Z-parameter of filter response. ... 73

Figure 43. Cross section of RXP organic material. ... 75

Figure 44. (a) Parallel-plate capacitor and (b) stitched capacitor. ... 76

Figure 45. Pi model of two-port equivalent circuit model. ... 77

Figure 46. Parallel-plate and stitched capacitors. ... 78

Figure 47. Fabricated RXP panel and 2 and 5 GHz BPFs images. ... 80

Figure 48. Physical layout of type1 (a) 2 GHz BPF and (b) 5 GHz BPF. ... 81

Figure 49. Measurement equipment with GSG probes. ... 82

Figure 50. Measured frequency response from VNA. ... 82

Figure 51. Measured results for type1 (a) 2 GHz and (b) 5 GHz BPFs. ... 83

Figure 52. Physical layout of type2 (a) 2 GHz and (b) 5 GHz BPFs. ... 85

Figure 53. Measured results for type2 (a) 2 GHz and (b) 5 GHz BPFs. 87

Figure 54. Proposed third-order BPF schematic. 88

Figure 55. BPF responses. (a) Without additional elements. (b) With L2 and L4. (c) With L2, L4, and L5. 89

Figure 56. Layout of type3 5 GHz filter. 91

Figure 57. Fabricated 5 GHz 3rd order BPF. 91

Figure 58. Measured result for type3 5 GHz BPF. 92

Figure 59. Layout of type3 2 GHz BPF. 93

Figure 60. Measured result for type3 2 GHz BPF. 93

Figure 61. Multi-chip embedded SoP module. 98

Figure 62. Maximum bandwidth ratio vs center frequency ratio [80]. 100

Figure 63. Proposed dual-band topology. 103

Figure 64. (a) low-passband schematic and (b) its frequency response for low-passband. 104

Figure 65. Single modified resonator and its frequency response for high passband. 106

Figure 66. Six-metal layer RXP stack-up. 108

Figure 67. Physical layout of dual-band bandpass filter. 109

Figure 68. Dimension of the layout from metal layer two to four. 109

Figure 69. X-ray photo of the dual-band bandpass filter. 110

Figure 70. Measured and simulated result for dual-band filter A. 111

Figure 71. Measured and simulated result for dual-band filter B. 111

Figure 72. Measured and simulated result for dual-band filter C. 112

Figure 73. Block diagram of the proposed dual-band module 113

Figure 74. Size reduction for high-rejection 2.4 GHz BPF. 114

Figure 75. Size reduction for third-order 5 GHz BPF. 115

Figure 76. Matching circuit schematic in ADS. 116

Figure 77. Physical layout of duplexer A. 117

Figure 78. Correlation result of duplexer A. 117

Figure 79. Physical layout of duplexer B 118

Figure 80. Correlation result of duplexer B. 118

Figure 81. Conceptual integration techniques for RXP technology (a) A separate substrate passive components. (b) Chip embedded in a cavity. 121

Figure 82. π-equivalent circuit model 123

Figure 83. Inductance from 1 GHz to 160 GHz 124

Figure 84. Capacitance from 1 GHz to 160 GHz 125

Figure 85. 60 GHz bandpass filter circuit schematic. 126

Figure 86. Simulation result of 60 GHz BPF in circuit simulator. 127

Figure 87. Physical layout of 60 GHz BPF 128

Figure 88. 60 GHz BPF response in EM simulator. 128

Figure 89. Fabricated 60 GHz BPF 129

Figure 90. 60 GHz BPF measurement correlation. 130

Figure 91. 60 GHz dual-band BPF topology. 131

Figure 92. Simulation result of 60 GHz dual-band BPF in circuit simulator. 131

Figure 93. Six metal-layer RXP stack-up. 132

Figure 94. Physical layout of 60 GHz dual-band BPF 133

Figure 95. Dimensions of layout from M1 to M2. 134

Figure 96. Frequency response of 60 GHz dual-band BPF in EM simulator. 134

Figure 97. Fabricated 60 GHz dual-band BPF 135

Figure 98. Correlation result with measurement 136

Figure 99. Screen shot of VNA for dual-band 60 GHz BPF. 137

Figure 100. Layout of 60 GHz duplexer. 138

Figure 101. Simulated response of 60 GHz duplexer. 138

Figure 102. Roadmap of package technology 141

Figure 103. Simulation result of edge-coupled bandpass filter. 142

Figure 104. Conventional filter topology with dielectric loss. 143

Figure 105. Effect of dielectric loss on filter performance. (a) High-loss L (b) High-loss C (c) High-loss L&C (d) Low-loss L (e) Low-loss C (f) Low-loss L&C 145

Figure 106. Filter response in terms of capacitor. 146

Figure 107. Wideband bandpass response using a capacitor. 147

Figure 108. (a) Physical layout and (b) measured result of UWB FR4 filter. 150

Figure 109. (a) Physical layout and (b) measured result of FR4 bandpass filter. 151

Figure 110. Geometry of simulated vias. 152

Figure 111. (a) S31 (IL) and (b) S21 (NEXT) of conventional vias and TSVs. 153

Figure 112. Model equivalent circuit of two TSVs [94]. 154

Figure 113. TSV coupling by varying oxide thickness and silicon conductivity. 155

Figure 114. Simulation result of UWB filter in silicon interposer. (a) Filter response and (b) physical layout. 157

Figure 115. Highpass filter using TSV coupling. (a) 8.5 GHz cutoff frequency (b) 27 GHz cutoff frequency. 157

Figure 116. High-rejection highpass filter by TSV. 158

Figure 117. Bandpass response in 60 GHz by TSV. 159

Figure 118. VNA screen shots of (a) UWB and (b) via as an inductor FR4 filters. 167

SUMMARY

The goal of the research in this dissertation is to develop techniques for 1) system-on-package integration of passive circuits using ultra-thin advanced polymers called RXP (Rogers experimental polymer), 2) extraction of frequency-dependent material properties up to millimeter-wave frequency, 3) development and synthesis of high-rejection filter topologies, 4) design and characterization of high performance miniaturized embedded passive circuits for microwave and millimeter-wave applications, and 5) development of via and through-silicon via (TSV) enhanced filter design method for integration in high-loss substrate.

The RXP material is developed to reduce the layer-count for multi-layer configuration and adoption of advanced fabrication technologies, hence reducing the overall system size for enabling thinner and smaller wireless modules. Frequency-dependent material properties of RXP, ceramic, and other materials have been extracted up to millimeter-wave frequency using parallel-plate resonator method. An automated extraction algorithm has been proposed to handle a large number of frequency samples efficiently. The accuracy of the extraction result has been improved by including the surface roughness effect for conductor operating at high frequency.

Using extracted RXP material properties, 2.4/5 GHz WLAN bandpass filters have been designed and characterized. High-rejection bandpass filter topologies for narrow 2.4 GHz and wide 5 GHz have been proposed. The proposed topologies have been synthesized to provide design equations as well as graphical design methodologies using Z-parameters. A new capacitor design called 3D stitched capacitor has been proposed to

achieve more symmetric layout by providing balanced shunt parasitics. The proposed topologies and design methodologies have been verified through the measurement of high-rejection RXP bandpass filters. Good correlation between the simulation and measurement was observed demonstrating an effective design methodology and embedding bandpass filters with good performance.

Dual-band bandpass filters for WLAN applications have been implemented and measured. Instead of connecting two bandpass filter circuits, a new single bandpass filter topology has been developed with a compact size as well as high isolation between passbands. High-rejection duplexer has been designed in RXP substrate for chip-last embedded IC technology, and a novel matching circuit has been applied for the miniaturization as well.

The 60 GHz V-band has special interest for wireless applications because of its high attenuation characteristics because of atmospheric oxygen. Millimeter-wave passive circuits such as bandpass filter, dual-band filter, and duplexer have been designed, and self-resonant frequency of passive components has been carefully avoided using the proposed method.

For low-cost system integration, silicon interposer with through-silicon-via (TSV) technology has been studied. The filter design method for high-loss substrate has been proposed. The coupling characteristic of TSV has been investigated for obtaining good insertion loss in lossy substrates such as silicon, and TSV characteristics has been used to design bandpass and highpass filters. To demonstration of concept, bandpass filters with good insertion loss have been realized on high-loss FR4 substrate.

CHAPTER 1

INTRODUCTION

High performance, low cost, and compact size combined with increasing system complexity have brought the need for high levels of integration in wireless applications. System-on-package (SoP) has been used as a solution for supporting the convergence of multiple microwave front-end modules by providing more functionality in the package through integration of passive components. Embedded passive technology is a key enabling technology for high levels of system integration in SoP. This technology requires advanced fabrication techniques and substrate materials to satisfy very demanding performance requirements.

Low temperature co-fired ceramic (LTCC) technology has allowed the fabrication and integration of three-dimensional circuits. Although LTCC technology has lower loss at high frequencies and lower coefficient of thermal expansion (CTE) than FR4, LTCC technology provides limited integration capability and higher cost as compared to a polymer based solution. As an alternative to LTCC technology, a polymer material that has become popular is liquid crystalline polymer (LCP), which has low loss, and is compatible with PCB manufacturing processes. However, a relatively higher processing temperature than FR4 and manufacturing variation issues because of the bondply material misalignment are still bottlenecks for the persuasive adoption of LCP technology. Recently, a new dielectric material called RXP (Rogers experimental polymer) which can be a replacement for LCP as an ultra-thin substrate in wireless applications has been introduced.

The goal of this research is to realize high-performance miniaturized embedded passive circuits for applications from RF to millimeter-wave frequencies using RXP technology. As an introductory discussion, this chapter explains the basic background in this dissertation. Section 1.1 provides the overview of current SoP technologies and the comparison with RXP technology. Section 1.2 emphasizes the need for frequency-dependent material property extraction and discusses previous approaches for material characterization. Section 1.3 addresses filter integration and performance issues and clarifies the limitations of previous filter designs. Then, the last two sections introduce the completed research and provide an outline of the dissertation.

1.1 Platforms for System Integration Technology

The increasing speed, functionality, and portability in consumer electronics have been putting tremendous pressure to include more circuits and passive components into the integration of systems. In almost every electronic product, the passive components including inductors, capacitors, and filters occupy a majority of area as well as limit overall device performances. In mobile products, for example, 90 % of the system components correspond to passives, which typically add up to some 400 discrete passive components and their metal interconnections on the substrate as shown in Figure 1 [1, 2]. Therefore, the miniaturization of the passives and the improvement of their performance are important driving forces for next generation electronics.

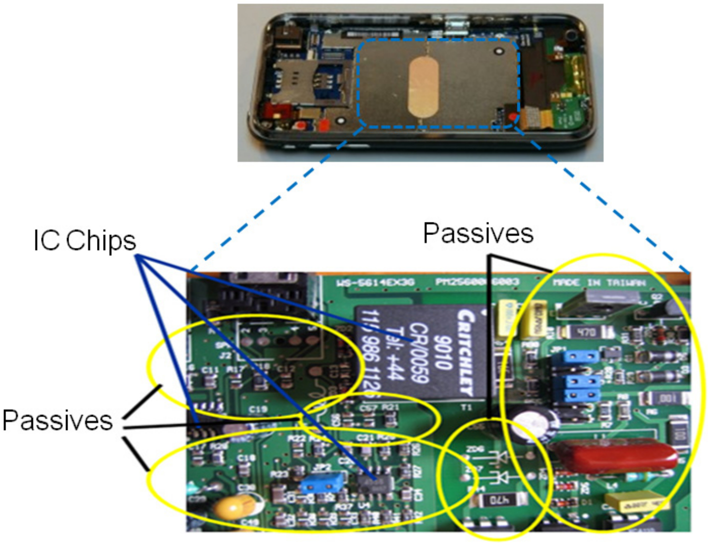

Figure 1. Circuit board of populated cellphone.

Multimedia systems have dramatically evolved using innovative system integration technologies such as system-on-chip (SoC), system-in-package (SiP), and system-on-package (SoP) [3, 4] as shown in Figure 2.

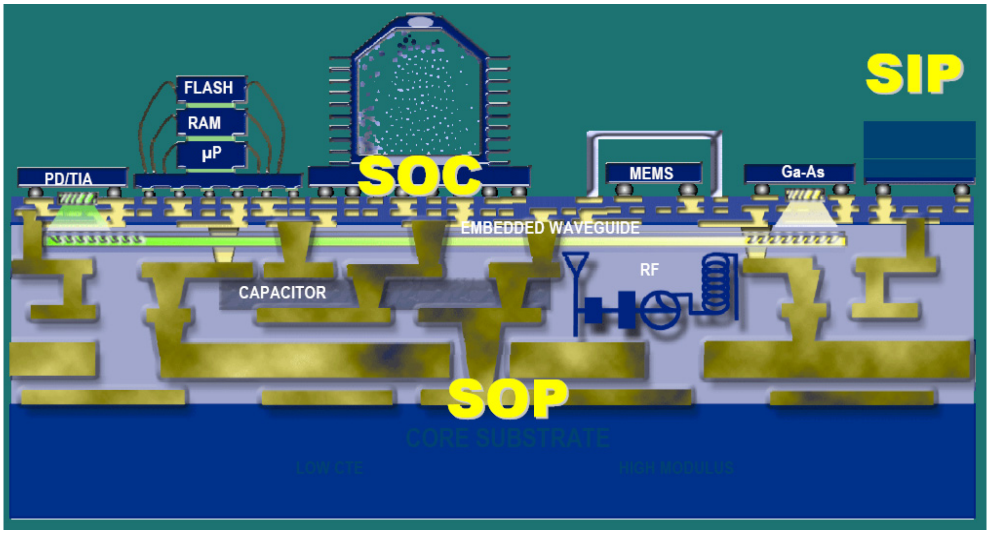

Figure 2. A platform for system integration [5].

These integration technologies continue to provide thinner and smaller form factor, lower cost, more functionality, and lower power consumption for next generation mobile applications. The SoC approach has provided a system-integration platform on a semiconductor chip. However, SoC based on the low-cost silicon substrate has suffered from passive integration of high quality inductors and filters because of poor substrate isolation and high silicon substrate losses [6]. As an alternative solution, RF front-end devices have been integrated into low-loss compound semiconductor substrates [7]. However, they are not a cost effective system solution because of the large area restricted for passive components [8]. As shown in Figure 3, the discrete-passives based on the SoC approach is thicker and bulkier than the embedded-passive device [9]. Therefore, a system-integration solution integrating multiple active dies and surface-mounted passive devices into a package called system-on-package (SoP) has been developed and commercialized on the last two decades. It has been found that the SoP approach provides better system integration capabilities with better RF performances compared to SoC and SiP using high performance passives embedded in a low-loss organic substrate [10].

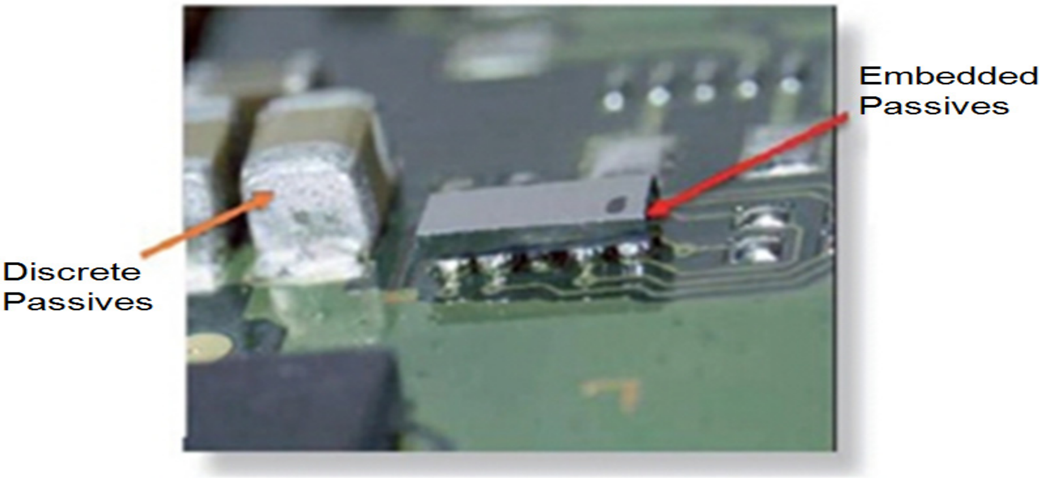

Figure 3. Comparison of discrete versus embedded passives.

In SoP, low temperature co-fired ceramic (LTCC) technology having high dielectric constant and low loss has provided system integration solutions for microwave and millimeter-wave applications [11-23]. However, LTCC technology may not necessarily provide a long-term effective packaging solution because of difficulty of embedding actives, thicker substrate, higher processing temperature (>900°C), larger weight, and higher cost as compared to organic technologies. Moreover, LTCC has a wide line-width, line to line spacing limitation, a small panel processing area, and high metal roughness. These barriers led to the development of organic-based SoP solutions [8, 10, 24-36].

Over the last few years, liquid crystal polymer (LCP) organic-based SoP technology has been considered as a promising candidate for system integration in a package because of its superior electrical properties up to millimeter-wave frequencies [24]. LCP (Ultralam 3850) is a laminate-type organic dielectric material that can be stacked to form multilayer substrates with the use of adhesive bondply layers (Ultralam 3908) in between stacked LCP layers. In addition to being a low-cost dielectric for a large panel area fabrication process, LCP has a combination of good electrical and mechanical properties. LCP has a low dielectric constant of 2.95 and a low loss-tangent of 0.002 up to millimeter wave frequencies. LCP also has favorable mechanical properties such as mechanical flexibility, a low coefficient of thermal expansion, and low moisture absorption. Furthermore, LCP has the mechanical strength to be the final printed wiring board (PWB), making it an excellent packaging substrate for SoP applications. In spite of the good RF performance and integration capability of LCP, LCP technology suffers from a few limitations because of relatively high processing temperature (290°C) compared to FR-4, which is a bottleneck for low-cost system integration. Additionally, the need for the bondply material for building stack-ups results in fabrication limitations because of the misalignment between the layers.

According to [37], the new ultra-slim NAND flash memory chip can be as thin as 0.6 mm, which is smaller than the thickness of typical LTCC substrates. To avoid a situation where the overall thickness of wireless products relies on the passive thickness rather than the chip thickness, an ultra-thin new substrate for SoP technology is required. Recently, ultra-thin organic low-K and low-loss dielectric called RXP has been developed and characterized to reduce layer counts and eliminate build-up layer processes in order to significantly reduce the substrate cost and improve fabrication limitations [38-44]. Unlike LTCC or LCP technologies, RXP can be made ultra-thin under low processing temperature (220°C), which is compatible with standard printed circuit board manufacturing processes. In [38], high Q embedded inductors have been developed in the core dielectric material (RXP1). In addition, a thin build-up dielectric material (RXP4) has been successfully developed with a fine line and low CTE capability [42]. As shown in Figure 4, embedded passives with a total thickness of less than 0.2 mm have been constructed using a combination of flexible RXP1 and RXP4 materials, which can embed actives with mixed signal (digital and RF) ICs.

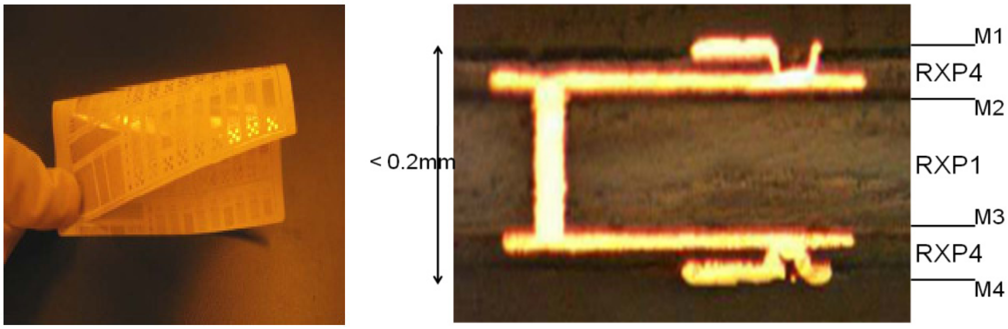

Figure 4. Flexible RXP coupon and cross section of RXP substrate.

RXP1 is made by a glass reinforced hydrocarbon polymer laminate core in the thickness range of 50-120µm with a low surface profile copper cladding for ultra fine-pitch wiring. RXP1 utilizes a thermosetting, hydrocarbon-based resin systems, a smooth ED copper foil for improved loss performance, and flat glass reinforcement to minimize the effect of the glass weave on signal propagation. The laminate material of RXP1 has excellent thermal stability and a high glass transition temperature (Tg) of >3000°C making it ideal for lead-free solder and other high temperature interconnects. It also has X-Y CTE in the range of 10-15ppm/°C to reduce the stress on the first level interconnects from Si and other ICs [43]. RXP4 is a 20µm thin unreinforced build-up film available as a free standing film or a resin coated foil (RCF). The advantages of this film are low RF signal delays and low RF power losses during signal transmission through the material [45].

The dielectric properties of RXP1 and RXP4 were characterized from 1 GHz to 110 GHz [40]. The extracted dielectric constant of RXP1 was 3.41±0.06 with loss tangent (tanδ < 0.006) up to 110 GHz. The extracted dielectric constant of RXP4 was 2.98±0.05 with loss tangent (tanδ <0.005) up to 110 GHz. RXP inductors showed unloaded quality factors of about 100 - 150 in the frequency range of 1- 15 GHz and had line widths in the range of 2-4 mils showing high performance and integration capabilities [38]. Table 1 summarizes the properties of materials for system integration.

Table 1. Comparison of system integration platforms.

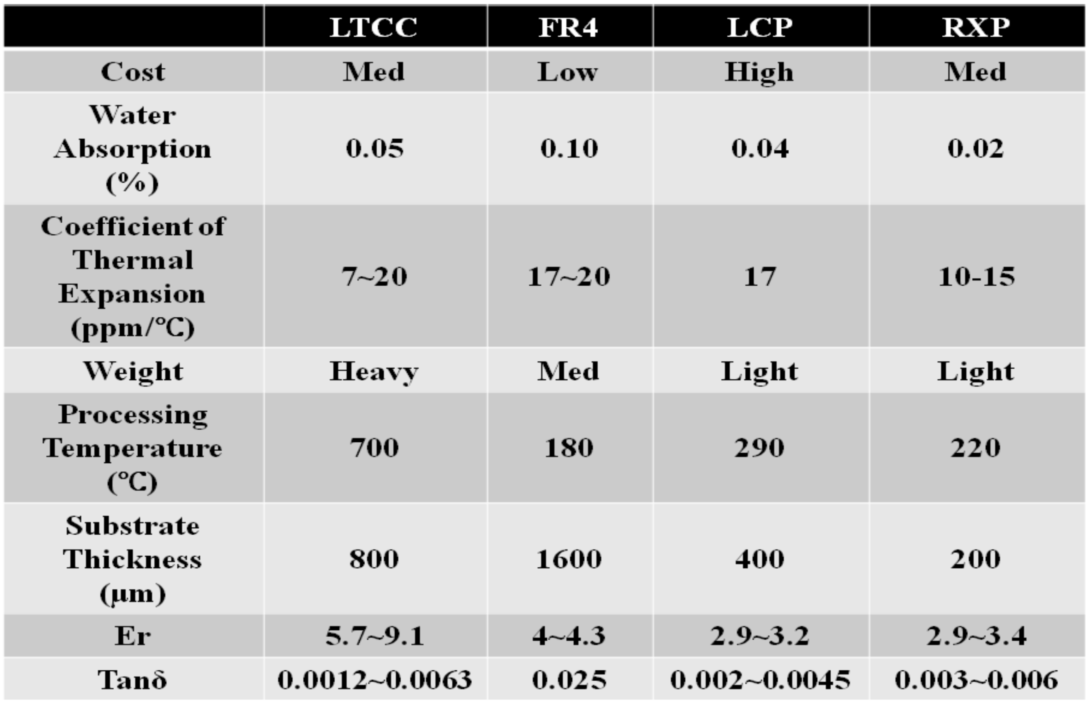

	LTCC	FR4	LCP	RXP
Cost	Med	Low	High	Med
Water Absorption (%)	0.05	0.10	0.04	0.02
Coefficient of Thermal Expansion (ppm/℃)	7~20	17~20	17	10-15
Weight	Heavy	Med	Light	Light
Processing Temperature (℃)	700	180	290	220
Substrate Thickness (μm)	800	1600	400	200
Er	5.7~9.1	4~4.3	2.9~3.2	2.9~3.4
Tanδ	0.0012~0.0063	0.025	0.002~0.0045	0.003~0.006

1.2 Material Characterization Methods

Since wireless applications operate at high frequencies, it is necessary to characterize materials as a function of frequency. Accurate dielectric constant and loss tangent of dielectric materials are essential for designing front-end module components. For example, design of high-Q passive devices is very sensitive to small changes in material properties that are important for obtaining accurate system response as well as achieving the highest quality factor for the passive components.

Microwave techniques for characterizing materials can be broadly classified into two techniques, namely non-resonant and resonant based methods. Non-resonant based methods use wave propagations on a transmission line to extract dielectric properties over a continuous frequency-range of interest [46] whereas resonant based methods are used to extract dielectric properties at discrete frequencies corresponding to the resonant frequency of the device [47]. In spite of the simplicity of non-resonant methods, resonator methods are widely used in material characterizations because of their sensitivity and high accuracy. The main advantage of the resonator based method is its sensitivity to small changes in low-loss dielectric properties [48].

In [48], a split-cylinder resonator was used to extract material properties. However, asymmetrical movement of the two terminations results in considerable measurement errors especially at high frequencies using this approach. A parallel-plate cavity resonator based on analytical solutions for estimating the resonant frequency was introduced in [49]. Although this resonator is simple to fabricate, the analytical equations are inaccurate for the characterization of low-loss materials. In [50], a microstrip ring resonator was introduced and the dielectric constant was extracted using regression analysis at resonant frequencies until the reflection loss was minimized. However, it is difficult to use the ring resonator for characterizing thin dielectric materials because the coupling coefficient through the gap can be small.

Most of the characterization techniques in [51] rely on analytical equations for extracting materials properties, which cause decreasing accuracy of the extraction results for lossy substrates. In [50], dielectric constants were extracted by finding a regression formula and optimizing the dielectric constant at discrete resonance frequencies until the return loss (S_{11}) value becomes as small as possible. By using this numerical method idea, another characterization method that uses corner-to-corner plane probing method has been developed [52]. A parallel-plate resonator has been chosen over micro-strip or ring-gap resonators because the coupling through gaps becomes very small for thin dielectrics. The corner-to-corner plane probing method requires only two-metal layered structures; hence it is simple to fabricate and measure. In addition, this structure is easier to probe because of positioning from the probes at the corner of the device.

The extraction method in [52] was based on the rapid solver which has some drawbacks. The rapid solver assumes a constant loss tangent. Since the loss tangent is a ratio of imaginary and real parts of the dielectric constant, the constant loss tangent is not a valid assumption because the imaginary and real parts of the dielectric constant are not constant but change with frequency. Furthermore, the rapid solver can only be applied in a low frequency range where the conduction loss is not affected by the surface roughness factor. Therefore, the material characterization by the rapid solver is limited to a low frequency because of the high frequency simulation inaccuracy.

As discussed in [53], the surface roughness introduces significant errors for dielectric material characterization. The surface roughness effect has been introduced in the conductor loss formulation [54], and the modeling of the conductor loss has been discussed in [55].

1.3 Filter Integration and Performance Problems

Wireless communication systems have been the most active part of modern electronics in the last few decades. As the market of wireless applications continues to grow, the development of wireless communication standards whose operating frequency bands are shown in Table 2 has also grown. A complete front-end module for a wireless communication system includes several blocks including power amplifiers, transceiver embedded circuits, antenna, baluns, and filters. Filters in the front-end module plays an important role for controlling the frequency bands of wireless standards as well as block the unwanted frequency bands. Every wireless product has one or more filters in their RF circuit architecture as shown in Figure 5 [56]. Hence, not only the filter-integration technology, but also the design technique and the performance of filters become critically important for wireless applications.

Table 2. Frequency bands of wireless standards.

Wireless Standards	Frequency Bands
GSM, CDMA, GPRS	824-894 MHz 880-960 MHz 1770-1880 MHz 1850-1990 MHz
UMTS(W-CDMA, CDMA2000)	1920-1980 MHz 2110-2170 MHz
GPS	1.2 GHz 1.5-1.6 GHz
WLAN	2.412-2.4835 GHz 4.9-5.9 GHz
Bluetooth	2.4 GHz
WiMAX	2.5-3.5 GHz
Military licensed band	4.4 GHz
Ultra-wideband (UWB)	3.1-10.6 GHz

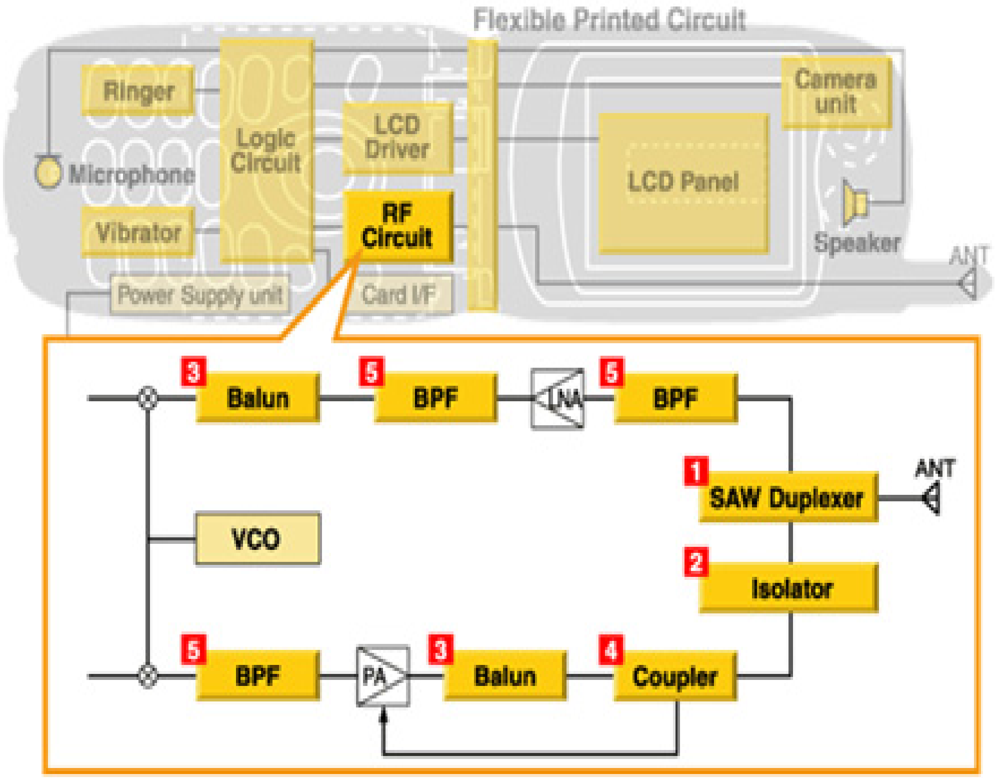

Figure 5. Block diagram of RF circuit in cellphone.

Among the wireless standards, wireless local area network (WLAN or Wi-Fi) has received special interest because of its unlicensed band and emerging mobile applications such as smart phones and mobile netbooks. The IEEE 802.11g (2.4 GHz) standard was established for higher band operation and better performance [57]. Following the WLAN specification, numerous SoP based bandpass filters (BPFs) have been reported [20-22, 58, 59]. Recently, IEEE has ratified the 802.11n (2.4 and/or 5 GHz) standard, which is almost ten times faster than 802.11g. IEEE 802.11n provides significantly enhanced data rate and range to help the data communication industry address the increasing demands placed on enterprise, home and public Wi-Fi [60]. Targeting the new standard, LTCC BPF designed for 5 GHz was presented in [18], which has 1.1 dB insertion loss with larger than 1 GHz bandwidth. In [61], a second-order LTCC BPF for C-band wireless application was presented with 1.4 dB insertion loss. Front-end LCP BPFs with center frequencies of 2.45 and 5.775 GHz were reported using a hybrid coplanar waveguide/stripline topology [28]. However, the LCP filter had a size of 12 mm^3, which was fairly large for wireless applications. Despite good RF performance using LTCC or LCP, the integration technology does not satisfy the demanding size and cost requirements.

While the filter integration technology affects miniaturization, design methodology used is responsible for the performance of filters. As the operating frequency of existing wireless standards comes closer and multiple standards are integrated into a package, high stopband rejection as well as low inband insertion loss in the transmitting and receiving paths is crucial for use in low-power wireless products supporting multiple wireless standards. For instance, more than 20 dB attenuation beyond 230 MHz out of the

WLAN passband frequency (2.4 GHz) is necessary to block the interference from W-CDMA (2.17 GHz). Therefore, the design requirements for BPFs become more difficult for suppressing unwanted frequency signals including harmonics, image, and inter-modulation signal or blocking the interference from other wireless standard bands.

A major challenge for filter design is to have sharp rejection responses at the stopband frequencies corresponding to the transmitter and receiver in a wireless module. The sharp rejection can be achieved by using a higher order filter topology. However, the overall size is also increased and the filter topology may not still satisfy the rejection requirements. To efficiently improve the stopband characteristics, transmission zeros can be introduced to produce notches at the stopband.

In [20], the authors designed the LTCC BPF with two transmission zeros based on an inductive coupled resonator with a feedback capacitor. Although the design methodology worked well with the measurement result, the size and rejection could not satisfy the stringent requirement such as more than 25 dB rejection from 400 MHz out of passband. Another work in [21] employed the step-impedance quarter-wavelength open stub to generate two transmission zeros at the low stopband and one transmission zero at the high stopband, but one of the low stopband transmission zeros was not observed in the implementation. The LCP Chebyshev three-pole filter using two transmission zeros was reported in [29]. However, the topology in [29] only produced a low stopband rejection making it difficult to block other high frequency bands. In [58], modified coupled inductors were used to produce transmission zeros, but it required more components and did not provide enough rejection.

1.4 Completed Research

The focus of the research in this dissertation is to realize high-performance passive circuits along with developing techniques for system-on-package integration using ultra-thin advanced polymers called RXP (Rogers experimental polymer), material characterization, and filter design for the high-loss substrate from 2.4/5 GHz WLAN to millimeter-wave frequency applications. To achieve this goal, the following work has been completed.

1. **Development of material characterization method**

   Material characterization method has been proposed to accurately extract the relative permittivity and loss tangent of the organic dielectric substrate. Parallel-plate resonators with corner-to-corner probing technique have been used for simple yet accurate fabrication and measurement. An automated extraction algorithm based on the finite difference method was applied for fast and efficient extraction process. In addition, more reliable correlation results at high frequency was achieved by including the surface roughness effect in the frequency-dependent conductivity model.

2. **Characterization of low-loss RXP, ceramic, and high-loss materials**

   The proposed characterization method has been applied to ultra-thin (< 200 μm) advanced polymers for core (RXP1) and build-up (RXP4) materials that can be used as chip-last embedded technology substrate. Frequency-dependent relative permittivity and loss tangent of this material has been extracted from 1 GHz to 110 GHz for the first time [40]. Causal models of extracted material properties were made using the vector fitting method. Stable relative permittivity values (3% variation for RXP1 and

2% variation for RXP4 over 110 GHz band) and low loss (<0.006 up to 110 GHz) were observed, showing RXP as a promising packaging technology for wireless applications. To quantify the application of the proposed extraction method, material properties of ceramic and high-loss materials have been extracted from 1 to 67 GHz as well.

3. **Development of high-rejection bandpass filter topology and design methods**

   High-rejection bandpass filter topologies for narrow and wide bands have been developed by modifying resonator tank circuits and adding a grounding inductor. Multiple transmission zeros distributed at lower and upper stopband relative to the center frequency have been created without increasing the size of the layout significantly because interconnects have been used as design parameters. Along with design equations for individual circuit elements, a graphical design methodology was also provided to predict the filter performance using Z-parameters.

4. **Design of novel 3D stitched capacitor**

   3D stitched capacitor has been developed to make more symmetrical layout design than the 3D conventional parallel-plate capacitor. Input and output of the 3D stitched capacitor can be accessible in the same layer so that the other layout elements can be easily connected without violating the layout symmetry. Unbalanced shunt parasitics from the 3D conventional capacitor becomes balanced shunt parasitics in the 3D stitched capacitor, which has been verified through measurements.

5. Design of embedded passive circuits for RF using RXP technology

Six different bandpass filters have been designed, fabricated, and measured in the four-metal layer RXP substrate. Total of 96 RXP bandpass filters were measured and 93 filters worked for the first time using RXP fabrication. For the commercially challenging rejection requirement, the world's smallest 2.4 GHz narrow-band bandpass filters have been designed and measured to verify the proposed narrow-band circuit topology and 3D stitched capacitor performance. This filter has been included in the preliminary embedded-chip technology. The world's smallest 5 GHz wide-band second-order bandpass filters were designed and fabricated using the proposed wide-band circuit topology. The second-order 5 GHz filter was extended to the third-order bandpass filter to achieve even more sharp rejection performance. For dual-band module application, lumped-element dual-band bandpass filters have been designed using a novel single bandpass filter topology for miniaturization. The miniaturized high-rejection WLAN duplexer has been implemented by redesigning 2.4 and 5 GHz bandpass filters using a six-metal layer RXP substrate. A novel matching circuit has been used for obtaining good insertion loss as well as high rejection and isolation performance.

6. Design of embedded passive circuits for millimeter-wave frequency

Lumped-element passive circuits have not been reported before because of the self-resonance frequency limitation for passive components operating at millimeter-wave frequency. Thus, a method to avoid the self-resonance frequency limitation has been proposed to design lumped-element passive circuits by using RXP technology. A 57

GHz bandpass filter and 29 & 62 GHz dual-band bandpass filter have been designed and measured. In addition, 57-64 GHz duplexer has been designed.

7. Development of filter design method for high-loss substrates

High-loss substrate ($\tan\delta > 0.01$) is often avoided for realizing passive circuits because the high-loss substrate such as silicon and FR4 provides low passive-performance. Nonetheless, the silicon interposer is attractive solution for low-cost system integration. Hence, filter design method targeting for silicon interposer with through-silicon via (TSV) technology has been studied. The substrate loss from high-loss substrate mainly affects a passband response in the filter design. To obtain good insertion loss performance in the passband, two design techniques have been proposed. The first one is to make the passband region into the inductive region by designing a capacitor to operate as an inductor at frequency where first and second self-resonance frequencies occur. The second technique is to use via or TSV as a lossless inductor. To validate the idea, bandpass filters have been realized in high-loss FR4 substrate ($\tan\delta > 0.025$) and measured results show less than 0.5 dB insertion loss for good passband response. A coupling characteristic of TSV compared to copper via is analyzed to extend the proposed technique for the silicon interposer where highpass filter for millimeter-wave frequency can be realized.

1.5 Dissertation Outline

The rest of this dissertation is organized as follows. Chapter 2 proposes a method of frequency-dependent material property extraction based on the parallel-plate resonator. The algorithm of the proposed numerical method and the inclusion of surface roughness effect are presented along with the material characterization results for RXP, ceramic, and high-loss materials up to millimetre-wave frequency. Chapter 3, 4, 5 discuss the design of passive circuits from RF to millimetre-wave frequencies. Chapter 3 focuses the design of high-rejection bandpass filters for WLAN application using RXP technology. Two circuit topologies are synthesized, and the proposed graphical design method is presented along with new 3D stitched capacitor design. Chapter 4 presents lumped-element dual-band bandpass filters and a duplexer realized in the RXP substrate. Chapter 5 explains the idea of avoiding the self-resonant frequency at millimetre-wave and shows lumped-element bandpass and dual-band filters realized in the 60 GHz band. Chapter 6 discusses an opportunity with silicon interposer and TSV for passive circuit integration and presents bandpass filter designs realized in FR4 to show the proof-of-concept. The dissertation is concluded in Chapter 7.

CHAPTER 2

MATERIAL CHARACTERIZATION

As the operation frequency continues to increase for next generation RF applications, fabrication techniques and dielectric materials in RF substrates have to meet very demanding performance requirements. In addition, many of the dielectric materials that are widely used for RF circuit design show limitations on the implementation for higher frequency applications. For instance, FR4 becomes dysfunctional because of prohibitively large losses in the high gigahertz range, and low temperature co-fired ceramic (LTCC) has a relatively high cost [1]. One potential material that could overcome these limitations is Liquid Crystal Polymer (LCP). Although LCP has low loss (loss tangent = 0.002-0.004 for $f < 105$GHz) and low cost (\$5/ft^2 for 2-mil single-clad low-melt LCP) [2], the high processing temperature (290 °C) and compatibility with build-up substrates cause other barriers.

Since the wireless products continue to evolve to have thinner products than their previous generation, a new dielectric material is crucial for accommodating the needs of extremely thin dielectric substrates. Accurate dielectric constant and loss tangent characterization are essential for numerous applications. To accurately estimate the material properties, frequency-dependent dielectric constant and loss tangent need to be extracted. Since next generation applications keep moving to high frequencies, it is necessary to characterize materials up to the millimeter wave range. Microwave techniques for characterizing materials can be broadly classified into two techniques, namely non-resonant and resonant based methods. Non-resonant based methods use wave propagation on a transmission line to extract dielectric properties over a continuous frequency range of interest [46] whereas resonant based methods are used to extract dielectric properties at discrete frequencies corresponding to the resonant frequency of the device [47]. The advantage of the resonator based method is its sensitivity to small changes in low-loss dielectric properties. The resonant based method has therefore been proposed and used for organic and non-organic material characterizations in this chapter.

This chapter focuses on material characterization method and material characterization results for low-loss organic and ceramic, and high-loss materials. The proposed extraction method including measurement method, automated extraction algorithm, inclusion of surface roughness, and estimation of dielectric thickness is explained in Section 2.1. Then, characterization results of RXP, ceramic, and high-loss materials from 1 GHz to 110 GHz are presented in Section 2.2. Finally, the chapter is summarized in Section 2.3

2.1 Material Characterization Technique

2.1.1 Cavity Resonator with Corner-to-Corner Probing Method

To extract material property, cavity resonator has been used. The top and side views of the resonator are shown in Figure 6.

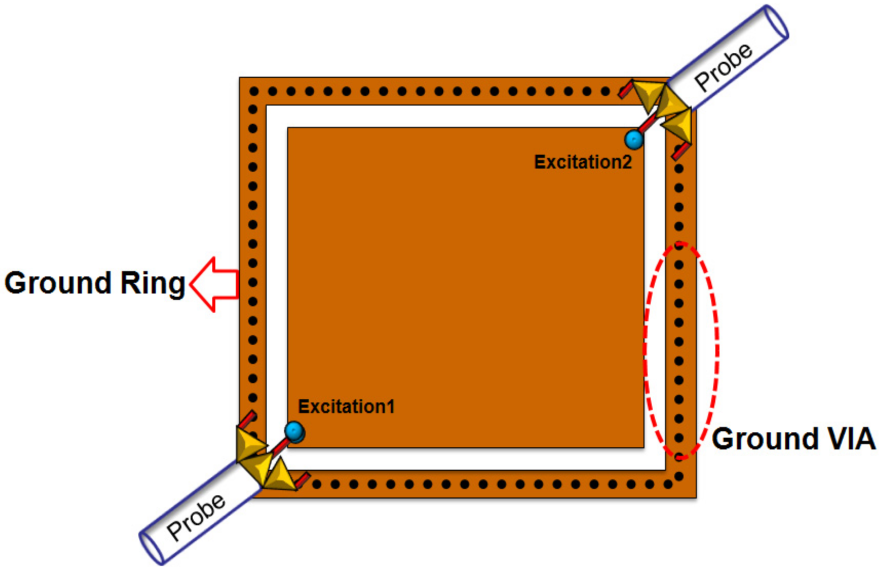

(a)

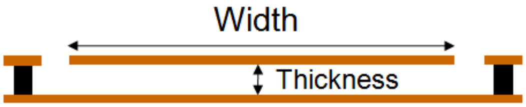

(b)

Figure 6. Cavity resonator. (a) Top view. (b) Side view.

The resonator has a parallel-plate structure having a dielectric in between top and bottom surface metal planes. The structure is surrounded by an additional top ground ring that is shorted to the bottom ground plane using vias. This additional ground ring is used as the ground reference for RF probes to excite the parallel-plate structure. Between the ground ring and top plate on the top surface, there is a gap determined by the probe pitch. The gap is optimized to ensure that there is negligible coupling between the parallel-plate structure and the additional ground ring.

A typical simulated or measured frequency response (Z_{12}, transfer impedance) of the cavity resonator is shown in Figure 7. As seen in Figure 7, the dielectric constant can be extracted from the resonant frequencies and the loss tangent can be extracted from the magnitude of Z_{12} at the resonant frequencies. Also, the dielectric thickness of the resonator can be estimated by extrapolating the measured frequency response at low frequencies where the resonator acts as a capacitor. It is important to note that the cavity resonator provides a limited number of resonances depending on the physical dimensions and material properties over the frequency band of interest. Therefore, several resonators of different sizes need to be designed for material characterization up to millimeter-wave frequencies.

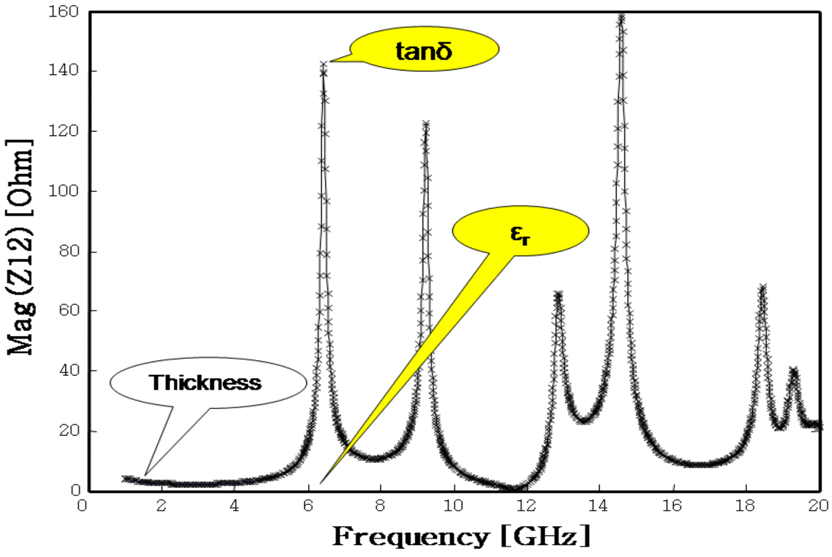

Figure 7. Frequency response of the resonator.

For design of the resonators, the rectangular waveguide resonant frequency formula is used, which is defined by

$$f_{mn} = \frac{c}{2\sqrt{\mu_r \varepsilon_r}} \sqrt{\left(\frac{m}{a}\right)^2 + \left(\frac{n}{b}\right)^2} \qquad (1)$$

where a and b are the width and length of the resonator, μ_r and ε_r correspond to the relative permeability and dielectric constant, c is the speed of light, and m, n are integers representing the resonant modes [62].

The parallel-plate cavity resonator requires only a 2-layered structure, hence it is simpler in terms of fabrication of the structure. Moreover, measurements can be done without introducing any via holes inside the plane pair using the corner-to-corner probing method. Therefore, de-embedding of measurement pad and line is not required. As shown in Figure 8, the signal tip of the probe touches the corner of the parallel-plate plane whereas the ground tips of the probe touch the surrounding ground ring which is shorted to the bottom plane with vias. As a result of this probing method, the measurement error from additional measurement pad or de-embedding steps can be minimized.

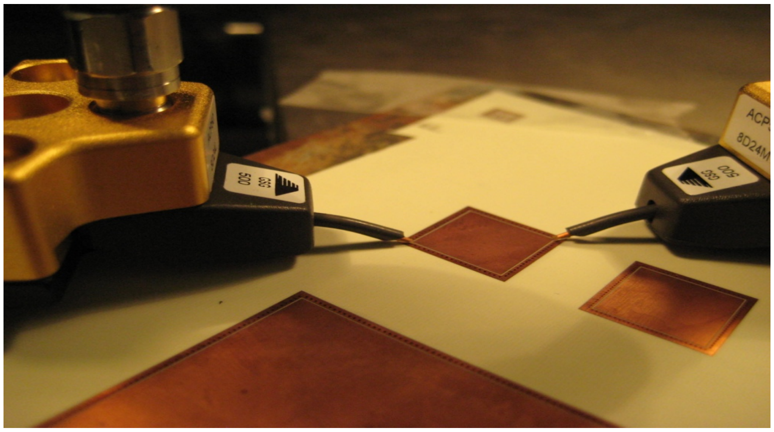

Figure 8. Corner-to-corner probing method.

2.1.2 *Automated Extraction Modeling and Algorithm*

Using the physical dimensions of the resonator and dielectric material parameters, the resonator needs to be simulated by using electromagnetic solvers until the simulated response is close to the measured response at the discrete resonant frequencies. This is done by iteratively changing the dielectric parameters of the material. The finite difference method (FDM) has been used and automated to compute the transfer-impedance (Z_{12}) parameters. The transfer-impedance parameters are less sensitive to probe parasitic because the self-impedance is affected by probe inductance.

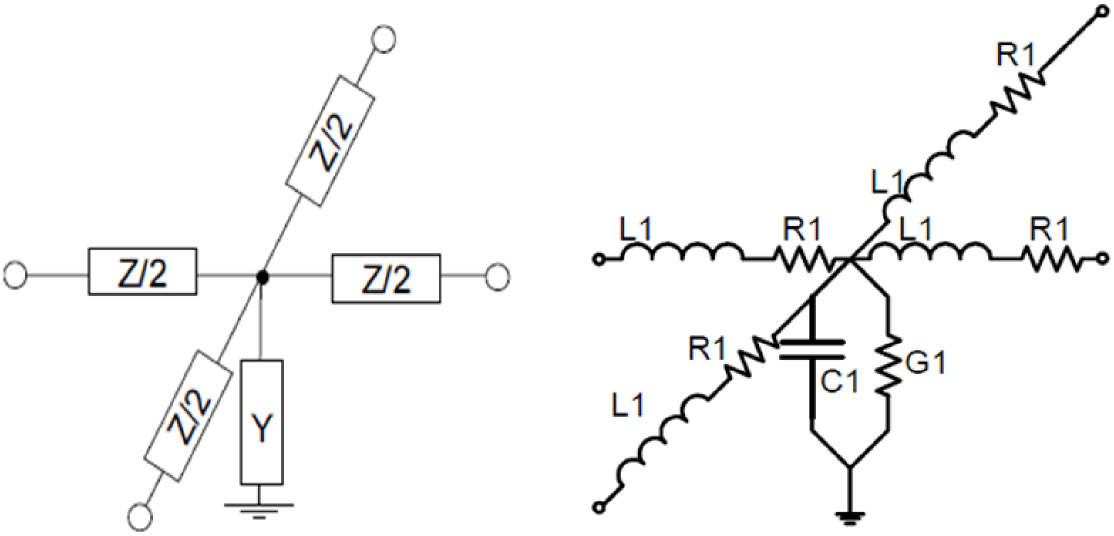

(a) (b)

Figure 9. (a) Unit cell model of a single plane pair. (b) Electrical model of FDM [63].

Unit cell and electrical model of FDM is shown in Figure 9. The FDM formulation has been discussed in detail in [64]. The formulation has been extended to include the surface roughness effect. The FDM method replaces the cavity resonator shown in

Figure 6 by square mesh where the impedance (Z) and admittance (Y) of each unit cell in the mesh can be calculated as [63]

$$Y = j2\pi f \cdot C_{uc} + 2\pi f \cdot C_{uc} \tan\delta \tag{2}$$

$$Z = j2\pi f \cdot L_{uc} + 2\sqrt{\frac{j2\pi f \cdot \mu}{\sigma}} + \frac{2}{\sigma t} \tag{3}$$

where $tan\delta$ is the loss tangent, σ is the conductivity, t is the thickness of the conductor, and C_{uc} and L_{uc} are capacitance and inductance of the unit cell that can be expressed as

$$C_{uc} = \varepsilon \frac{w^2}{d} \qquad\qquad L_{uc} = \mu d \qquad (4).$$

In the above equations, ε is the permittivity, w is the width of the unit cell, and d is the thickness of the dielectric. The second term in (2) represents the dielectric loss. In (3), the second term represents the AC resistance due to skin effect and internal inductance while the third term represents the DC resistance.

As the frequency increases, constant conductivity in (3) is no longer valid because the surface roughness significantly decreases the conductivity at high frequencies where the skin depth becomes smaller than the surface roughness. Based on [65], the frequency-dependent conductivity can be expressed as

$$\sigma(f) = \frac{\sigma_o}{(1 + \exp(-\frac{\delta(f)}{2T})^{1.6})^2} \tag{5}$$

where f is the frequency, σ_o is the conductivity at low frequency, and T is the root mean square of the surface roughness. Substituting (5) into (3), the impedance of each unit cell can be rewritten as

$$Z = j2\pi f \cdot L_{uc} + 2 \cdot (1 + \exp(-\frac{\delta(f)}{2T})^{1.6}) \cdot \sqrt{\frac{j2\pi f \cdot \mu}{\sigma_o}} + \frac{2}{\sigma_o t} \quad (6).$$

In the simulation technique used for material characterization in [66], the extraction process is performed by using a wide frequency range around the resonant frequency. Since the simulation time is directly proportional to the number of frequency points, the computational cost can be very high. Therefore, a narrow-band simulation technique has been used to reduce the computational time.

The correlation process begins with the extraction of resonant frequencies from the measured Z_{12} response obtained from the S-parameters. The resonant frequencies can be estimated using the imaginary parts of poles extracted from measured Z_{12} data where the poles can be obtained from vector fitting [67]. For extracting the material parameters accurately, the algorithm uses three measured frequency points, namely the frequency at resonance and two adjacent frequency points. Then, an iterative simulation is performed until good correlation is obtained at all the three frequency points. To iteratively compute the material properties, Nelder-Mead simplex method [68] was used until the least square error between the simulated and measured results is minimum. A flow chart of the iterative extraction process is shown in Figure 10, and a typical narrow-band simulation result after convergence is shown in Figure 11 where the simulated results lie exactly on top of the measured results.

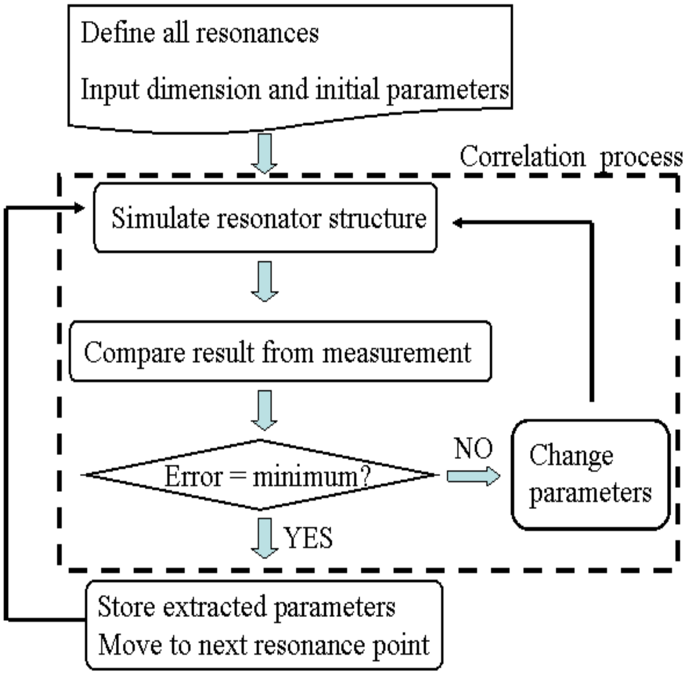

Figure 10. Flow chart of extraction process.

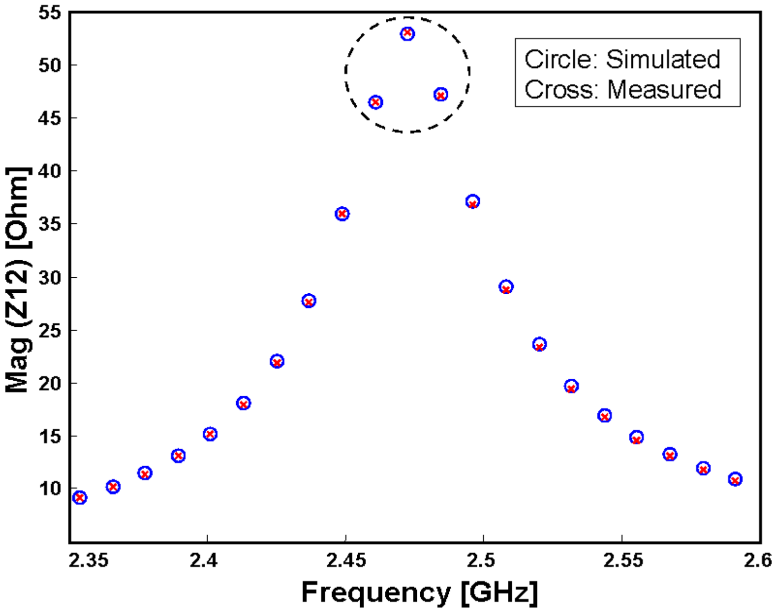

Figure 11. Correlation result from narrow-band simulation.

The number of unit cells in FDM is very important because the unit cell size is directly proportional to the simulation times since the final solution involves a matrix inversion. In the ideal case, it will be best to use as small as possible unit cell size in order to have the most accurate simulation result. However, the number of unit cell size has to be optimized in order to have accurate and efficient simulation results.

Theoretically, it is recommended that the size of unit cell should be less than a tenth of the wavelength in the dielectric material. By using a tenth of the wavelength for the size of unit cell, the simulation results can in general be matched with measurements. However, the theoretical size of the unit cell cannot be used in the extraction process since the simulation results are not accurate enough to extract the material parameters of interest. Figure 12 demonstrates how the simulation results change as the size of unit cell decreases.

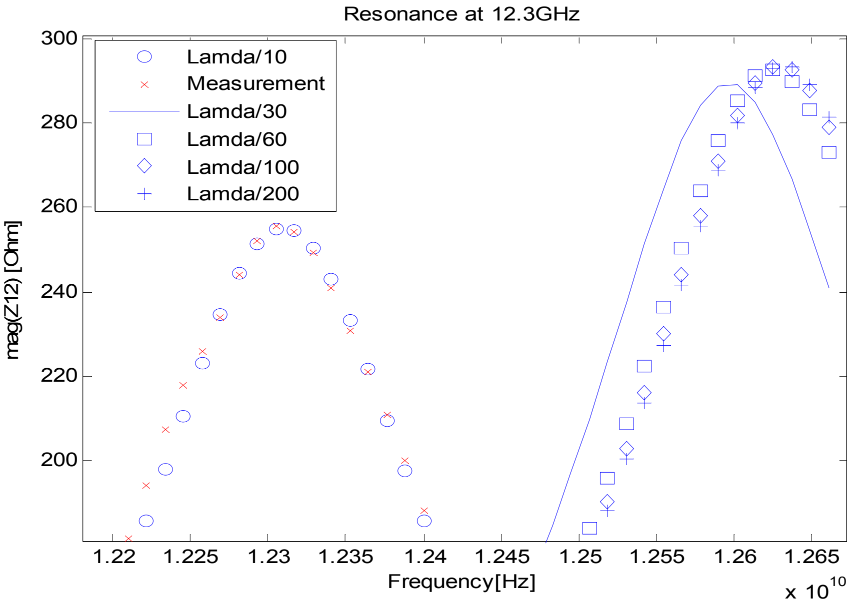

Figure 12. Simulation result for the sensitivity of unit cell size.

The extracted parameters obtained from the use of the theoretical unit cell size are applied to the same resonance frequency by decreasing the size of the unit cell. Consequently, the simulation graph continues to shift to the right as the size of the unit cell is decreased. By comparing squares and diamonds in Figure 12, it can be seen that the simulation graph is not shifted much after the unit cell becomes smaller than a sixtieth of the wavelength. Eventually, the simulation result converges when the unit cell is smaller than two-hundredth of the wavelength.

To find the ideal unit cell size in terms of the simulation speed and the convergence of the result, the extracted dielectric constant for one thirtieth, one sixtieth, and one two- hundredth are compared. The difference between one sixtieth and one two-hundredth was about 0.01%, and the difference between one thirtieth and one sixtieth was about 0.08%. Moreover, the variations from extracted loss tangents were negligible. Therefore, it can be concluded that a thirtieth of the wavelength is the ideal unit cell size because the simulation speed for a thirtieth of the wavelength is 8 times faster than one sixtieth of the wavelength, and the difference between them is negligible.

2.1.3 Inclusion of Surface Roughness Effect

The surface roughness of the conductor was measured using a Veeco Instruments Sloan DEKTAK® 3030 surface profiler. The probe of the system travels on the surface of the conductor. Figure 13 shows the surface roughness measurement results for RXP1 and RXP4 dielectric materials. The horizontal axis is in microns, and the vertical axis is in angstroms. The measured surface roughness of RXP1 was 0.78μm, and the measured surface roughness of RXP4 was 1.03μm, which represent root mean square (RMS) values of the measurement across the surface of the cavity resonator.

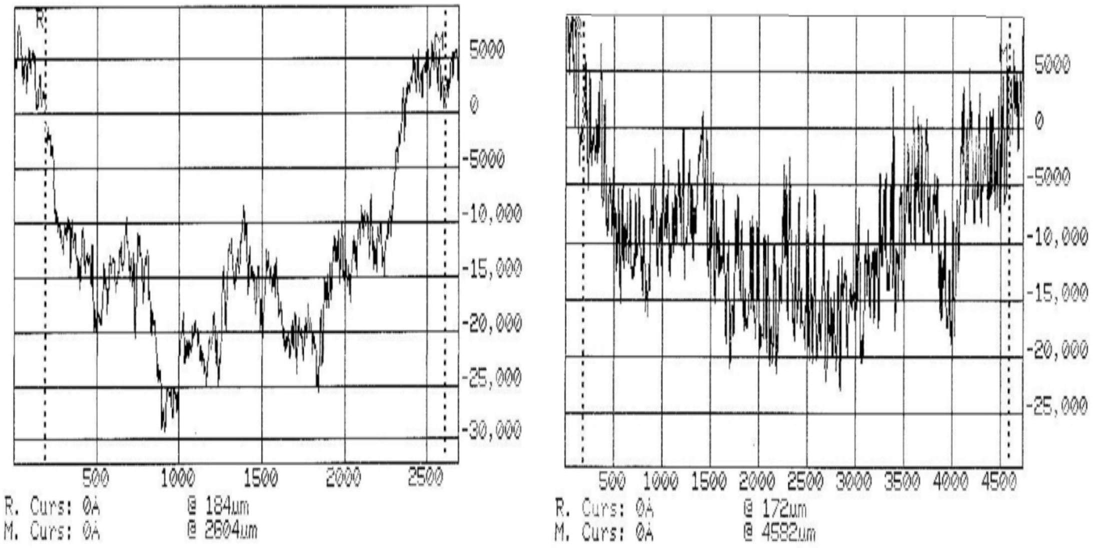

(a) (b)

Figure 13. Surface roughness measurement. (a) RXP1. (b) RXP4.

To illustrate the effect of surface roughness on the conductivity, the frequency-dependent conductivity of copper from 1 GHz to 40 GHz for RXP1 and RXP4 is shown in Figure 14. As shown in the figure, the skin depth becomes smaller than the surface roughness at 7.2 GHz for RXP1 and 4.1 GHz for RXP4 (shown as star in the figure) where the frequency-dependent conductivity becomes less than half of the original conductivity (5.8 x10^7 S/m). Above 40 GHz, the effective conductivity approaches 1.45 x 10^7 S/m.

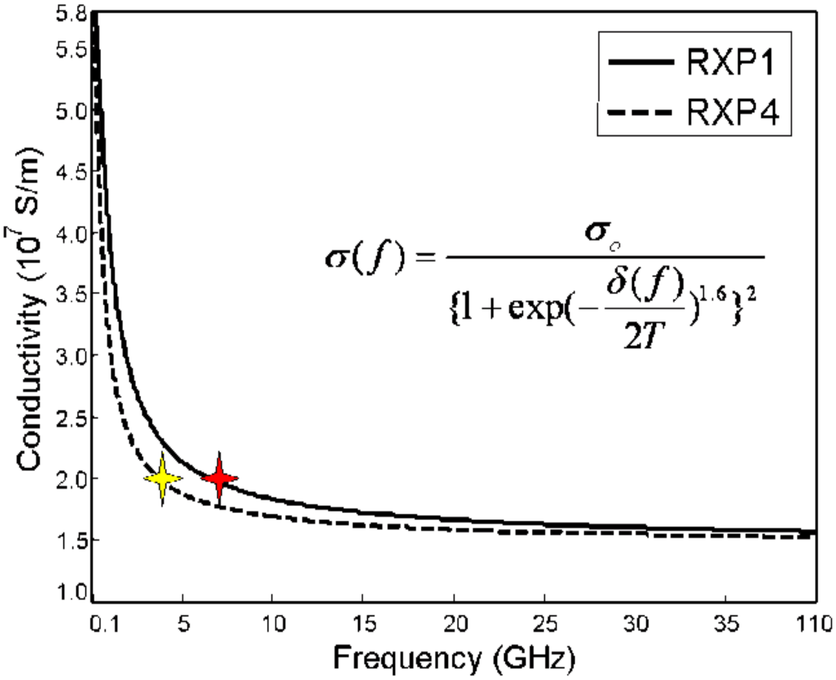

Figure 14. Frequency-dependent conductivity for RXP1 and RXP4.

To illustrate the effect of surface roughness on the dielectric constant and loss tangent extraction, the characterization results without and with the surface roughness effect on RXP1 are shown in Figure 15. As seen in Figure 15 (a), there are small differences for the dielectric constant in both cases. However, the effect of surface roughness on the extracted loss tangent can be large, as shown in Figure 15 (b). Therefore, the surface roughness from the conductor mainly affects the loss tangent during the extraction process.

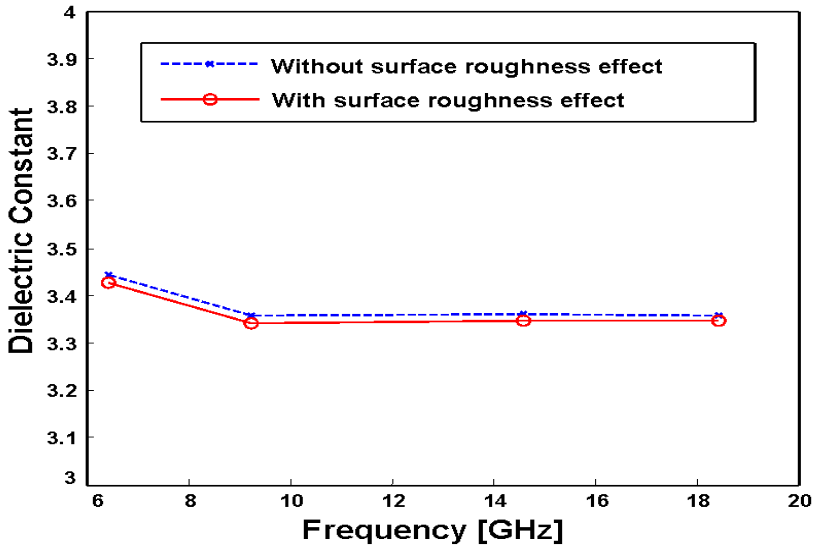

(a)

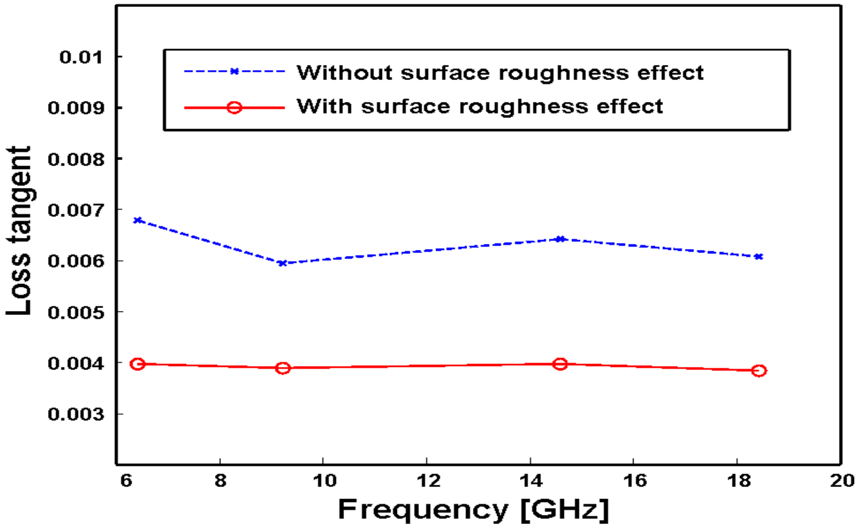

(a)

Figure 15. Surface roughness effect on RXP1. (a) Dielectric constant. (b) Loss tangent.

2.1.4 Extraction of Dielectric Thickness

Using the proposed method, the dielectric thickness can be extracted using at low frequencies where the resonator is not sensitive to the material properties. The extracted thickness of RXP1 and RXP4 were 115.5µm and 19.2µm as shown in Figure 16 (a) and (b), respectively. Unlike material parameters extraction, the thickness can be measured by cross-sectioning where the resonator can be cut in half to examine the thickness, as shown in Figure 16 (c) and (d). The extracted thickness is within the range of the measured result from the cross-sectioning. This also demonstrates the efficiency of the proposed method for estimating the dielectric thickness, which is a critical parameter since it affects the loss tangent extraction.

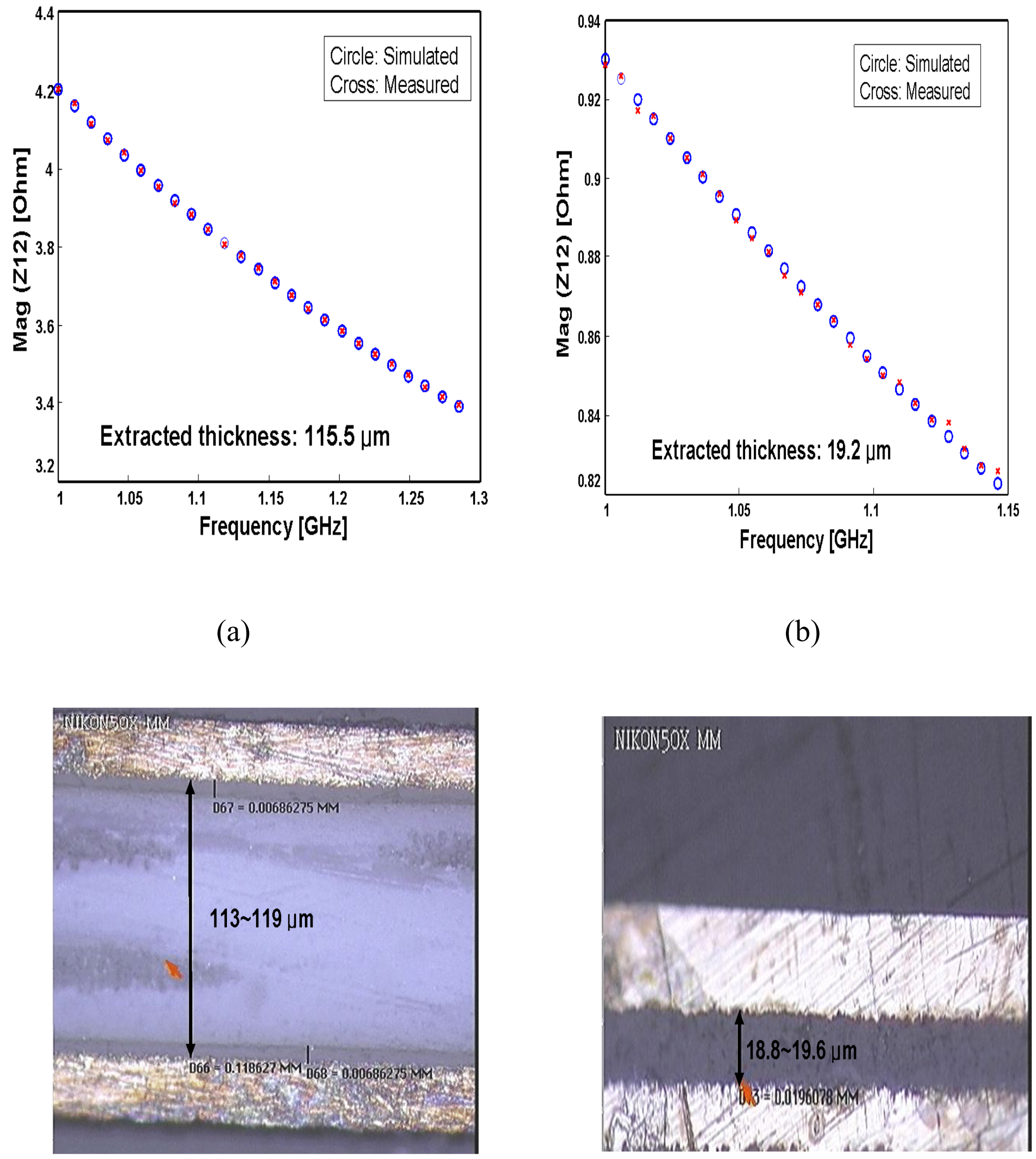

(a) (b)

(c) (d)

Figure 16. Thickness estimation and measured thickness. (a) Correlation for RXP1. (b) Correlation for RXP4. (c) Measured cross-section for RXP1. (d) Measured cross-section for RXP4.

2.2 Material Characterization Results up to Millimeter-Wave

2.2.1 Extraction of RXP Material Properties up to 110 GHz

Five cavity resonators were designed for characterizing the RXP1 and RXP4 materials using (1). The physical dimensions of the resonators are summarized in Table 3. A gap of 100 μm was used for all resonators, which results in negligible fringing capacitance for both the RXP1 and RXP4 dielectrics. The measured responses of resonators on RXP from 1 to 110 GHz are shown in Figure 17. As shown in Figure 17 (c) and (d), the measured response from 40 to 110 GHz exhibits peaks at resonant frequencies that are not as sharp as from 1–40 GHz. Although these non-sharp peaks do not affect the extraction of dielectric constant, it can introduce errors in the loss tangent extraction. To improve the accuracy of loss tangent extractions from 40 to 110 GHz, a full wave simulator [69] was used. It is important to note that the extraction process in Figure 10 has not changed.

Table 3. Physical dimensions of resonators.

	Width x Length (mm^2)	Thickness (d) (μm)	Frequency range
RXP1, RXP4	32.5 x 32.5	100, 20	1–20GHz
	12.5 x 12.5	100, 20	1–20GHz
	9.5 x 9.5	100, 20	20–40GHz
	6.5 x 6.5	100, 20	40–67GHz
	4.5 x 4.5	100, 20	67–110GHz

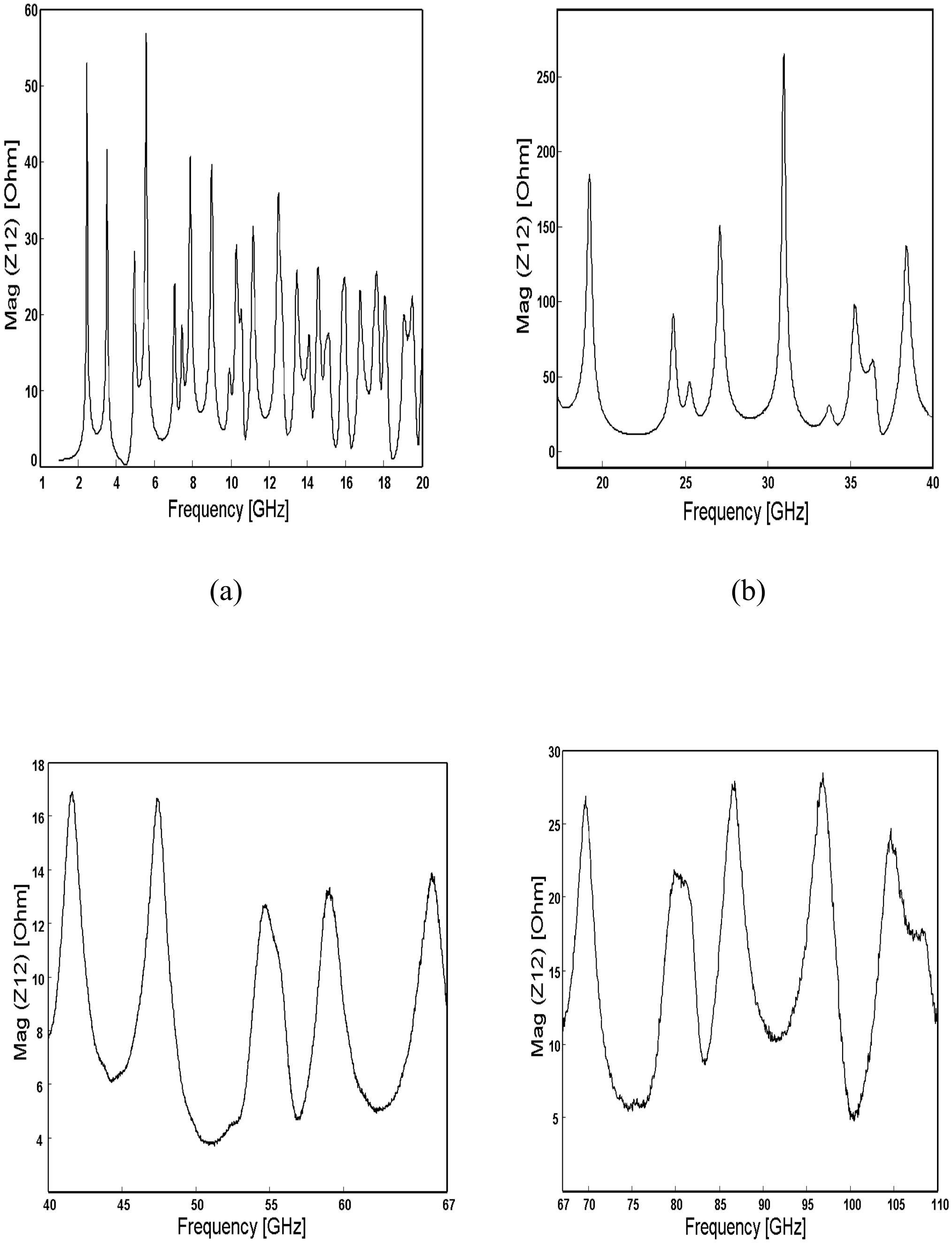

(a) (b)

(c) (d)

Figure 17. Measured transfer impedance (Z_{12}). (a) 32.5mm resonator with RXP1. (b) 9.5mm resonator with RXP1. (c) 6.5mm resonator with RXP4. (d) 4.5mm resonator with RXP4.

For the extraction of dielectric constant and loss tangent up to 110 GHz, the frequency range was divided into three parts namely 1-40 GHz, 40-67 GHz, and 67-110 GHz. The measurements were carried out using short-open-load-thru (SOLT) calibration. Up to 40 GHz, six resonators (32.5, 12.5, 9.5mm for the RXP1 and RXP4) were measured using Agilent PNA 8363B with Cascade GSG-500 air coplanar probes. From 40 GHz to 67 GHz, 6.5mm resonator was measured using Agilent PNA E8361C with GSG-250 air coplanar probes, and Agilent VNA 8510C was used for measurement on a 4.5mm resonator from 67 GHz to 110 GHz with GSG-250 air coplanar probes. The measured S-parameters were converted into impedance parameters for extracting the dielectric properties.

Figure 18 shows range of high frequency results where the measured and simulated results are superimposed demonstrating good correlation. The extracted RXP1 results are shown in Figure 19, and the extracted RXP4 results are shown in Figure 20 from 1 GHz to 110 GHz. The blue bar in the extracted results show how much extracted values are varying in the interval of 1-32 GHz, 32-62, and 62-110 GHz ranges.

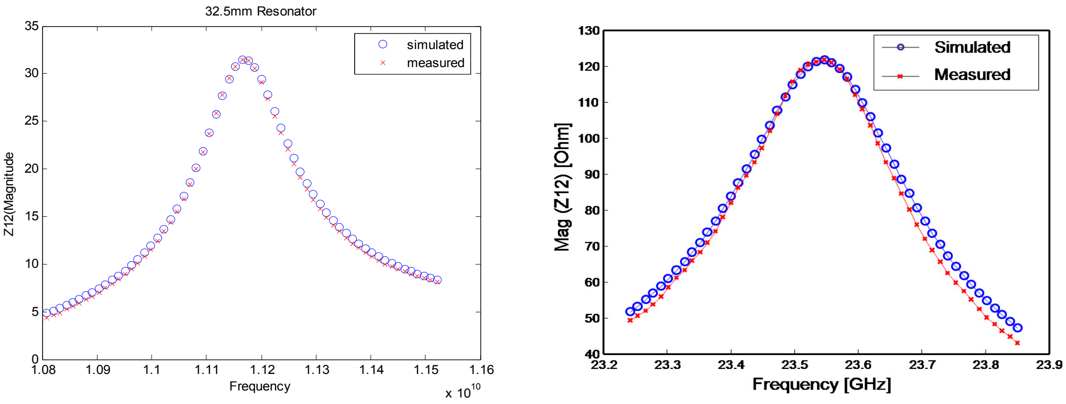

(a) 11 GHz (b) 23 GHz

Figure 18. Correlation result from microwave to millimeter-wave frequency.

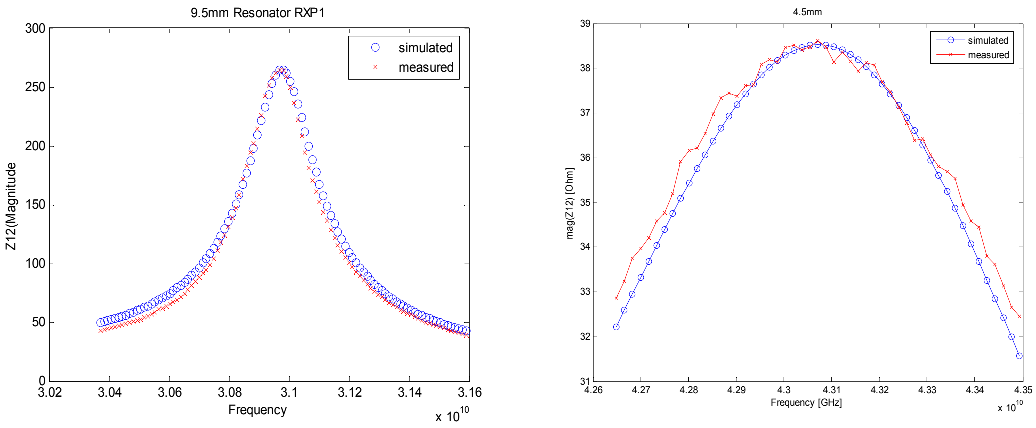

(c) 30 GHz (d) 43 GHz

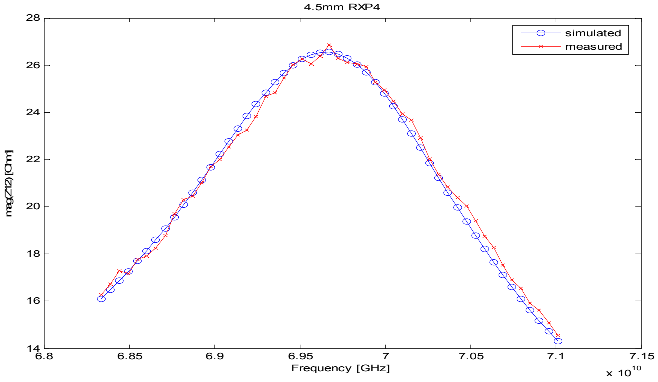

(e) 69 GHz

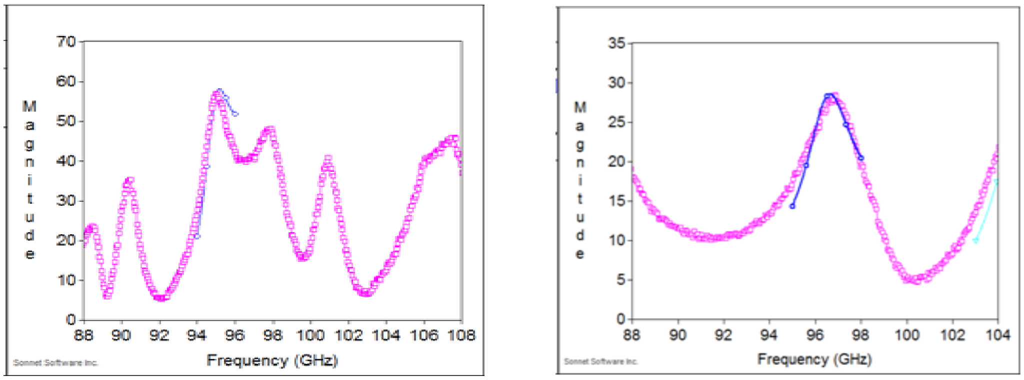

(f) 95 GHz (g) 97 GHz

Figure 18 Continued

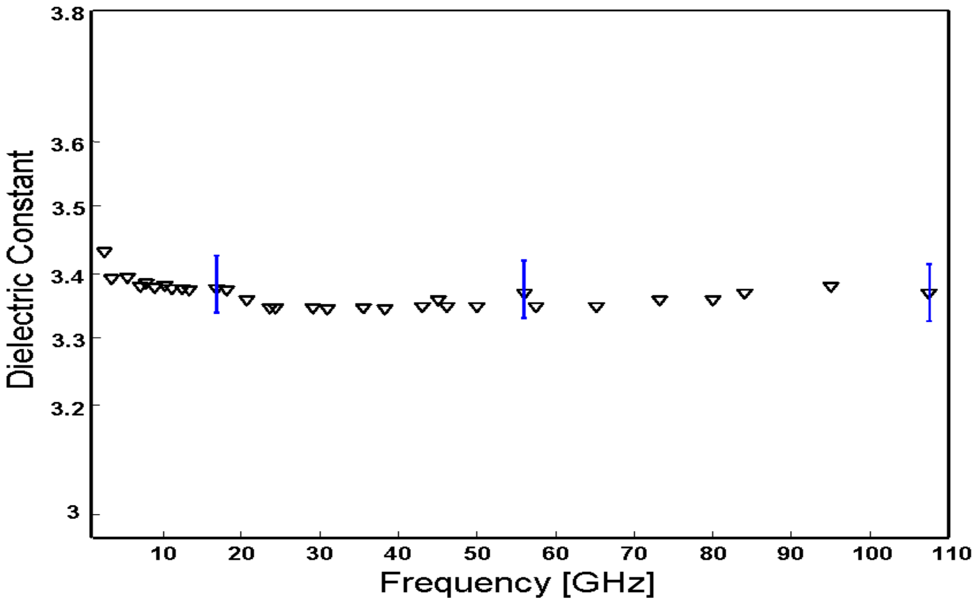

(a)

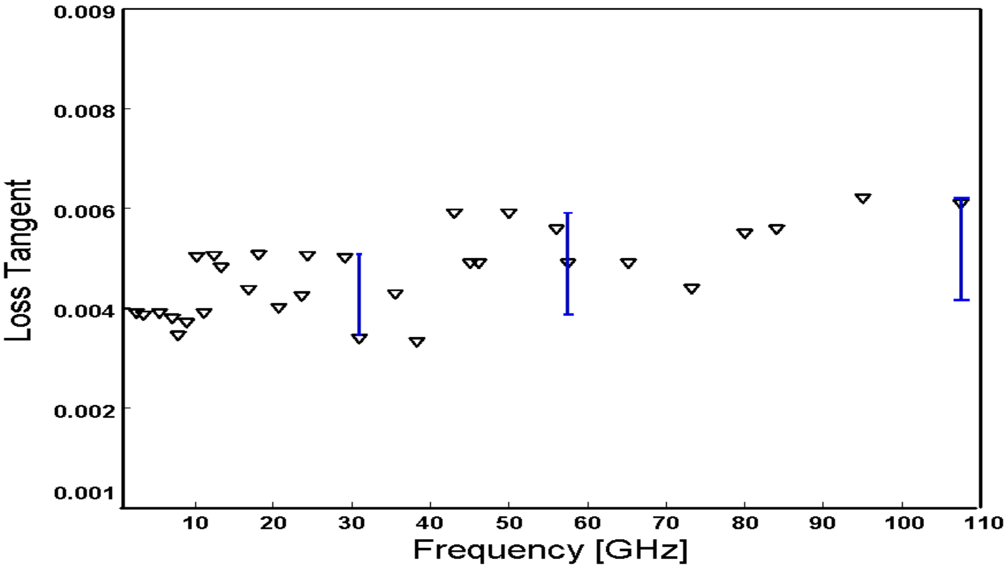

(b)

Figure 19. RXP1 extracted results. (a) Dielectric constant. (b) Loss tangent.

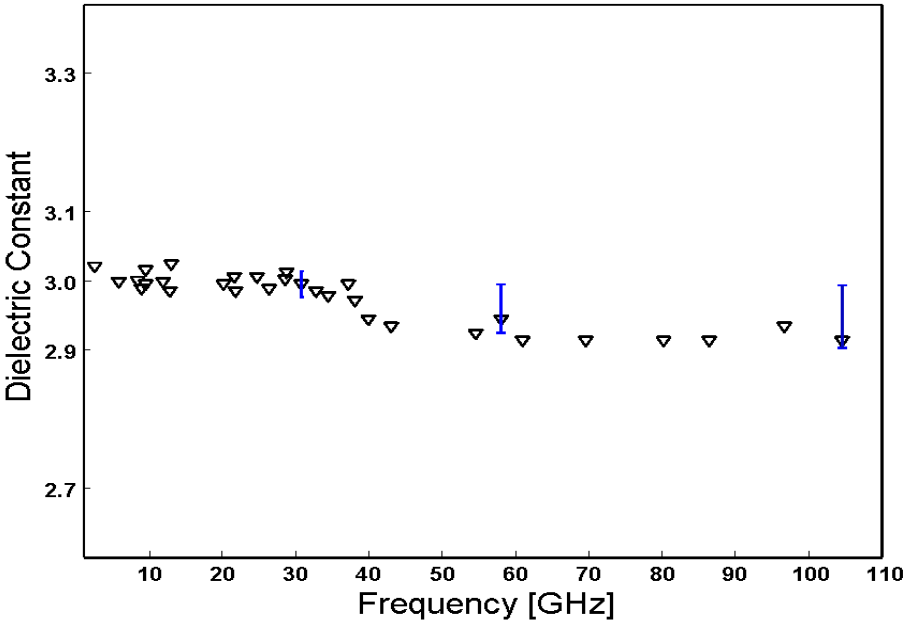

(a)

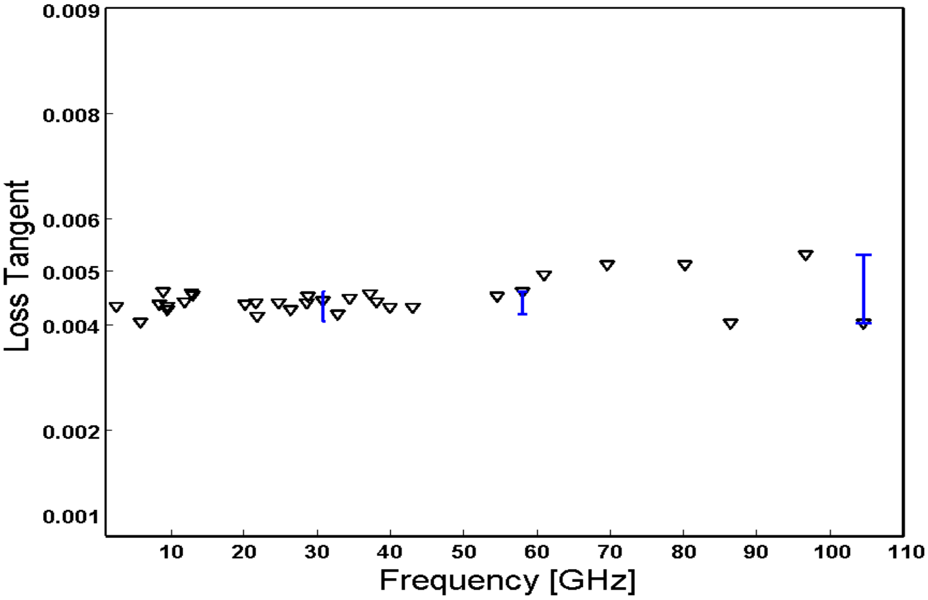

(b)

Figure 20. RXP4 extracted results. (a) Dielectric constant. (b) Loss tangent.

To illustrate how much frequency-dependent dielectric constant varies from low-frequency values, Table 4 summarizes the differences of the frequency-dependent extracted parameters from the low frequency vendor’s value up to 40 GHz. The extracted dielectric constant at 40GHz was 3.36, which is about 3% difference from the low frequency vendor’s value. The extracted loss tangent was 0.0040, which corresponds to a 5% difference.

Table 4. Difference between extracted values and vendor.

Frequency [GHz]	Difference from vendor ε_r (3.48 at 1GHz)	Difference from vendor Tanδ (0.0038 at 1GHz)
2.47	0.06	0.00011
3.52	0.09	0.00019
5.57	0.10	0.00010
7.89	0.11	0.00060
9.01	0.11	0.00043
11.17	0.11	0.00032
12.50	0.12	0.00029
13.46	0.12	0.00027
16.77	0.12	0.00024
18.07	0.12	0.00024
20.66	0.12	0.00023
23.55	0.12	0.00022
29.20	0.12	0.00021
35.47	0.12	0.00021
38.36	0.12	0.00021

2.2.2 Development of Causal Model

The extracted dielectric constant and loss tangent may violate causality because of measurement inaccuracies. Bode's integral relationship, which satisfies causality [70], requires a relationship between the real and imaginary parts of any complex function. A typical model that satisfies Bode's integral relationship is the Debye model, which can be used in electromagnetic solvers to obtain causal results. The Debye model has been constructed by using vector fitting method [67].

Based on the extracted frequency-dependent dielectric constant and loss tangent at discrete frequencies, vector fitting method can be used to create a state space representation. This results in a Debye model of the form

$$\varepsilon_r(s = 2\pi f) = \varepsilon_\infty + \sum_m \frac{b_m}{s - a_m} \tag{7}$$

where f is the frequency, ε_∞ is the real part of complex permittivity at very high frequency, a_m is the pole with negative real parts, and b_m is the residue with positive real parts. Using the constructed causal models, the dielectric constant and loss tangent of RXP1 and RXP4 were computed at all the frequencies, as shown in Figure 21.

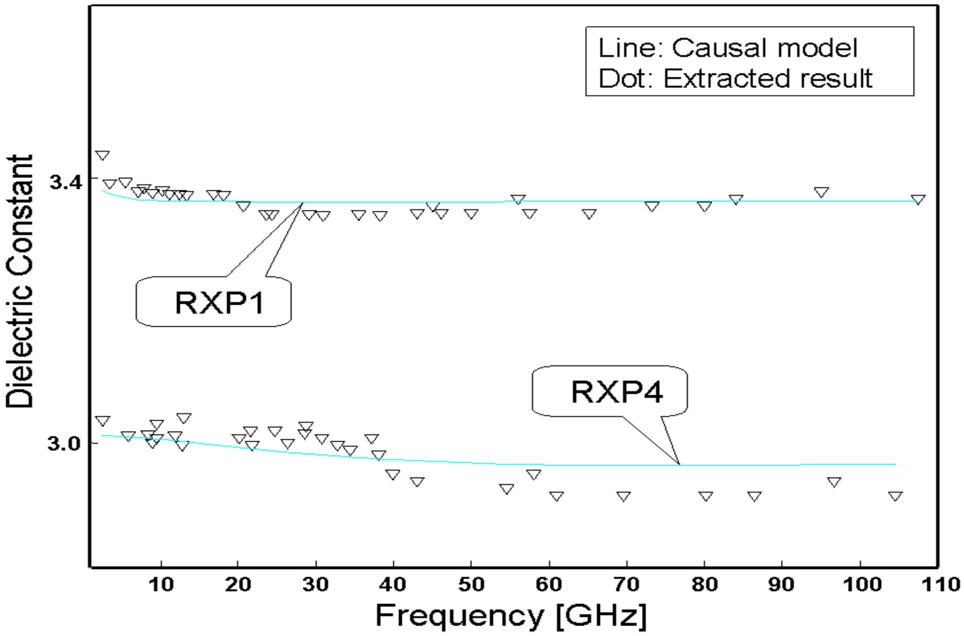

(a)

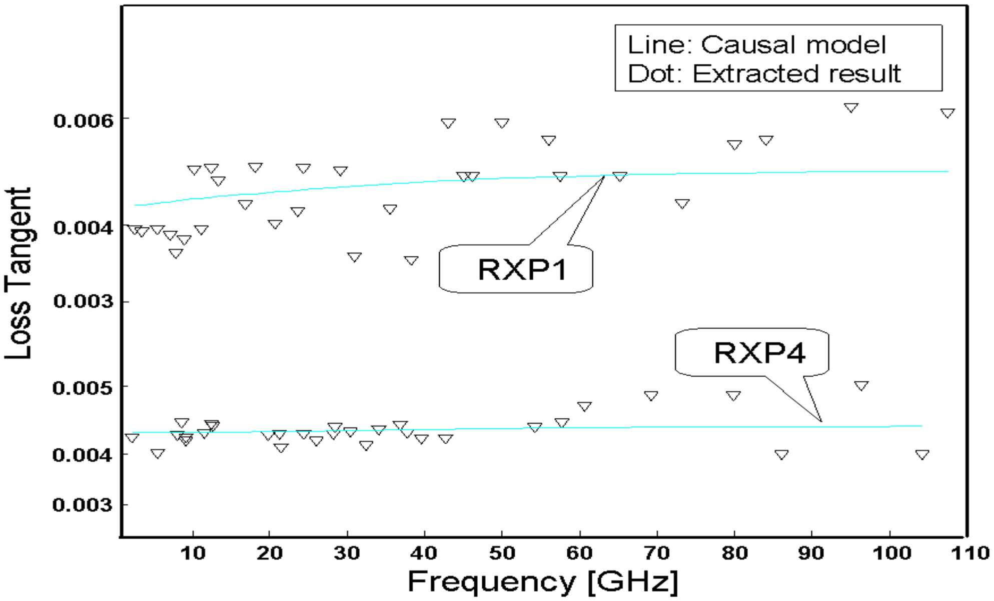

(b)

Figure 21. Causal model with extracted results. (a) Dielectric constant. (b) Loss tangent.

The dielectric constant in the causal model shows a variation less than 3% over the 110 GHz band for RXP1, and the RXP4 result has a variation of less than 2% over the 110 GHz band. The loss tangent has values between 0.0037-0.006 for RXP1, and 0.004-0.0053 for RXP4 in the frequency range from 1-110 GHz.

2.2.3 Extraction of Ceramic Material Property up to 67 GHz

In order to extract the dielectric properties (relative permittivity and loss tangent) of a ceramic substrate from 1 to 67 GHz, six parallel plate resonators have been designed and are presented in Figure 22. Their dimensions are respectively:

- Resonator 1: 30 mm x 30 mm;
- Resonator 2: 20 mm x 20 mm;
- Resonator 3: 10 mm x 10 mm;
- Resonator 4: 6 mm x 6 mm;
- Resonator 5: 5 mm x 5 mm;
- Resonator 6: 4 mm x 4 mm.

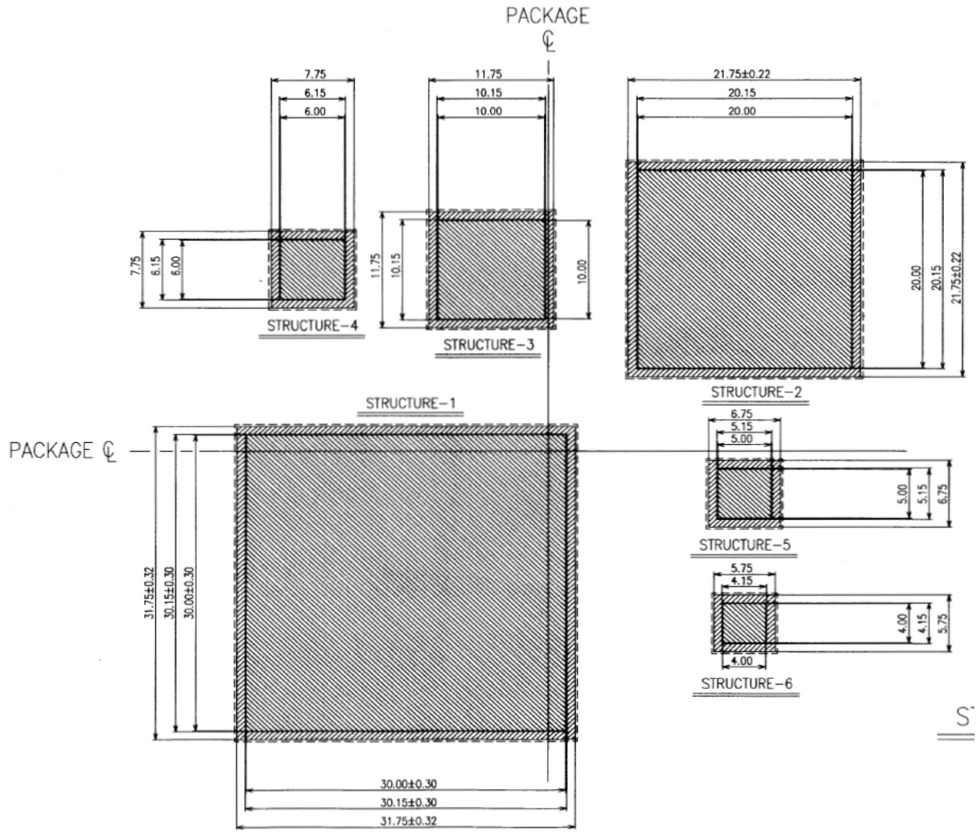

Figure 22. Layout of the parallel-plate resonators for ceramic material.

Four similar samples were provided as shown in Figure 23 to verify repeatability of the proposed extraction method. The metal thickness, metal roughness, as well as the substrate roughness have been measured with a Veeco Dektak 150 profilometer, with a very high resolution of 4 angstroms. Figure 3 shows a typical roughness measurement result. The ceramic substrate appears to be rough, with an average roughness of 1 micron. *Ra* indicates the average roughness, whereas *Rq* is the RMS roughness which is used to extract the dielectric parameters of the substrate. A metal thickness of 10 microns and a surface roughness of 1.01 microns have been considered for extraction process while the ceramic thickness of 137-145 microns is used.

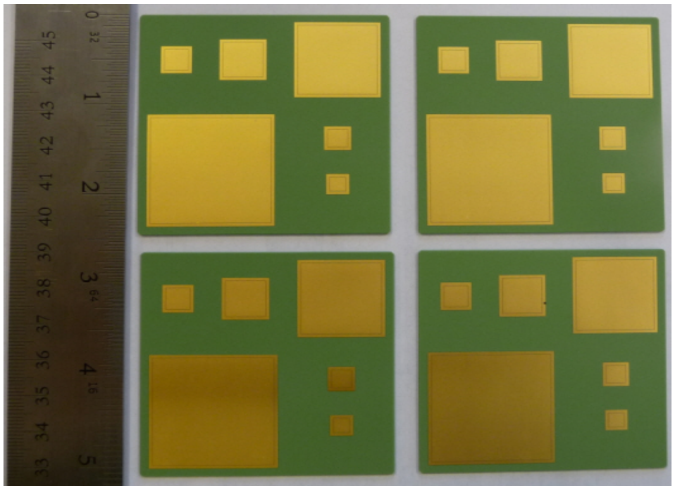

Figure 23. Fabricated resonators on ceramic substrate.

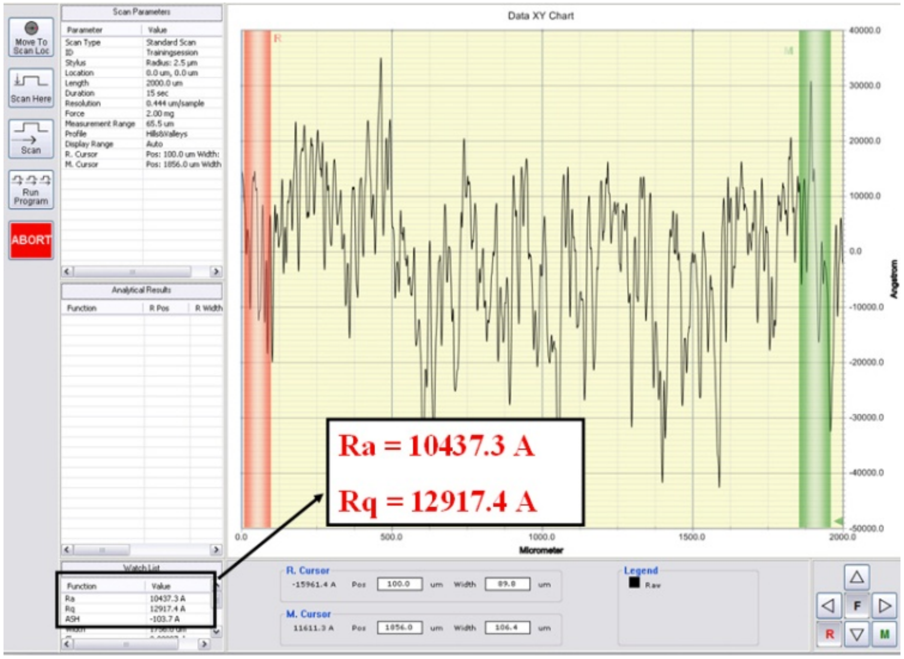

Ra = 10437.3 A

Rq = 12917.4 A

Scan Parameters

Parameter	Value
Scan Type	Standard Scan
ID	Trainingsession
Stylus	Radius: 2.5 µm
Location	0.0 um, 0.0 um
Length	2000.0 um
Duration	15 sec
Resolution	0.444 um/sample
Force	2.00 mg
Measurement Range	65.5 um
Profile	Hills&Valleys
Display Range	Auto
R. Cursor	Pos: 100.0 um Width:
M. Cursor	Pos: 1856.0 um Width

Analytical Results

Function	R Pos	R Width

Watch List

Function	Value
Ra	10437.3 A
Rq	12917.4 A
ASH	-103.7 A

R. Cursor
-15961.4 A Pos 100.0 um Width 89.8 um

M. Cursor
11611.3 A Pos 1856.0 um Width 106.4 um

Figure 24. Ceramic surface roughness measurement.

The parallel plate resonators resonances have been measured using an Agilent PNA E8361C. In order to get a better calibration and consequently a better accuracy in the measurements, the frequency range up to 67 GHz has been divided in 3 parts: [1-23]

GHz, [23-45] GHz, and [45-67] GHz. An SOLT calibration has been performed for each frequency range and 250-um pitch probes (67A-GSG-250) and a CS-5 calibration substrate have been used. As shown in Figure 25, the return loss measured at both ports for the four different samples shows almost no variation, which demonstrates the consistency of the measured results and the quality of the fabrication.

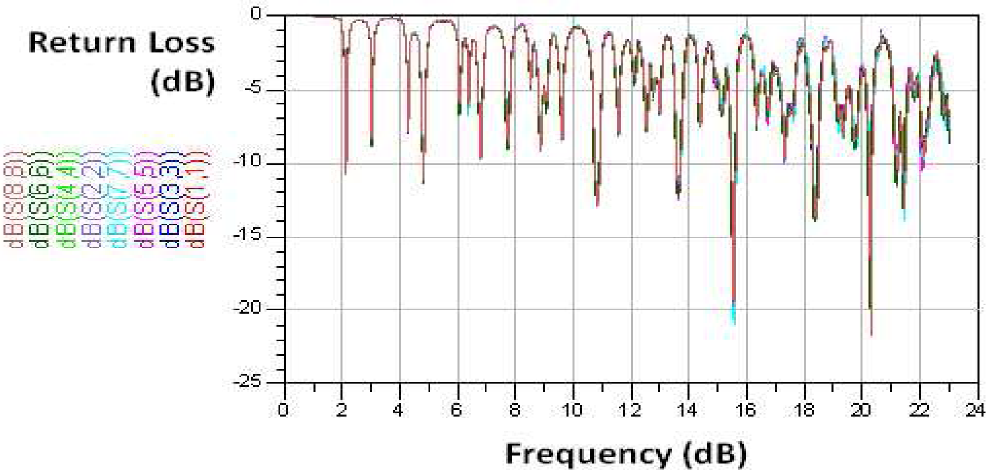

(a)

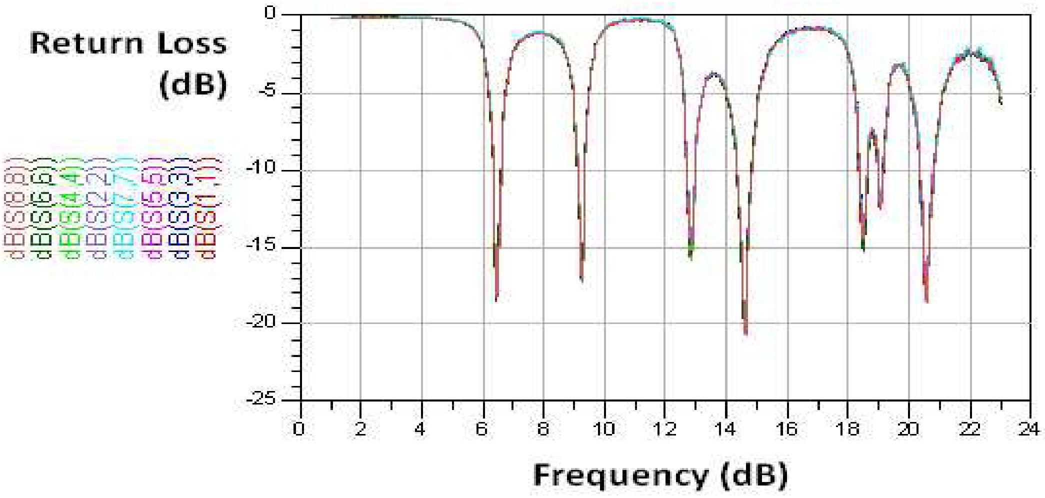

(b)

Figure 25. Measured return loss of four samples from (a) resonator 1 and (b) resonator 3.

The extraction of the relative permittivity and that of the loss tangent from 1 to 67 GHz for four samples are presented in Figure 26 and Figure 27, respectively. The extracted relative permittivity of the ceramic substrate is 5.432 ± 0.068 from 1 GHz up to 67 GHz. The loss tangent is less than 0.0055 over the [1-67] GHz frequency range. The results are consistent for the four samples, showing accuracy and repeatability of the proposed extraction method.

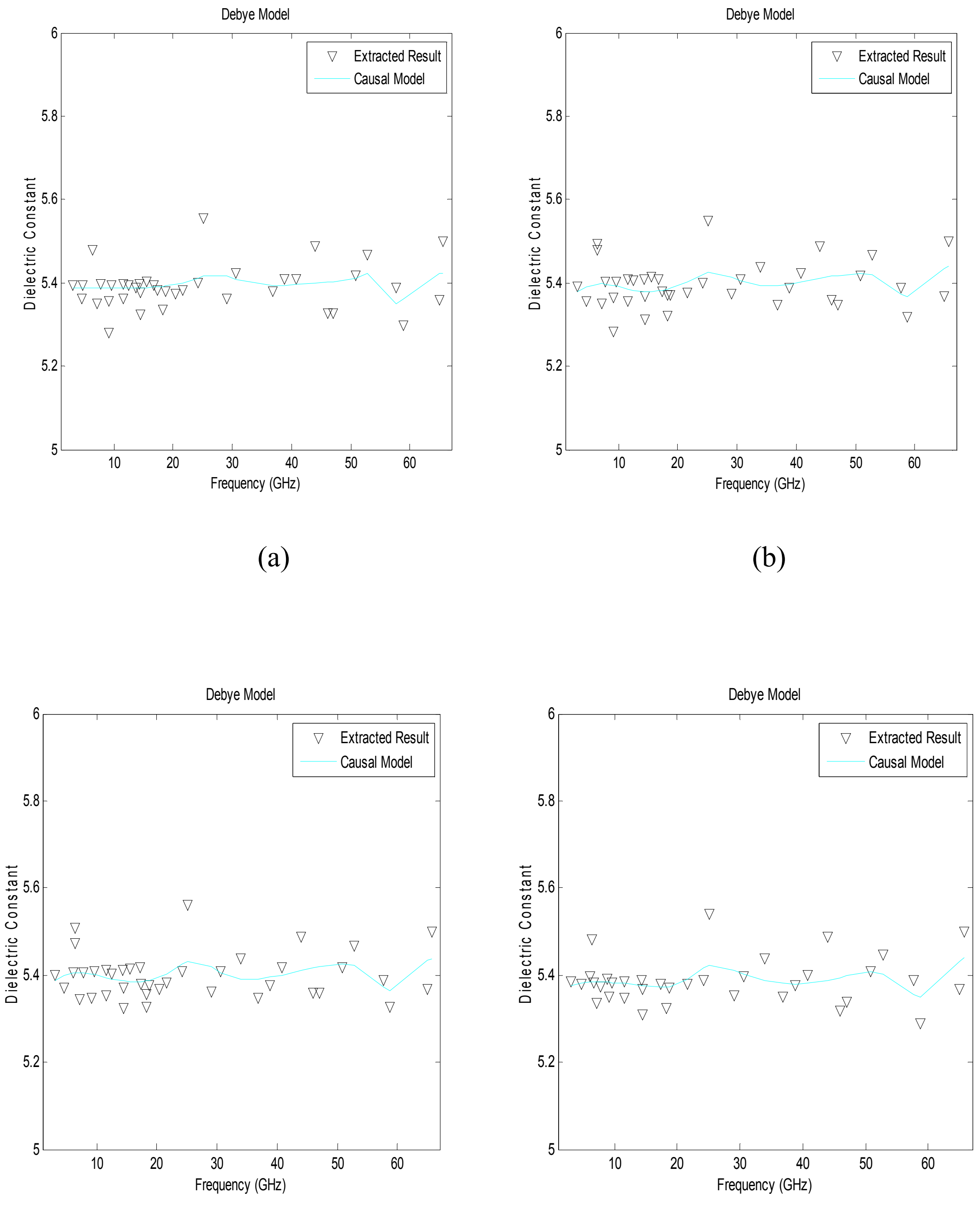

(a)

(b)

(c)

(d)

Figure 26. Extracted dielectric constants. (a) Sample1 (b) Sample2 (c) Sample3 (d) Sample4

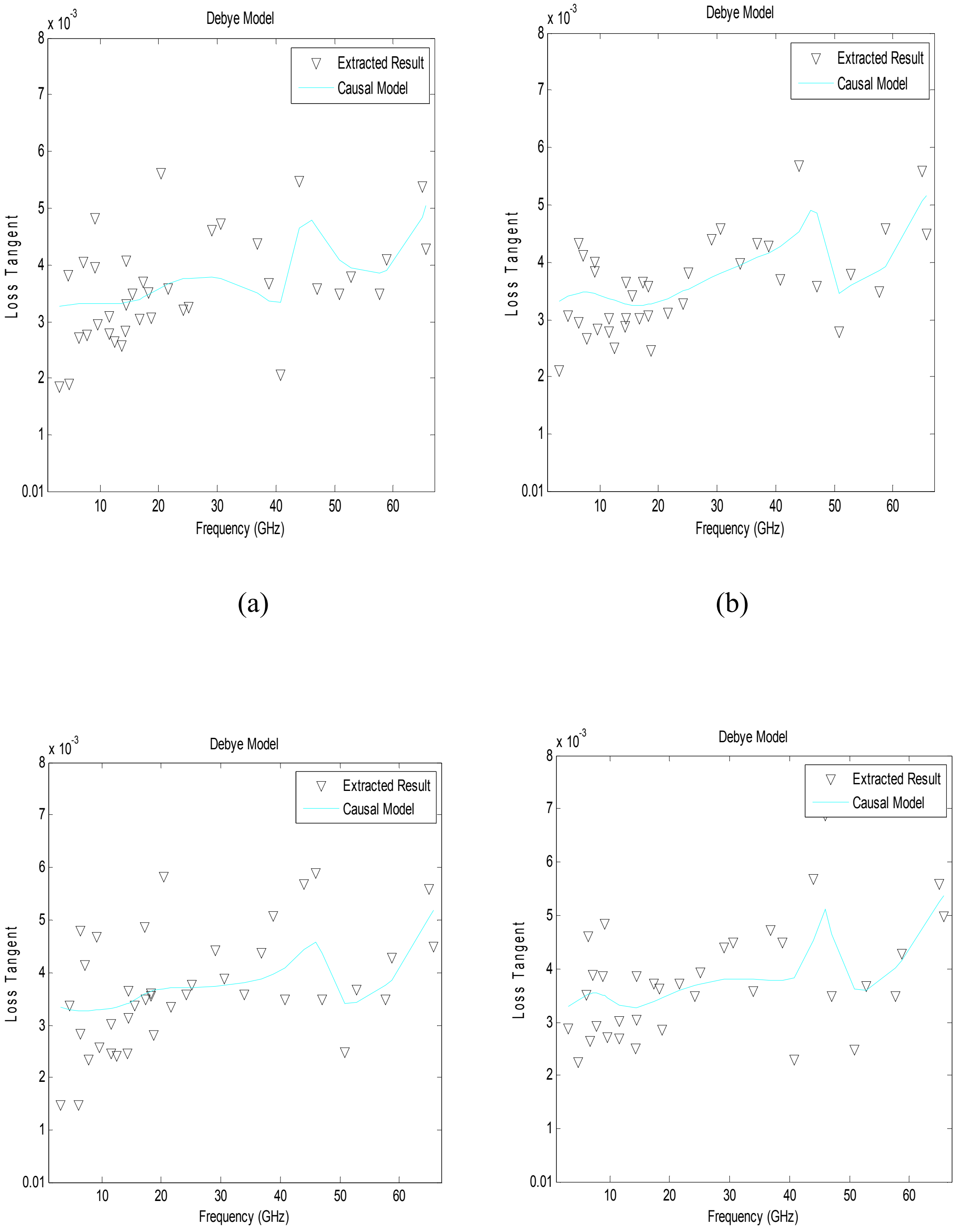

(a) (b)

(c) (d)

Figure 27. Extracted loss tangents. (a) Sample1 (b) Sample2 (c) Sample3 (d) Sample4

2.2.4 Extraction of High-Loss Material Property up to 67 GHz

The proposed extraction method has been used to extract the property of low-loss organic and ceramic materials. Although many of the extraction methods are limited to specific type of material type because of measurement or fabrication limitations, the proposed parallel-plate resonator method can be applied to various types of material because of structure simplicity. Hence, a high-loss material has been characterized to extract the dielectric properties (relative permittivity and loss tangent) from 1 to 67 GHz. Seven parallel-plate resonators have been designed and are presented in Figure 28. Their dimensions are respectively:

- Resonator 1: 10 mm x 10 mm; Resonator 2: 5 mm x 5 mm;
- Resonator 3: 4 mm x 4 mm; Resonator 4: 3 mm x 3 mm;
- Resonator 5: 2.4 mm x 2.4 mm; Resonator 6: 2 mm x 2 mm;
- Resonator 7: 1.6 mm x 1.6 mm.

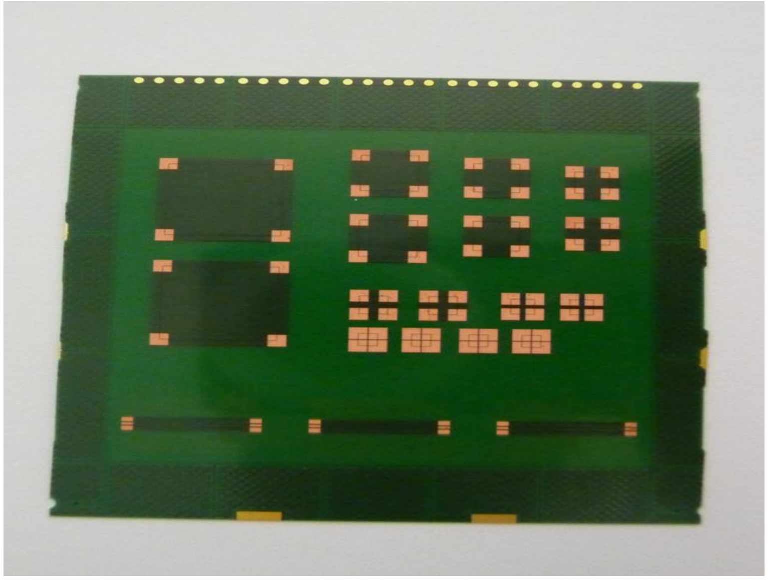

Figure 28. The resonator layout for high-loss material.

Once the SOLT calibration is performed for each of the frequency range, the probes are landed at two opposite corners of the cavity resonators and the S-parameters are recorded as touchstone file. Figure 29 shows the measurement set-up with the 10 mm x 10 mm resonator.

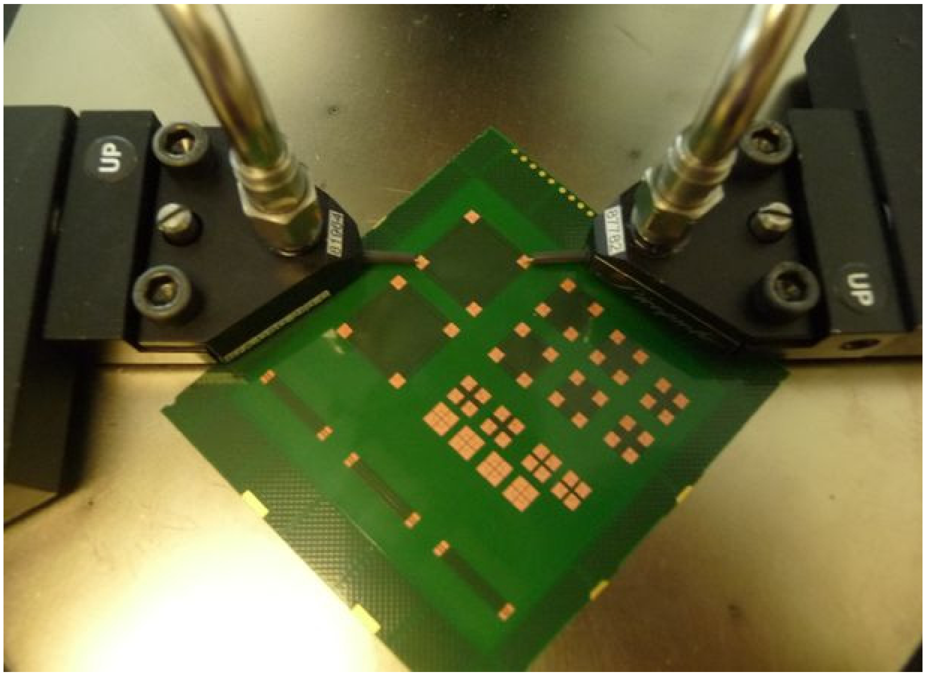

Figure 29. Corner-to-corner probing.

The wider resonators are more suitable at the lower frequencies since they provide numerous resonances compared to smaller resonators. Figure 30 illustrates this by comparing the measured results of resonators 1 (10 mm by 10 mm) and 3 (4 mm by 4mm), from 1 to 30 GHz. As for Figure 31 to Figure 32, they show the transfer impedance measured for Resonator 1, and 5, respectively, from two different samples. Almost no variation is observed between the two different samples: this demonstrates the consistence of the measured results and the quality of the fabrication.

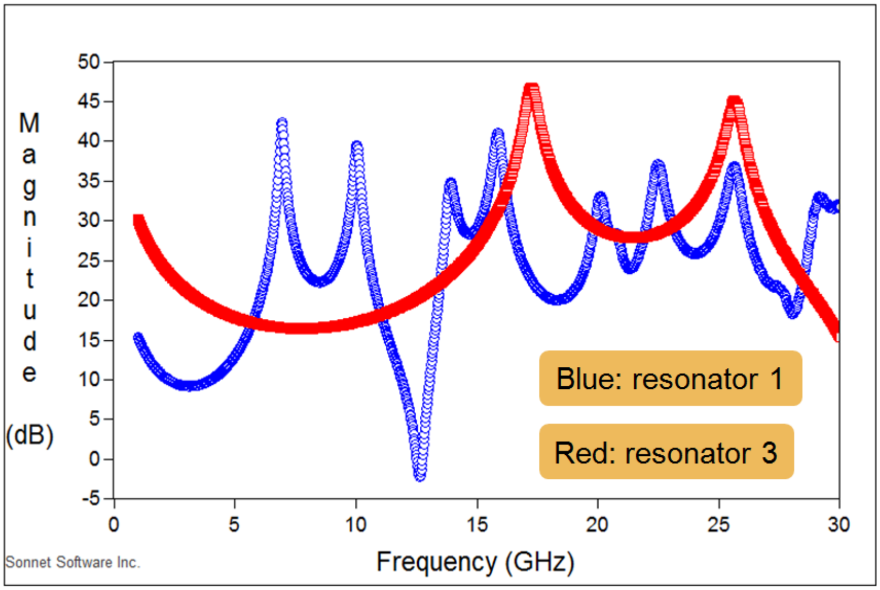

Figure 30. Comparison between resonator 1 and resonator 3.

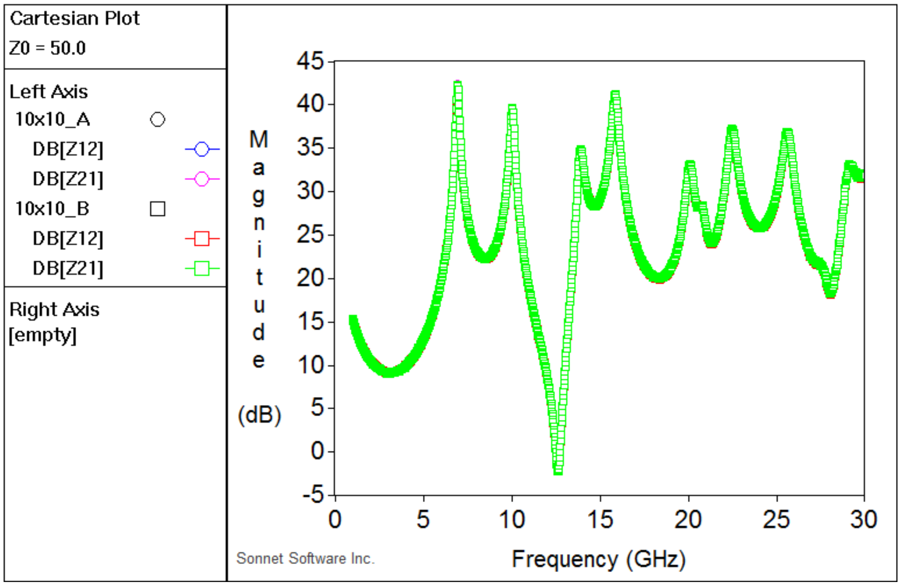

Figure 31. Measured transfer impedance of resonator 1 from two samples.

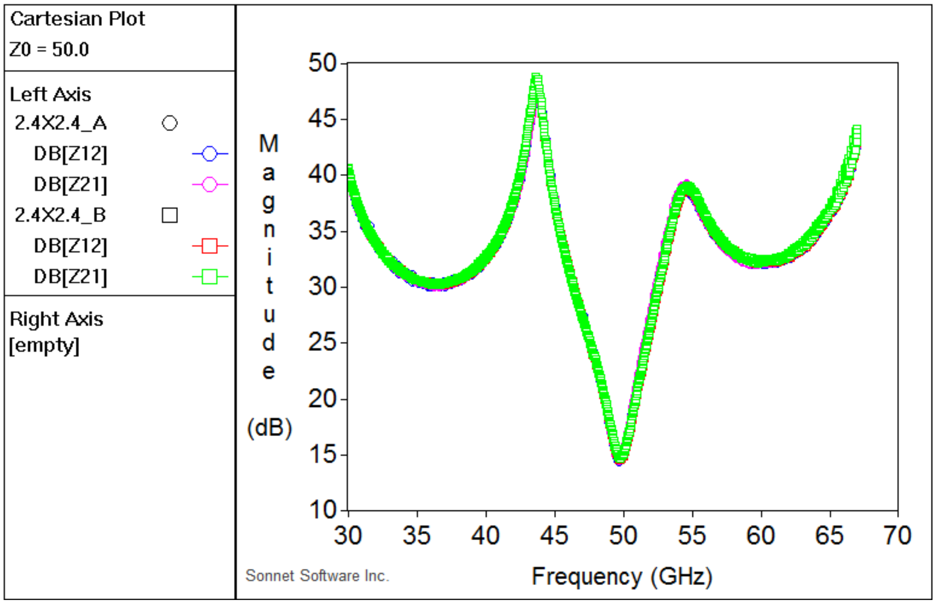

Figure 32. Measured return loss of resonator 5 from two samples.

Total of 7 resonators from two different samples have been measured and characterized, and the extraction results of the relative permittivity and the loss tangent from 1 to 67 GHz are obtained. In high frequency measurement environment, measurement errors cannot be avoided because of calibration limitations. That is, the measurement data may not be stable or violate causality. Therefore, Debye model, described in section 2.2.2, is also constructed. The results of the vector fitting can be used in EM simulator to obtain causal results. Extracted results and causal models are shown in Figure 33 and Figure 34 for each sample.

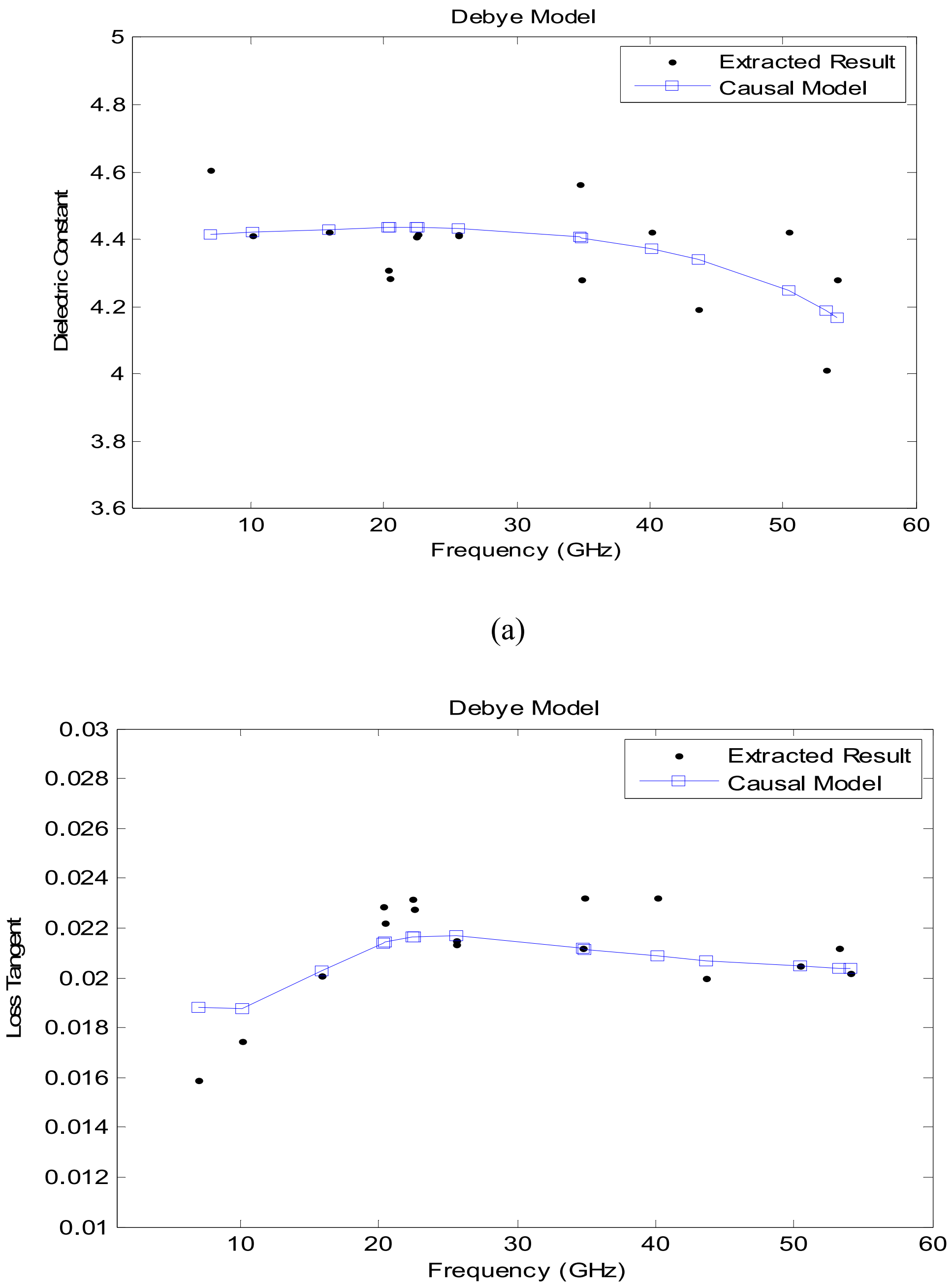

(a)

(b)

Figure 33. High-loss material extraction results from sample1. (a) Dielectric constant (b) Loss tangent

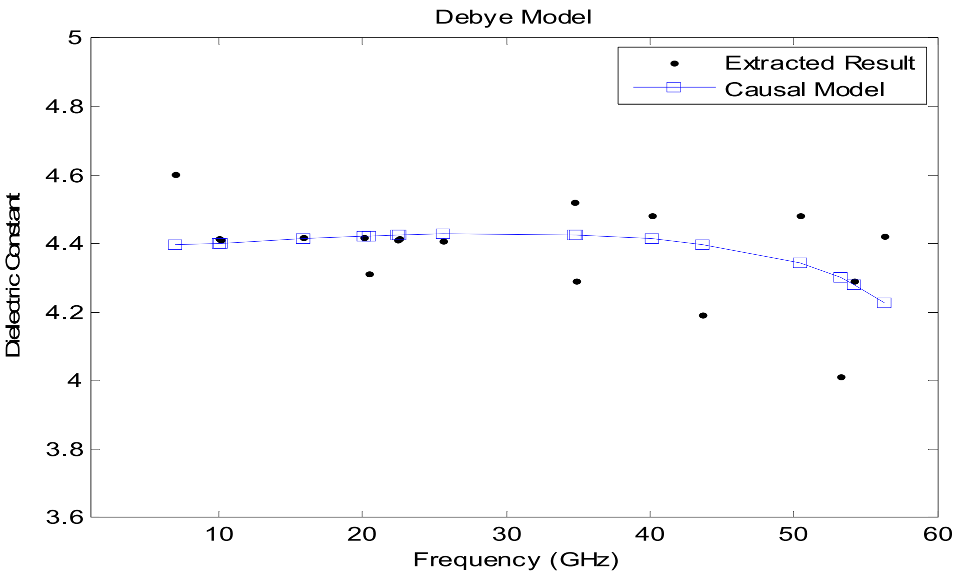

(a)

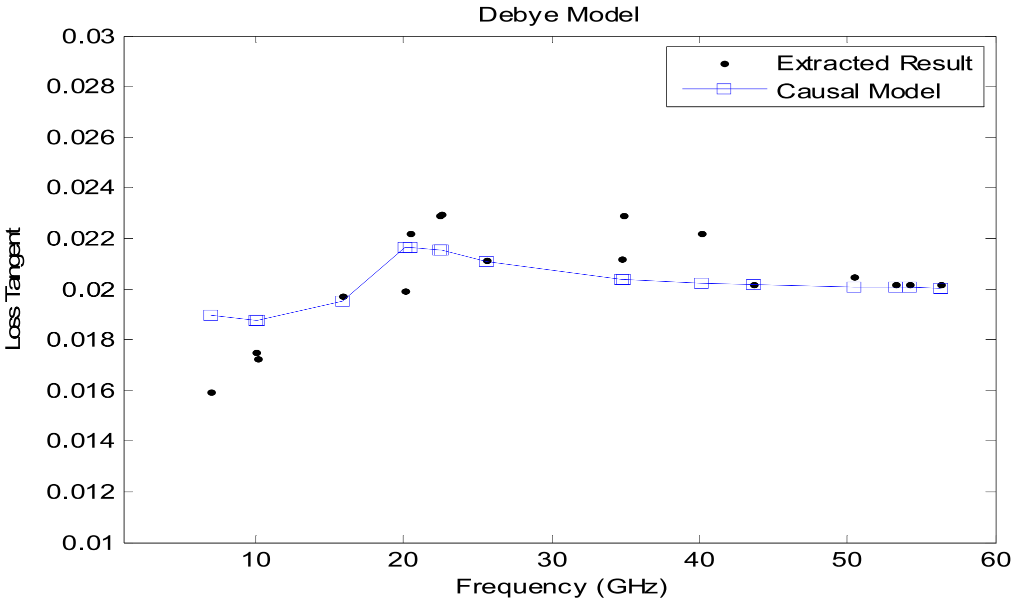

(b)

Figure 34. High-loss material extraction results from sample2. (a) Dielectric constant (b) Loss tangent

The results are consistent for the two samples. The extracted relative permittivity of sample1 is 4.305 ±0.295 from 1 GHz up to 67 GHz while sample2 has 4.306 ±0.295. Both materials have loss tangent of 0.016 at low frequency, which goes up to 0.0232 for sample1 and 0.0229 for sample2.

2.3 Summary

This chapter presented an efficient and accurate method for extracting frequency-dependent material properties such dielectric constant and loss tangent, which are critically important for transmission line behavior in terms of the signal integrity as well as the passive circuits design. The proposed extraction algorithm provides an efficient extraction process, which enables to handle a large number of samples to extract the material property. Moreover, inclusion of the surface roughness factor into the conductor-loss formulation enhances the confidence level of frequency-dependent loss tangent extraction results.

To validate the proposed method, three different material properties were extracted. For the first time, the dielectric properties of next generation thin low-k and low-loss RXP materials were successfully characterized from 1 GHz to 110 GHz. The extracted dielectric constant of RXP1 was 3.41±0.06 and loss tangent has values between 0.0037-0.006 from 1 to 110 GHz. For RXP4, the extracted dielectric constant was 2.98±0.05 while loss tangent has values between 0.004-0.0053 up to 110 GHz. A causal model for the dielectric parameters was successfully constructed from the extracted results, which includes the surface roughness effect. Based on the results, RXP materials can be used in wireless applications since they have stable and good high frequency properties. Figure 35 shows a material property comparison between RXP and LCP.

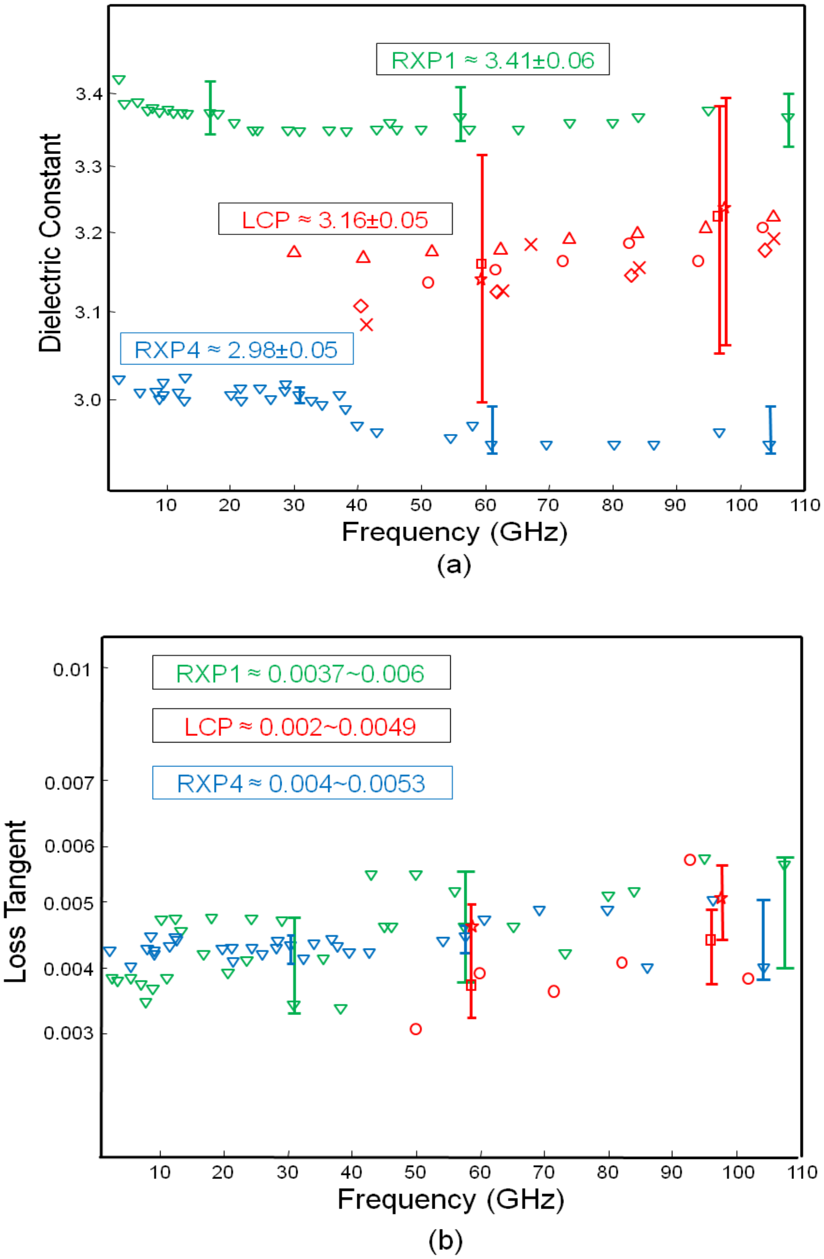

Figure 35. Material property of LCP and RXP up to 110 GHz: (a) dielectric constant, and (b) loss tangent. (Green: RXP1, blue:RXP4, red: LCP [24])

The material properties of ceramic and high-loss materials were extracted from 1 to 67 GHz. To validate the measurement and fabrication accuracy, more than two samples of the same resonator were measured and characterized. The resulting measurement and extraction results showed almost no variation between each samples, showing the accuracy and repeatability of the proposed method. Therefore, the proposed method can be readily applied to various types of the material characterization with high accuracy.

CHAPTER 3

EMBEDDED WLAN BANDPASS FILTERS

Multimedia systems have dramatically evolved using innovative system integration technologies by providing thinner and smaller form factor, lower cost, more functionality, and lower power consumption for next generation mobile applications [3]. One of the system integration technology, system-on-package (SoP), has provided better system integration capabilities with good RF performances by embedding actives and passives into a low-loss organic substrate [6]. In SoP, low temperature co-fired ceramic (LTCC) technology having high dielectric constant and low-loss has provided system integration solutions for microwave and millimeter-wave applications. However, LTCC technology may not necessarily provide a long-term effective packaging solution because of difficulty of embedding actives, thicker substrate, higher processing temperature (> 900 °C), larger weight, and higher cost as compared to organic technologies. These barriers led to the development of organic-based SoP solutions. Over last few years, liquid crystal polymer (LCP) organic-based SoP technology has been considered as a promising candidate for system integration in a package because of its superior electrical properties up to millimeter-wave frequencies [24]. Nonetheless, LCP technology also requires a relatively higher processing temperature (290 °C) than FR-4 and has manufacturing variation issues due to bondply material misalignment, which can be a bottleneck for low-cost system integration.

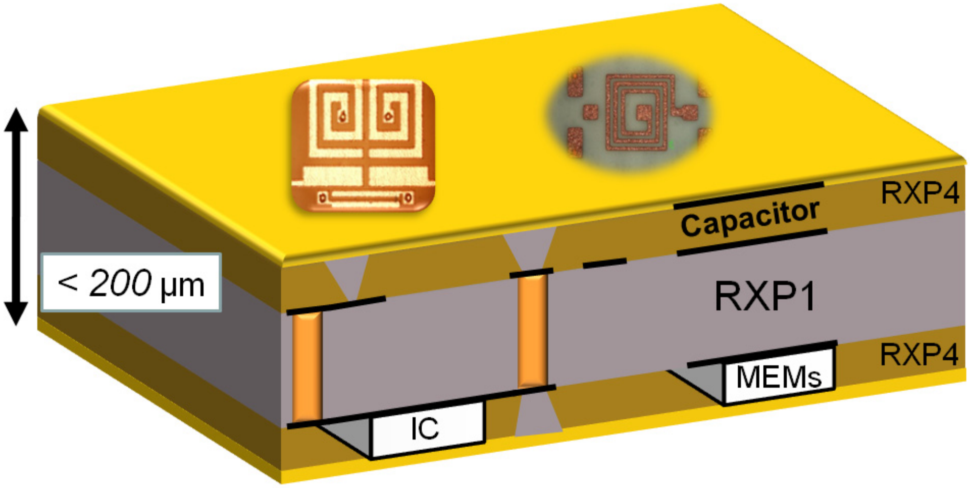

Figure 36. Embedded passive and active module using RXP.

Recently, ultra-thin organic low-K and low-loss dielectric called RXP has been developed and characterized to reduce layer count and eliminate build-up layer processing in order to significantly reduce the substrate cost [40, 71, 72]. Unlike LCP technology, RXP can be made ultra-thin under low processing temperature (220 °C), which is compatible with standard printed circuit board manufacturing processes. RXP supports ultra fine-pitch wiring with low surface profile copper and enables integrated circuits (ICs), MEMS devices, and 3D ICs with blind microvias to be embedded in the substrate as shown in Figure 36. Details regarding material properties and the fabrication processes of RXP can be found in [40, 72].

Wireless communication systems have been the most active part of modern electronics for the last few decades. This has led to the development of wireless communication standards such as GSM, W-CDMA (2.1-2.17 GHz), WLAN (2.4-2.48 & 4.9-5.9 GHz), WiMAX, and so on. Among the wireless standards, wireless local area network (WLAN or Wi-Fi) has received special interest because of its unlicensed band and emerging mobile applications such as smart phones and mobile netbooks. High rejection bandpass filter (BPF) is a key component to achieve high performance for mobile applications. The IEEE 802.11g (2.4 GHz) standard was established for higher band operation and better performance [57]. Recently, IEEE 802.11n (2.4 and/or 5 GHz) standard was proposed, which is almost ten times faster than 802.11g.

As the operating frequency of existing wireless standards comes close and multiple standards are integrated into a package, high stopband rejection as well as low inband insertion loss in the transmitting and receiving paths is crucial for use in low-power wireless products supporting multiple wireless standards. For instance, more than 20 dB attenuation beyond 230 MHz out of the WLAN passband (2.4 GHz) is necessary to block the interference from W-CDMA (2.17 GHz). Therefore, the design requirements for BPFs become more difficult for suppressing unwanted frequency signals including harmonics, image, and inter-modulation signal or blocking the interference from other wireless standard bands.

This chapter focuses on the design of high-rejection bandpass filters for the WLAN application in RXP substrate. Six different bandpass filters were designed, fabricated, and measured in RXP. High-rejection bandpass filter topologies for narrow (2.4 GHz) and wide (5 GHz) bands are discussed in Section 3.1. Next, filter design methodology and RXP design rule and stack-up are presented in Section 3.2. Novel 3D stitched capacitor is proposed in Section 3.3, and measurement results of the proposed WLAN bandpass filters are presented in Section 3.4.

3.1 High-Rejection Bandpass Filter Topologies

3.1.1 Narrow-Band Bandpass Filter Topology

Figure 37 shows the conventional second-order capacitively- coupled topology and its frequency response [73]. Unless the size of filter is increased, the conventional topology cannot satisfy demanding high-rejection specifications because the slope of the stopband is directly related to the order of filter (number of *L*C resonator tank circuits). For instance, WLAN requires more than 25 dB attenuation at 2.17 GHz where W-CDMA operates. Assuming the insertion loss is 1.5 dB at 2.4 GHz, the slope of low stopband requires 10.22 dB per 100 MHz to meet this rejection requirement. As shown in Figure 37 (b), the conventional topology cannot meet this steep slope requirement. The simplest way to improve rejection with a minimum order of the filter is to introduce a transmission zero. The conventional way to have a transmission zero is to add a LC tank circuit with inductor and capacitor in parallel. However, this increases the size of the filter. Therefore, the conventional topology is modified to have an additional grounding inductor (L_G) as shown in Figure 38 (a).

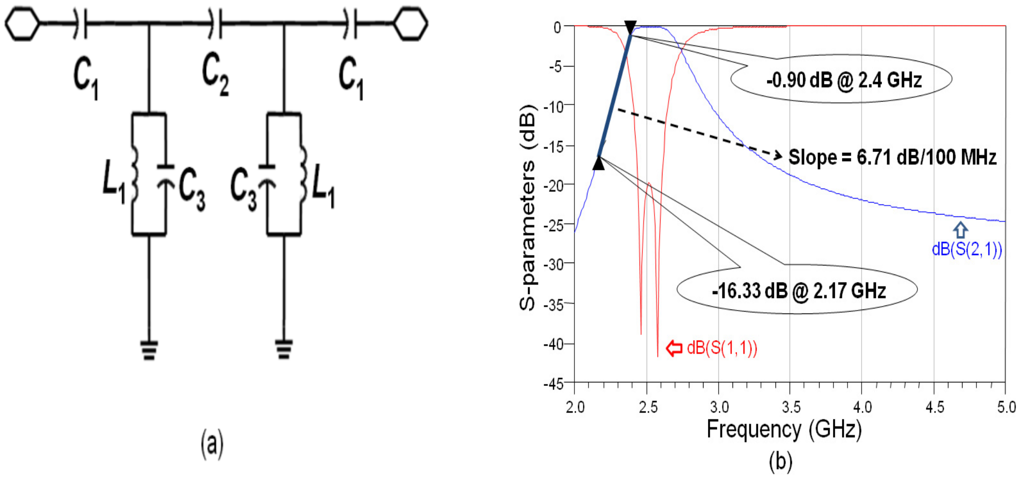

Figure 37. (a) Conventional capacitively-coupled topology. (b) Frequency response.

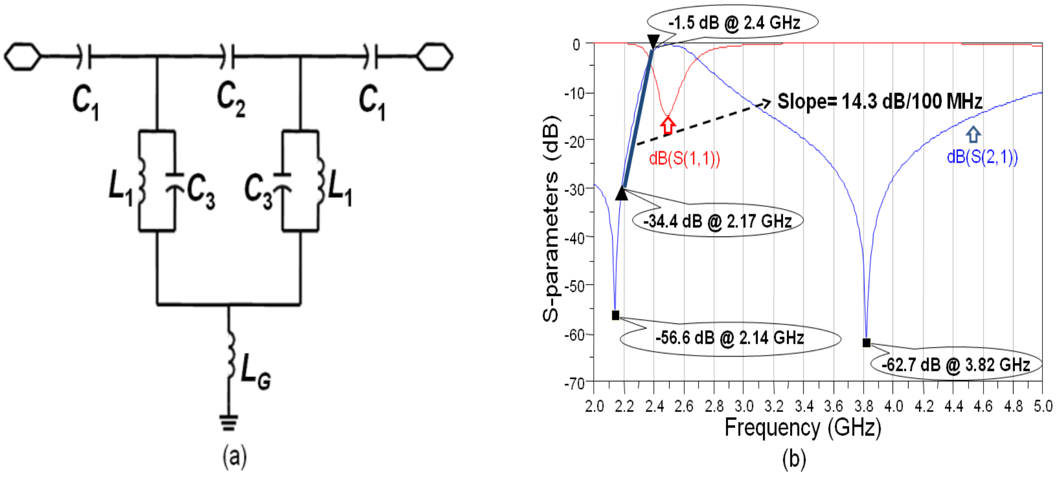

Figure 38. (a) Modified topology with grounding inductor. (b) Frequency response.

By adding the grounding inductor, a finite transmission zero can be produced to improve the stopband rejection. Without increasing the order of the filter, the slope of the modified topology has been much steeper than the conventional topology as shown in Figure 38 (b). Moreover, the grounding inductor is an essential element in multilayer design because the ground is connected through via connection, which can be implemented as an inductance. Hence, inductor L_G does not increase the size.

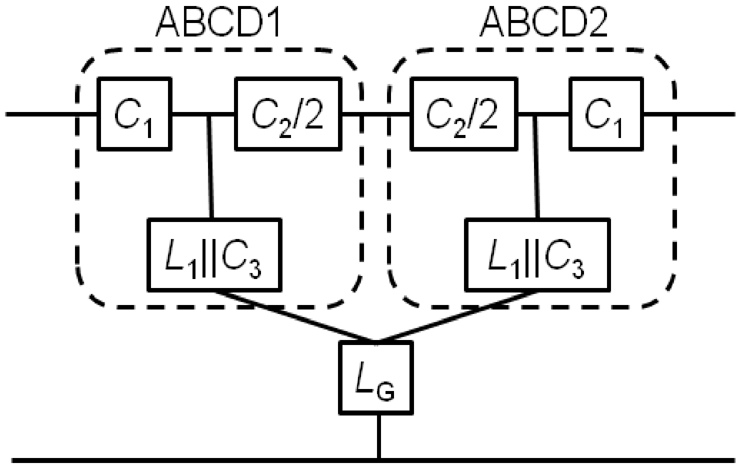

Figure 39. Equivalent circuit for modified topology.

Design equations for calculating the component values of the capacitively-coupled filters can be derived by using standard filter synthesis procedures [73]. Before calculating the component values, the fractional bandwidth of the passband and admittance inverter can be defined as

$$\Delta = \frac{f_2 - f_1}{\sqrt{f_2 \cdot f_1} = f_0} \tag{8}$$

$$J_{01} = \frac{1}{Z_0}\sqrt{\frac{\pi \cdot \Delta}{4 \cdot g_1}} \tag{9}$$

where f_1 and f_2 denote the edges of the passband, f_0 is the center frequency, g_n are either Butterworth or ChebyShev constants, and Z_0 is the characteristic impedance.

The synthesis begins with selection of the inductor L_1. The inductance value L_1 is generally chosen to have a maximum realizable quality factor depending on the substrate and fabrication technology. For RXP technology, is has been shown that inductor quality factor has a range of 70~100 from 2 to 5 GHz [38]. Then, the capacitance values are computed using

$$C_1 = \frac{J_{01}}{\omega_0\sqrt{1-(Z_0 \cdot J_{01})^2}} \tag{10}$$

$$C_2 = \frac{\Delta}{8 \cdot f_0 \cdot Z_0\sqrt{g_1 \cdot g_2}} \tag{11}$$

$$C_3 = \frac{1}{L_1 \cdot \omega_0^2} - \frac{C_1}{1+(\omega_0 \cdot C_1 \cdot Z_0)^2} - C_2 \qquad (12).$$

To find the grounding inductor L_G, the modified topology is represented as in Figure 39. Using ABCD matrix property and circuit symmetry, the conventional topology can be defined by multiplying ABCD1 and ABCD2 matrices

$$ABCD_{conv.} = \begin{bmatrix} A & B \\ C & D \end{bmatrix} = \begin{bmatrix} A_1 & B_1 \\ C_1 & D_1 \end{bmatrix} \cdot \begin{bmatrix} A_2 & B_2 \\ C_2 & D_2 \end{bmatrix} = \begin{bmatrix} A_1 & B_1 \\ C_1 & D_1 \end{bmatrix} \cdot \begin{bmatrix} D_1 & B_1 \\ C_1 & A_1 \end{bmatrix} \tag{13}$$

where $A_2=D_1$, $B_2=B_1$, $C_2=C_1$, $D_2=A_1$. Because the transmission zeros occur when $Z_{21}= 0$ and transfer impedance (Z_{21}) from ABCD matrix can be found as the inverse of C, the transfer impedance for the conventional topology can be expressed as

$$Z_{21} = \frac{1}{C} = \frac{1}{2 \cdot C_1 \cdot D_1} \tag{14}$$

$$C_1 = \frac{1+s^2 \cdot L_1 \cdot C_3}{s \cdot L_1} \tag{15}$$

$$D_1 = \frac{s^2 \cdot L_1(2 \cdot C_2 + C_3) + 1}{2 \cdot s^2 \cdot C_2 \cdot L_1} \tag{16}$$

Then, the total transfer impedance for the modified topology can be found by adding L_G to the transfer impedance. Therefore, the grounding inductor can be calculated depending on the desired transmission zero locations using

$$Z_{21,Total} = \frac{1}{2 \cdot C_1 \cdot D_1} + s \cdot L_G = 0 \tag{17}$$

$$L_G = \left| \frac{s^2 C_2 L_1^{\,2}}{(1 + s^2 L_1 C_3) \cdot (s^2 L_1 (2C_2 + C_3) + 1)} \right| \tag{18}$$

where the location of finite transmission zeros will be the two positive roots of the polynomial in (18). Alternatively, they can be obtained by solving (17) graphically.

3.1.2 Wide-Band Bandpass Filter Topology

Capacitively-coupled topology is suitable for a narrow band filter implementation that has relatively steeper low stopband-rejection than high stopband. The 5 GHz filter operates at much wider bandwidth (> 1GHz) than 2 GHz (< 200 MHz) and has more rejection requirements: 25 dB attenuation at 4.4 GHz where military spectrum bands and 7.2 GHz where 3rd harmonic exists. Hence, a different topology with more transmission zeros is needed. In this regard, the proposed topology to be implemented is shown in Figure 40. It consists of second-order unique resonators with grounding inductor and feedback capacitor (C_2).

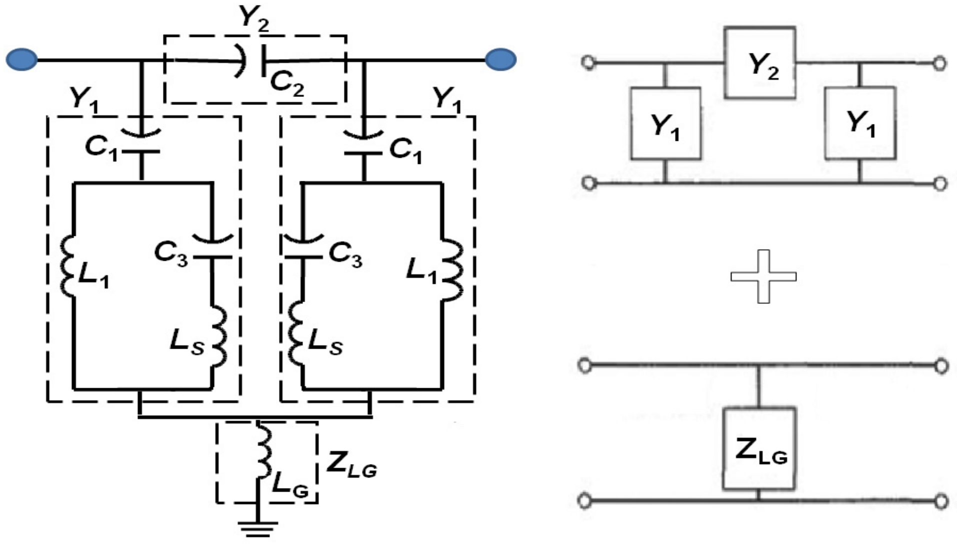

(a) (b)

Figure 40. (a) Unique resonator with grounding inductor. (b) Its equivalent circuit.

It has been shown that the circuit topology in Figure 40 (a) without series inductors (L_S) and grounding inductor (L_G) produces two transmission zeros from C_2 mutual coupling of inductors L_1 [20]. However, the rejection requirements cannot be satisfied with only two transmission zeros without sacrificing the bandwidth and insertion loss. Moreover, the mutual coupling requirement to produce transmission zeros may not be realizable. Therefore, additional series inductors along with the grounding inductor have been added to introduce more transmission zeros. It should be noted that the proposed topology does not require mutual coupling between L_1. Instead of the mutual coupling, the topology employs the series inductors producing the high stopband transmission zero. These additional series inductors, in fact, are necessary for the multilayer organic BPF layout design. For instance, a capacitor can be readily realized by using parallel-plates on two different layers. To make a connection from the capacitor to other element such as inductor, the layout requires an interconnect or via that can be represented as an inductance at microwave frequency. Therefore, L_S can be used as a design parameter, which serves as an interconnect or via without increasing size of the layout. Likewise, L_G can be used as a grounding connection through a ground layer since there must be at least one grounding connection from the BPF layout to the ground layer in multilayer design.

The capacitors C_1, C_3 can be computed by using (10) and (12), and C_2 can be obtained from [20]. To find series and grounding inductor values, the whole part of the circuit except L_G can be transformed to π-network as shown in Figure 40 (b). The series inductor is related to upper stopband transmission zero. Therefore, L_S can be found from

$$L_s = (\frac{1}{2\pi f_{uz}})^2 \times \frac{C_1 + C_3}{C_1 C_3} \tag{19}$$

where f_{uz} is the frequency of the upper stopband transmission zero. To include the grounding inductor to the π-network, the admittance matrix (π-network) is converted into an impedance matrix. Then, the overall impedance matrix for the proposed topology is the sum of π-networks in series with the grounding inductor. Hence, the overall impedance matrix can be represented as

$$Z_{LG} = \begin{pmatrix} sL_G & sL_G \\ sL_G & sL_G \end{pmatrix} \tag{20}$$

$$Z_{\pi-network} = \begin{pmatrix} \frac{Y_1 + sC_2}{D} & \frac{sC_2}{D} \\ \frac{sC_2}{D} & \frac{Y_1 + sC_2}{D} \end{pmatrix} \tag{21}$$

$$Z_{total} = Z_{\pi-network} + Z_{LG} = \begin{pmatrix} sL_G + \frac{Y_1 + sC_2}{D} & sL_G + \frac{sC_2}{D} \\ sL_G + \frac{sC_2}{D} & sL_G + \frac{Y_1 + sC_2}{D} \end{pmatrix} \qquad (22)$$

where $s = j\omega$, Y_1 is the sum of the admittance from C_1 and resonator tank circuit, and $D = Y_1^2 + 2Y_1C_2s$. Since the transmission zeros occur when $Z_{21} = 0$, the grounding inductor can be calculated by setting $Z_{21} = 0$

$$sL_G + \frac{sC_2}{D} = 0 \qquad (23)$$

$$Y_1^2 + 2Y_1C_2s + \frac{C_2}{L_G} = 0 \qquad (24)$$

$$L_G = \frac{C_2}{-Y_1^2 - 2Y_1C_2s} \qquad (25)$$

$$Y_1 = \frac{sC_1(s^2C_3(L_1 + L_S) + 1)}{s^2C_3(L_1 + L_S) + sC_1(sL_1(s^2C_3L_S + 1)) + 1} \qquad (26).$$

The location of multiple finite transmission zeros will be the positive roots of the polynomial in (24). Therefore inductor L_G can be obtained depending on the desired transmission zero locations by using (25).

To show L_G behavior on transmission zero locations, a second-order bandpass filter centered at 5.3 GHz has been designed by using the topology shown in Figure 40. The corresponding circuit element values are C_1=1.50 pF, C_2=0.78 pF, C_3=0.43 pF, L_1=0.76 nH, and L_S=1.06 nH. The curves without circles ($S21_B$, $S11_B$) in Figure 41 show the designed filter response without the inductor L_G, and the curves with circles ($S21_A$, $S11_A$) show the filter response after including the inductor L_G. The TZ_1 to TZ_4 points represent the transmission zero frequencies from the first to the fourth transmission zero.

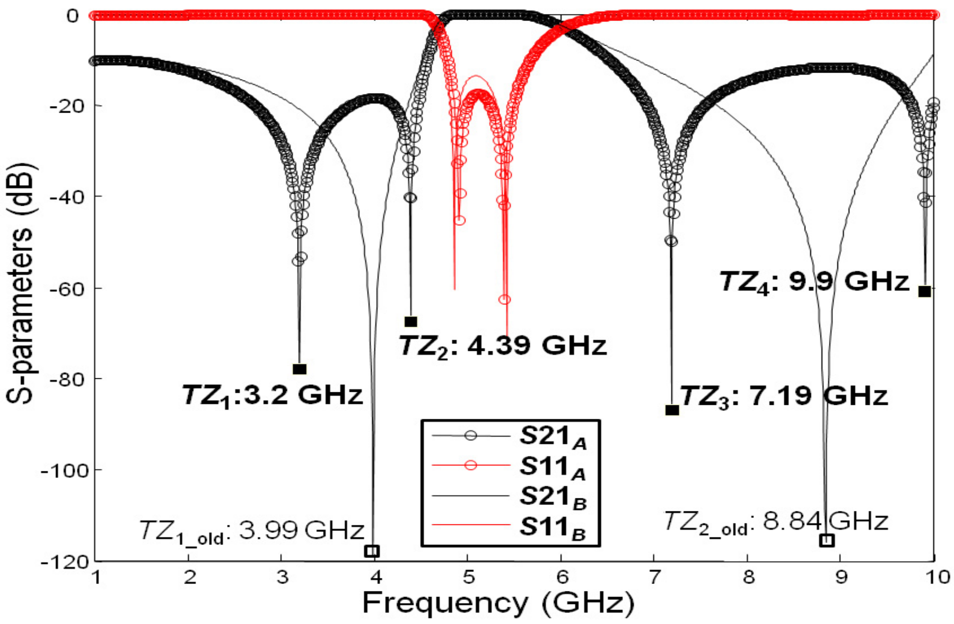

Figure 41. Filter response in S-parameters.

As shown in Figure 41, $S21_B$ has two transmission zeros at 3.99 and 8.84 GHz. After the inductor L_G is included, the filter response shows sharper rejections with four transmission zeros at 3.2, 4.39, 7.19, and 9.9 GHz. It is important to note that the passband and center frequency of the BPF response have not changed by including the inductor L_G.

In addition, the impedance matrix (22) can be used to predict the passband region. The insertion loss (S_{21}) is expressed in terms of the impedance matrix

$$S_{21} = \frac{2Z_{21}Z_0}{Z_{11}{}^2 + Z_0{}^2 + 2Z_{11}Z_0 - Z_{21}{}^2} \tag{27}$$

and setting Z_{11}=Z_{21}, (15a) becomes

$$S_{21} = \frac{2Z_{21}Z_0}{Z_0{}^2 + 2Z_{11}Z_0} \quad (28).$$

When $Z_0^2 << 2Z_{11}Z_0$, S_{21} becomes one. Therefore, the passband region can be predicted by observing points from Z-parameter frequency response where Z_{11} and Z_{21} cross with their magnitudes greater than $Z_0/2$. If the characteristic impedance is 50 Ω, the magnitude should be much greater than 27.96 dB.

The proposed circuit can also be graphically solved by using (23) to predict the location of transmission zeros as well as the passband region. To validate (23) and the passband prediction, transfer ($Z21$) and self ($Z11$) impedance from Z-parameter responses are shown in Figure 42 where TZ_1 to TZ_4 points represent the transmission zero occurring frequencies and P_1 and P_2 correspond to the start and stop passband frequency.

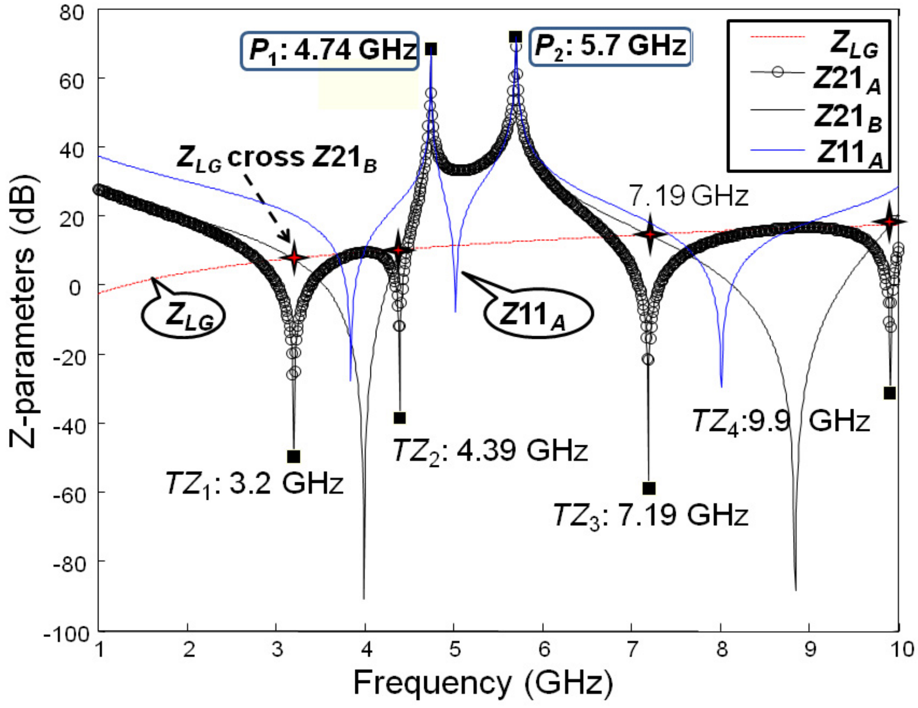

Figure 42. Location of transmission zeros and passband from Z-parameter of filter response.

According to (23), the transmission zeros occur when $Z21_B$ (transfer impedance before adding L_G) crosses the frequency response from Z_{LG}. Figure 42 clearly shows that the frequency points (cross marks) where Z_{LG} intersects $Z21_B$ correspond to exact transmission zero locations from $Z21_A$ (transfer impedance after adding L_G). Four sharp notches are generated at 3.2, 4.39, 7.19, 9.9 GHz, which are identical to the transmission zero location of filter response in Figure 41. Therefore, inductor L_G can be selected graphically depending on the desired locations of the transmission zeros. Moreover, points P_1 and P_2 where the $Z21_A$ intersects the $Z11_A$ represent the passband region (4.74 and 5.7 GHz) of the filter: their magnitudes much greater than 27.96 dB. It is important to note that intersection points from $Z21_A$ and $Z11_A$ that have magnitude smaller than 28 dB do not represent the passband region.

3.2 Filter Design Methodology and RXP Stack-Up

To demonstrate the performance of the proposed circuit schematic and RXP material, 2.4/5 GHz BPFs were designed using the circuit schematics shown in Figure 38 and Figure 40. First, each lumped-element values except the series and grounding inductors were calculated by the classical microwave design equations (8)-(12) [73]. Then, the series and grounding inductors were included by the proposed method so that the filter responses showed the sharp rejection at the stopband while they maintained good insertion and return loss with desired bandwidths. After obtaining all of the lumped-element values, each element was replaced by the corresponding layout. The physical layout was realized using RXP technology as shown in Figure 43. RXP stack-up has four-metal layers with total thickness of 0.191mm. The dielectric constant of RXP1 is 3.47 with loss tangent of 0.0043, and the dielectric constant of RXP4 is 3.03 with loss tangent of 0.0038 at 1 GHz. Details regarding material properties and fabrication processes of RXP can be found in [40, 72].

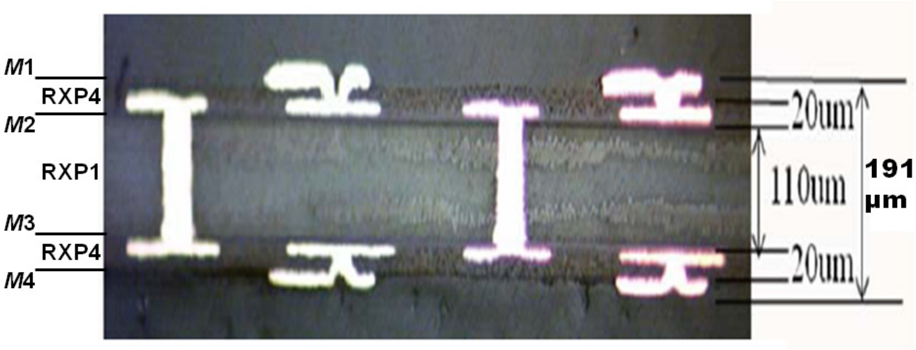

Figure 43. Cross section of RXP organic material.

With the multilayer capability of the RXP substrate, the lumped-elements can be readily realized by using a metal strip for the inductor and parallel-plates for the capacitor. Metal layers 1, 2, and 3 (*M1*, *M2*, and *M3*) were used to layout the components while metal layer 4 mainly served as the ground plane. The first completed layout was further refined to have better performance because parasitic effects and coupling from the close proximity between elements affected the designed performance. To reduce the design cycle, the proposed schematics in Section 3.1 were used to examine the behavior of lumped-elements so that only the corresponding inductors or capacitors could be modified in the layout for better performance. For instance, the center frequency is shifted if C3 value in Figure 40 is changed or bandwidth is changed if C2 value is changed. Therefore, each element behaviour can be studied in the circuit simulator, and then a necessary modification can be applied to the layout using a 3D EM solver, which significantly reduces the design-cycle time.

3.3 3D Stitched Capacitor

In addition to the proposed topology, the capacitor in the layout was designed using a stitched (3D inter-digitated) capacitor topology. The basic idea of the stitched capacitor is to combine the advantages of a 3D parallel-plate capacitor with a 2D inter-digitated capacitor. The first step for designing the stitched capacitor is to segment the parallel-plate capacitor into number of sections and then to stitch the segmented sections using vias to meet the required capacitance. The main advantage of this capacitor layout is **easy access to input/output ports and symmetrical shunt parasitic capacitances**. The stitched capacitor that provides the same shunt parasitic capacitance at input/output ports from the same layer is shown in Figure 44 (b).

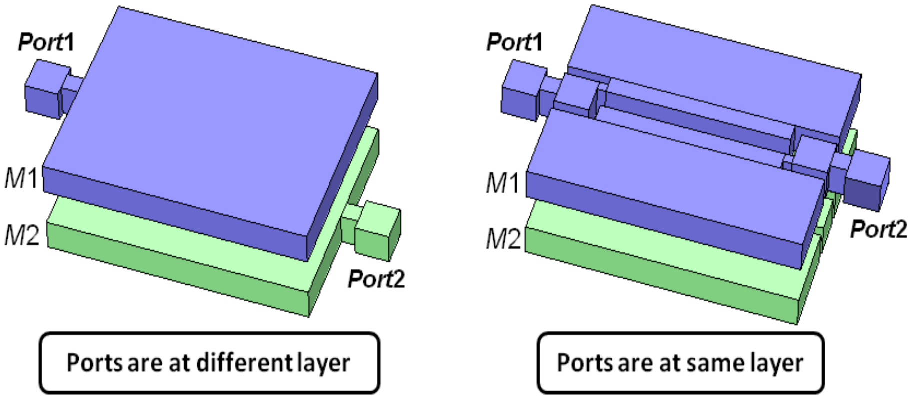

(a) (b)

Figure 44. (a) Parallel-plate capacitor and (b) stitched capacitor.

In the parallel-plate capacitor shown Figure 44 (a), the input and output ports (*port*1, *port*2) are always located on different layers, which results in uneven shunt capacitance parasitics and asymmetrical layout. For instance, the feedback capacitor (C_2) in Figure 40 is connected to *port*1 and *port*2 of BPF. If the feedback capacitor is designed using the parallel-plate capacitor, the interconnect from *port*2 of the feedback capacitor requires a via. Since only one side of the feedback capacitor has via inductance, the entire design becomes asymmetrical. Although the stitched capacitor requires two vias, the feedback capacitor implemented as stitched capacitor maintains the symmetry. Hence, it contributes towards improving the performance, especially insertion loss.

Figure 45 shows the pi model of two-port embedded passives in multilayer substrate. This model is useful for modeling of embedded passives at the frequency band below the self resonant frequency and for providing design insights without relying on complex equivalent circuit models. The Ca and Cb are shunt parasitics at input and output ports while Ce represents the capacitance. The circuits and quality factors (Ce, Ca, Cb | Qe, Qa, Qb) can be analytically extracted from simulated or measured scattering parameters [74].

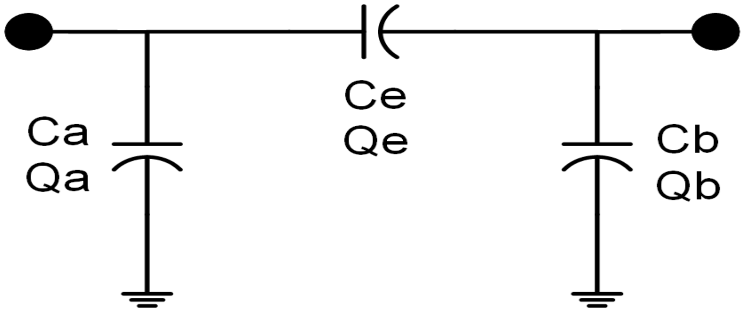

Figure 45. Pi model of two-port equivalent circuit model.

For demonstration of the stitched capacitor, a parallel plate capacitor and two stitched capacitors were designed and fabricated in RXP substrate. Three capacitors located on M1 and M2 with a ground plane on M4 were fabricated and measured. Figure 46 shows the top view of M1 and M2 metal layers and the X-ray photo of three capacitors. The measured capacitances Ce, Ca, Cb at 2 GHz are detailed in Table 5. As noted in Table 5, Ca is not equal to Cb for the parallel plate capacitor but Ca is close to Cb for two stitched capacitors. It should be also noted that the shunt parasitic capacitances of stitched capacitors are reduced to half of the parallel plate capacitor, which demonstrates that the stitched capacitor can alleviate shunt parasitics. A slightly smaller capacitance in stitched capacitors is due to the gaps and vias for stitching segmented sections.

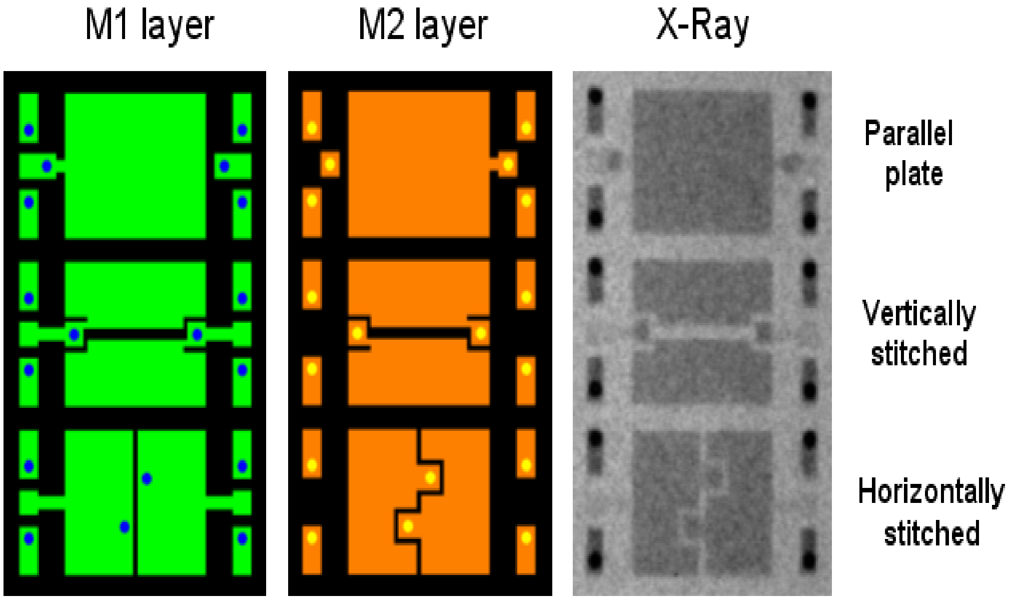

Figure 46. Parallel-plate and stitched capacitors.

Table 5. Measured parasitics and capacitances @ 2 GHz.

Capacitor	Ce (pF)	Ca (pF)	Cb (pF)	Note
Parallel Plate	2.96	0.05	0.58	Ca ≠ Cb
Vertically Stitched	2.65	0.29	0.31	Ca ≈ Cb
Horizontally Stitched	2.78	0.31	0.30	Ca ≈ Cb

Furthermore, the desirable shunt parasitics can also be obtained by controlling the bottom surface. Since both input/output ports can be accessed from the same metal layer, surface mountable devices can be directly mounted on the exposed top metal surface. For instance, stitched capacitors can be tuned and optimized by mounting additional capacitors, and resonators can be realized by mounting inductor. Moreover, it provides vertical routing flexibility by mounting interconnects such as bonding wires and bumps.

3.4 WLAN Bandpass Filter

3.4.1 Design of High-Rejection Second-Order WLAN Bandpass Filters

The proposed RXP BPFs have been fabricated by Packaging Research Center (PRC) at *Georgia Institute of Technology*. The fabricated RXP panel and BPFs prototypes based on the physical layouts are shown in Figure 47.

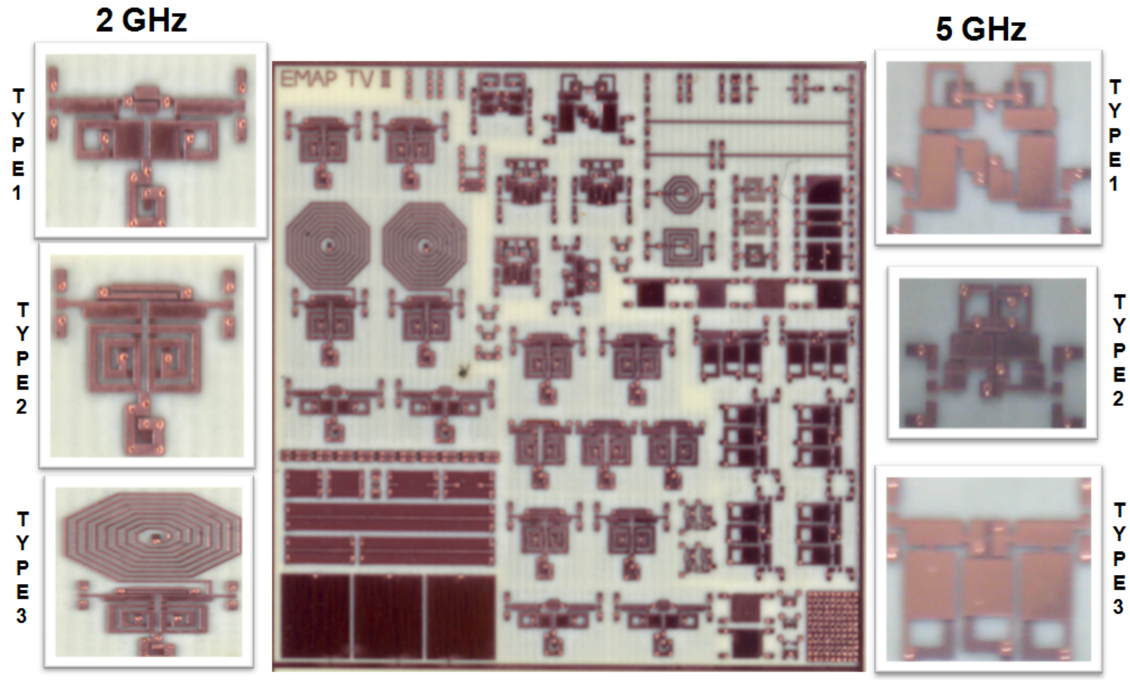

Figure 47. Fabricated RXP panel and 2 and 5 GHz BPFs images.

Figure 48 shows the physical layout of the organic BPFs embedded in a four-metal layer RXP substrate. The sizes of designed filters were 3.6 mm × 2.4 mm × 0.191 mm for 2 GHz and 2.55 mm × 2.45 mm × 0.191 mm for 5 GHz application.

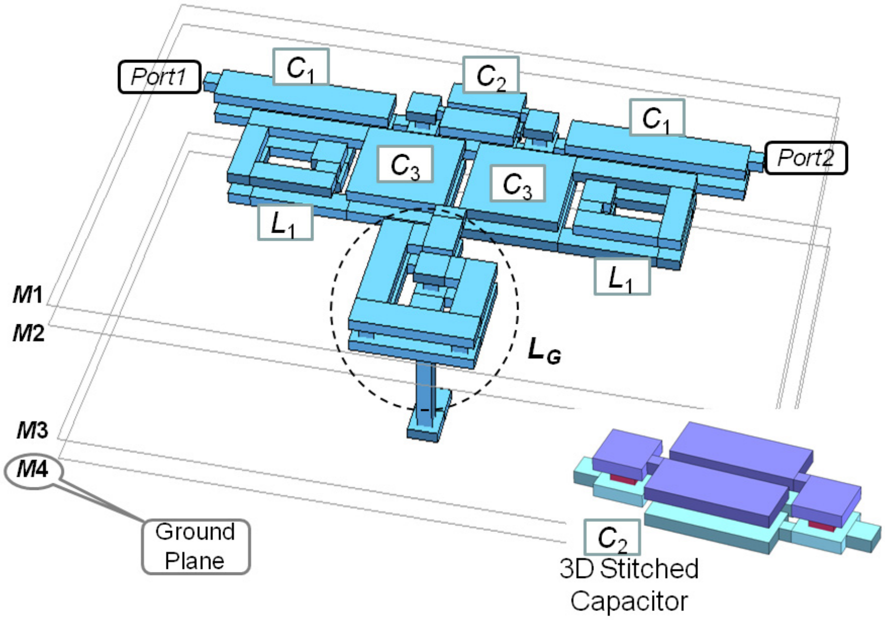

(a)

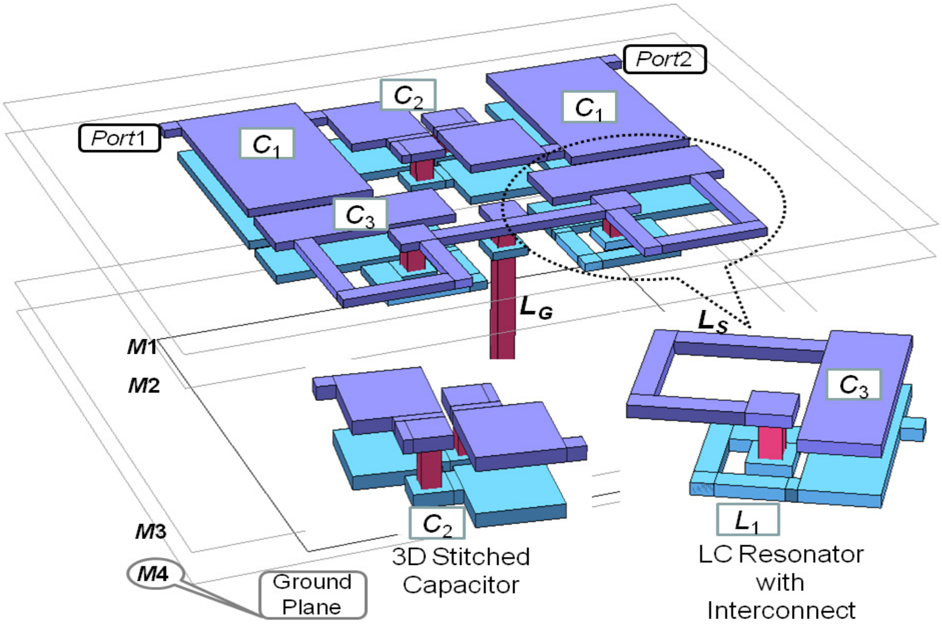

(b)

Figure 48. Physical layout of type1 (a) 2 GHz BPF and (b) 5 GHz BPF.

The measurement was carried out using short-open-load-thru (SOLT) calibration using Agilent PNA 8363B and Cascade GSG-500 air coplanar probes. The measurement equipment is shown in Figure 49, and one of the 5 GHz BPFs measurements showing less than 1 dB insertion loss is shown in Figure 50.

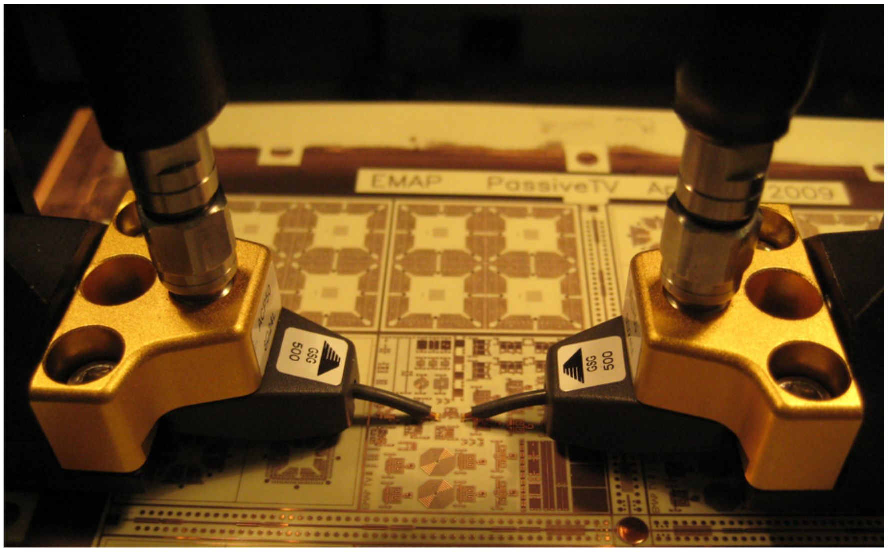

Figure 49. Measurement equipment with GSG probes.

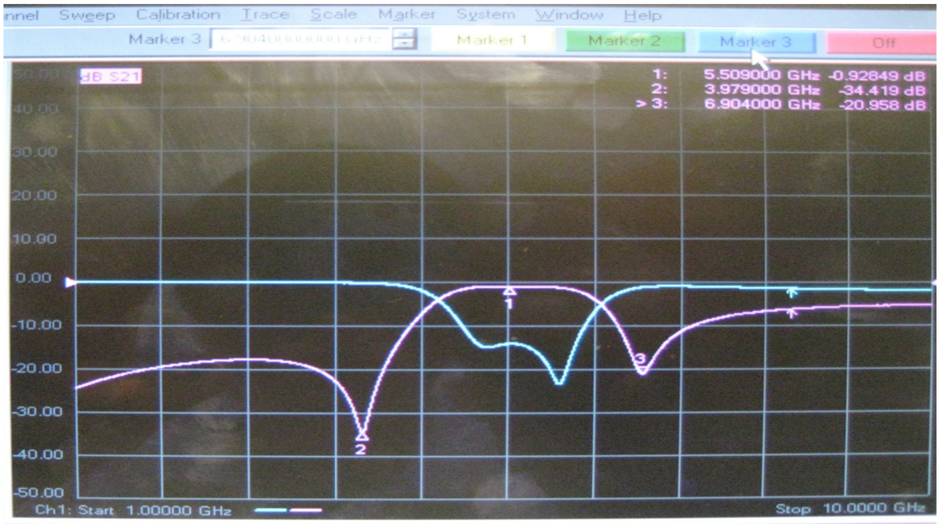

```
  1:   5.509000 GHz  -0.92849 dB
  2:   3.979000 GHz   -34.419 dB
> 3:   6.904000 GHz   -20.958 dB
```

Figure 50. Measured frequency response from VNA.

Based on the measurement, the measured RXP BPFs (type1) responses have excellent correlations with the simulation. Both measured and simulated frequency responses are shown in Figure 51.

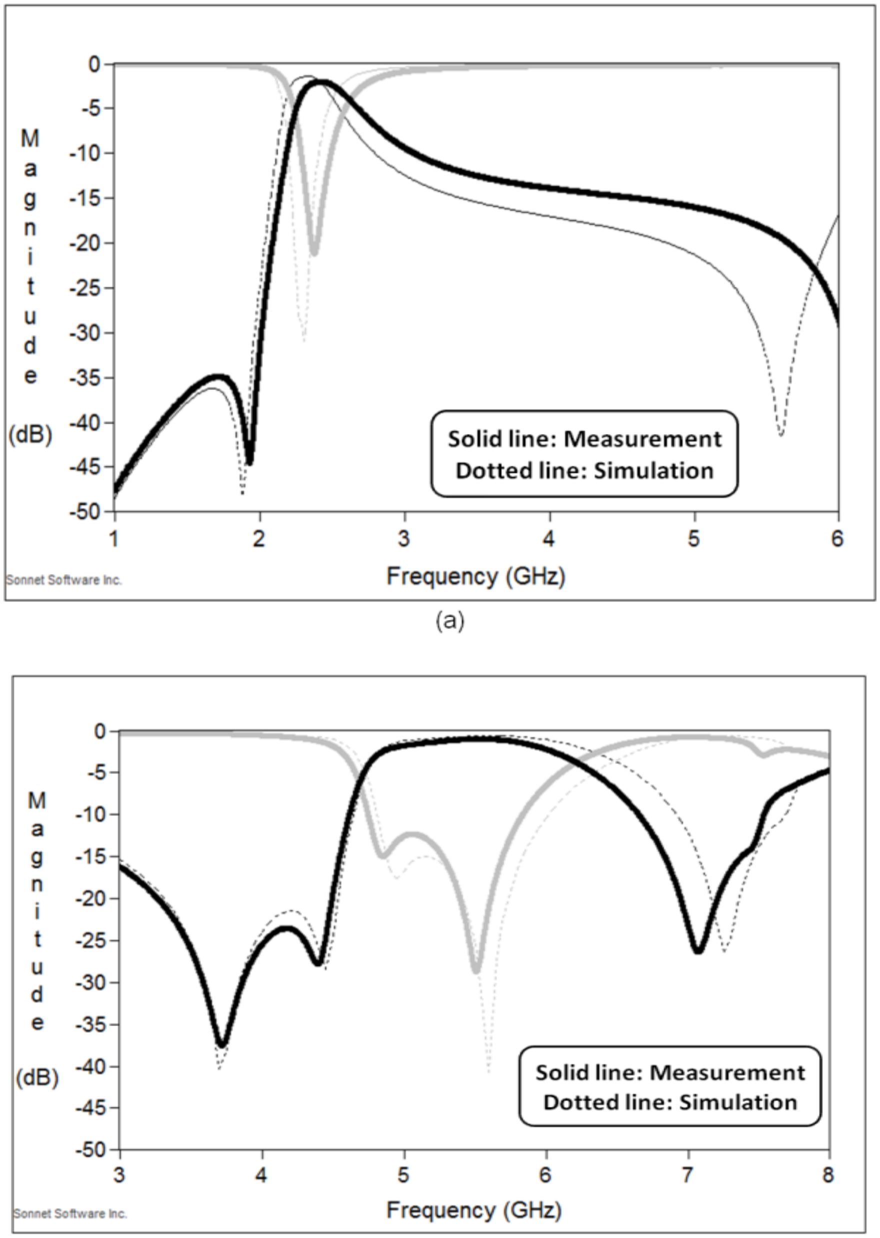

Figure 51. Measured results for type1 (a) 2 GHz and (b) 5 GHz BPFs.

The measured 2 GHz BPF exhibited a center frequency of 2.4 GHz and a 3 dB bandwidth of 250 MHz. The return loss was lower than 20 dB, and the insertion loss was 2 dB at the center frequency. Furthermore, 30 dB attenuation beyond 300 MHz out of the passband was achieved. The measured 5 GHz BPF exhibited a center frequency of 5.5 GHz with 1.3 GHz bandwidth. The return loss was lower than 24 dB, and the insertion loss was 0.97 dB at the center frequency. For the rejection, 27 dB attenuation at 400 MHz out of the passband was achieved. Transmission zeros occurred at 4.4 GHz and 7 GHz, which are ideal for rejecting unwanted harmonic signals.

3.4.2 Miniaturization of High-Rejection Second-Order WLAN Bandpass Filters

After verifying the filter performances and the proposed topology, two more designs (type2) were constructed for size reduction. For the 2 GHz design, mutual coupling in the resonator inductors (*L1)* was applied by placing inductors adjacently so that the current going though the inductor travels to the same direction. For the 5 GHz design, each element value was recalculated to target smaller capacitances. The physical layouts of the optimized designs are shown in Figure 52.

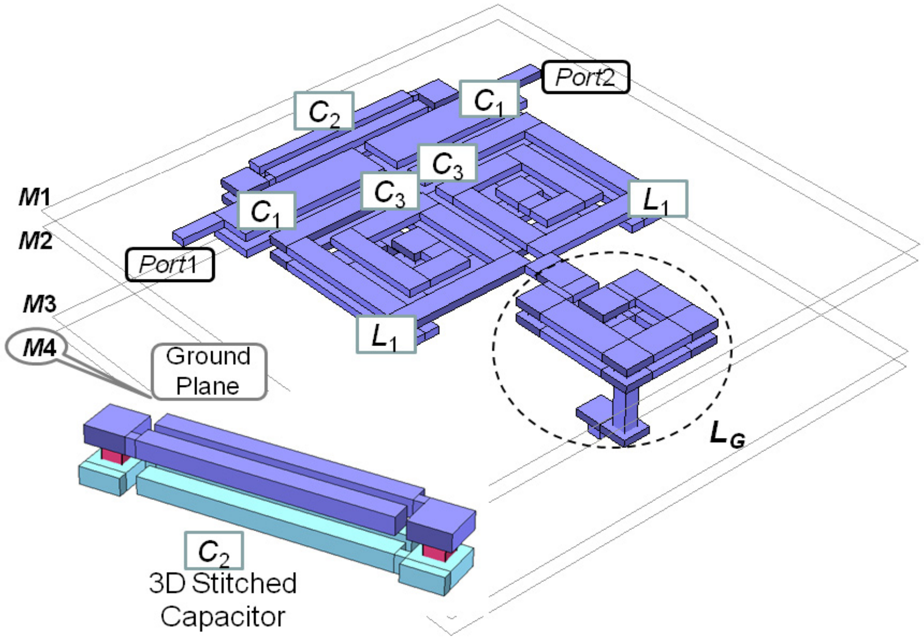

(a)

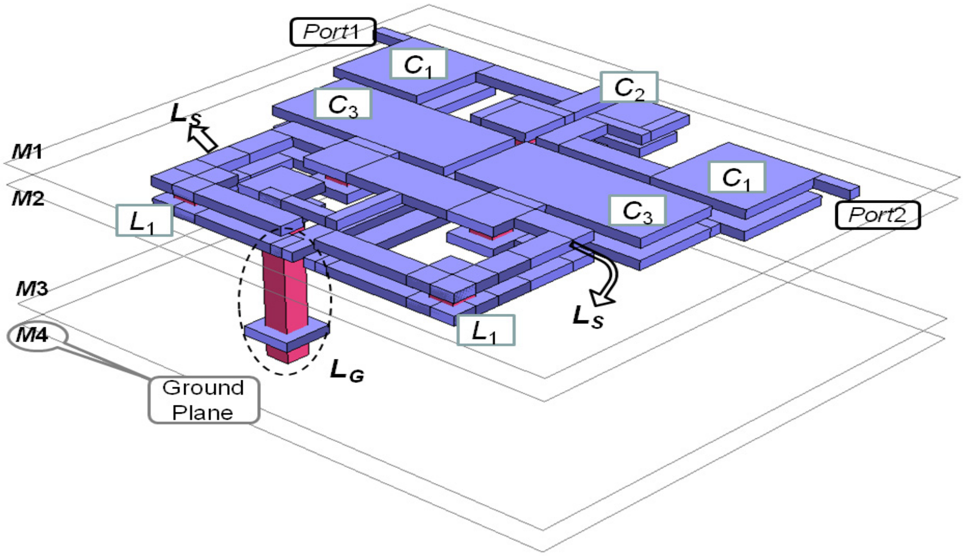

(b)

Figure 52. Physical layout of type2 (a) 2 GHz and (b) 5 GHz BPFs.

The size of miniaturized 2 GHz filter was 2.2 mm × 3.0 mm × 0.191 mm (24 % area reduction compared to the first design), and the 5 GHz filter occupied 1.85 mm × 1.6 mm × 0.191 mm (52 % area reduction compared to the first design), which showed the high integration capability of the ultra-thin RXP substrate. The measured results for the miniaturized designs of 2 and 5 GHz BPFs are shown in Figure 53. The measured miniaturized 2 GHz filter was centered at 2.38 GHz and had a 3 dB bandwidth of 200 MHz. The return loss was lower than 18 dB, and the insertion loss was 2.2 dB at the center frequency. Furthermore, **low-band attenuation of 30 dB beyond 250 MHz from the passband** was achieved. For 5 GHz design, the measurement exhibited a center frequency of 5.6 GHz with 1.5 GHz bandwidth. The return loss was lower than 14 dB, and the insertion loss was 0.92 dB at the center frequency, which shows high performance integration of RXP technology for filter.

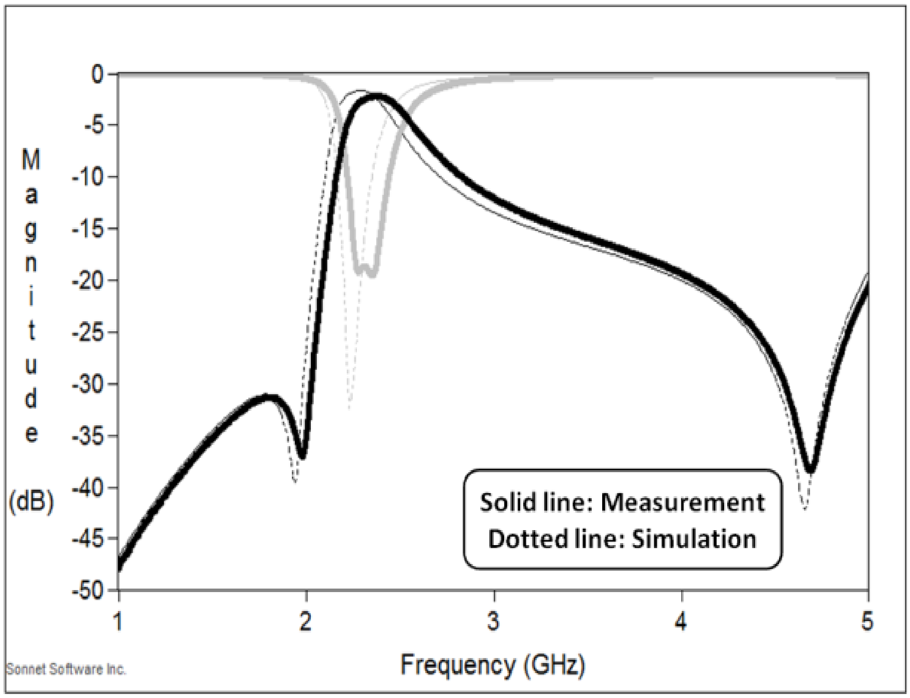

(a)

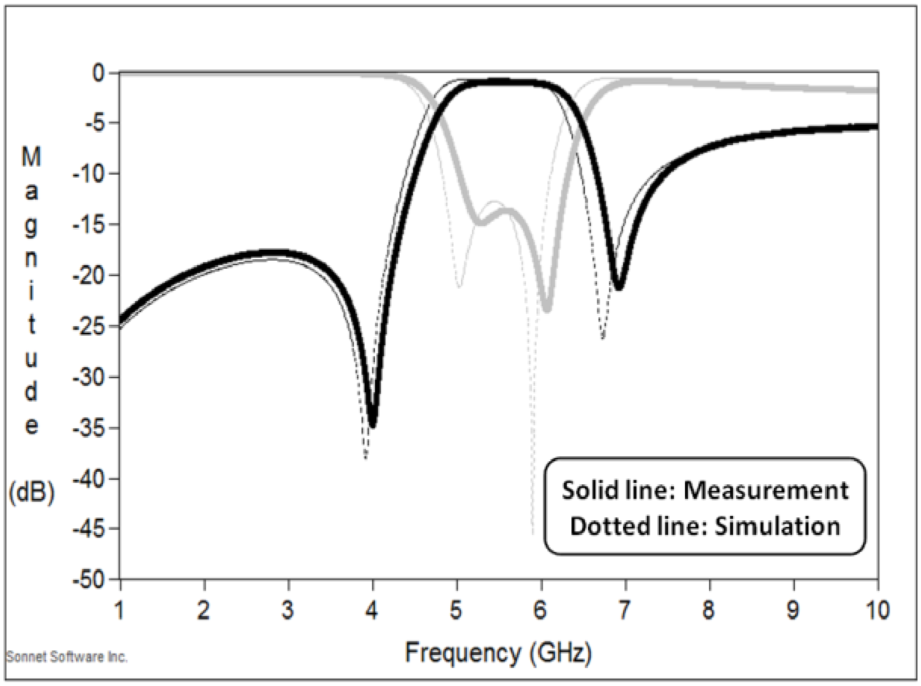

(b)

Figure 53. Measured results for type2 (a) 2 GHz and (b) 5 GHz BPFs.

3.4.3 Design of High-Order WLAN Bandpass Filters

Although the second-order topology provides high-rejection performance, commercially challenging 5 GHz filter specification requires more stringent rejection requirement. Therefore, a third-order BPF topology has been developed and synthesized for an enhanced stopband characteristic as shown in Figure 54.

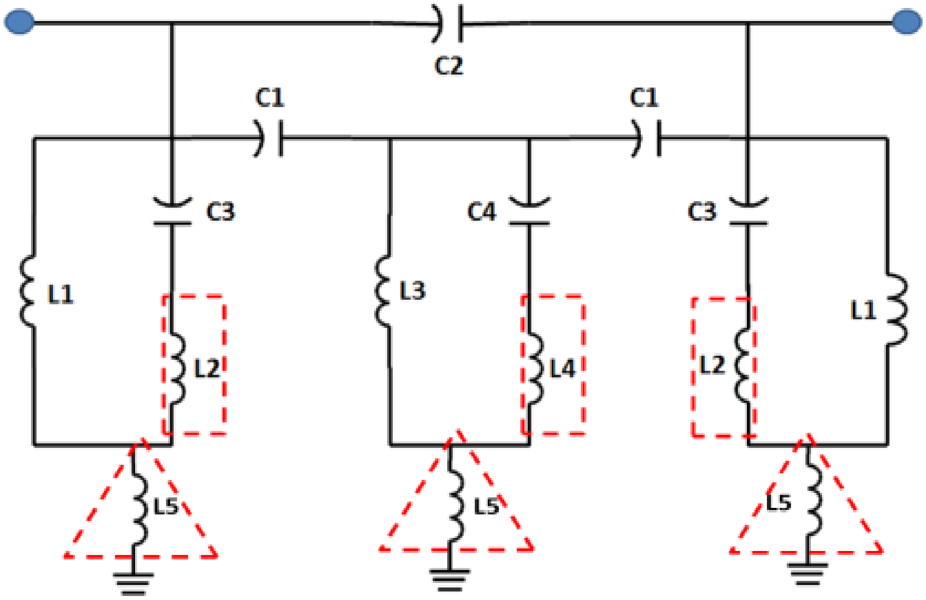

Figure 54. Proposed third-order BPF schematic.

The circuit topology without additional elements *L*2, *L*4, *L*5 (the dotted square and triangle areas) has been known for producing two transmission zeros [20]; it uses a second-order coupled resonator BPF in parallel with a feedback capacitor (*C2*) and magnetic coupling between inductors, which introduce finite transmission zeros to the low and high stopband. Instead of having the magnetic coupling between inductors, the additional elements can introduce multiple transmission zeros as shown in Figure 55, which shows the effect from these additional elements.

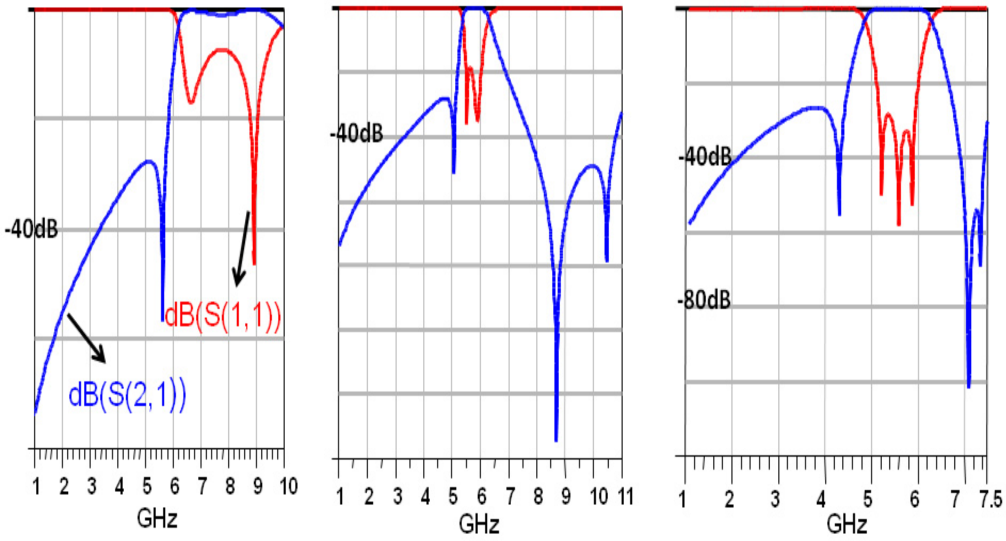

(a) (b) (c)

Figure 55. BPF responses. (a) Without additional elements. (b) With L2 and L4. (c) With L2, L4, and L5.

Figure 55 (a) shows the response without any additional elements and magnetic coupling. It is clear that the bandwidth is very wide without rejection at the upper stopband. After series inductors (*L2* and *L4*) are included, Figure 55 (b) shows two transmission zeros for the high stopband. As shown in Figure 55 (c), the rejection response from Figure 55 (b) is dramatically improved by adding the inductor *L5*. It is important to note that the lumped-elements values in Figure 54 have not been changed, but only components *L2*, *L4*, and *L5* are added to improve the filter response.

The series inductors are related to the high stopband transmission zeros, which can be calculated using

$$L2 = \frac{1}{(2\pi f_{tz1})^2 \cdot C3} \tag{29}$$

$$L4 = \frac{1}{(2\pi f_{tz2})^2} \cdot \frac{C1 + C4}{C1 \cdot C4} - L3 \tag{30}$$

where f_{tz1} is the first high stopband transmission zero and f_{tz2} is the second transmission zero frequency. After including series inductors, the ground inductor can be obtained by

$$L5 = \left| \frac{L1 \cdot [1 - (2\pi f_{tz3})^2 \cdot L2 \cdot C3]}{1 - (2\pi f_{tz3})^2 C3 \cdot (L1 + L2)} \right| \tag{31}$$

where f_{tz3} is a desired high stopband rejection frequency. In addition, the location behavior of additional transmission zeros can be easily observed by tuning *L2*, *L4*, and *L5* in a commercial circuit simulator [75].

The calculated circuit element values in Figure 54 are *L1*=0.31 nH, *L2*=0.34 nH, *L3*=0.34 nH, *L4*=0.55 nH, *L5*=0.37 nH, *C1*=0.41 pF, *C2*=0.21 pF, *C3*=0.99 pF, *C4*=0.76 pF. After obtaining all of the lumped-element values, each element is replaced by a corresponding layout. The overall size of the filter is 2.6 x 2.1 x 0.191 mm^3. Figure 56 shows a physical layout of the organic BPF embedded in a four-metal layer RXP substrate and Figure 57 shows the fabricated filter.

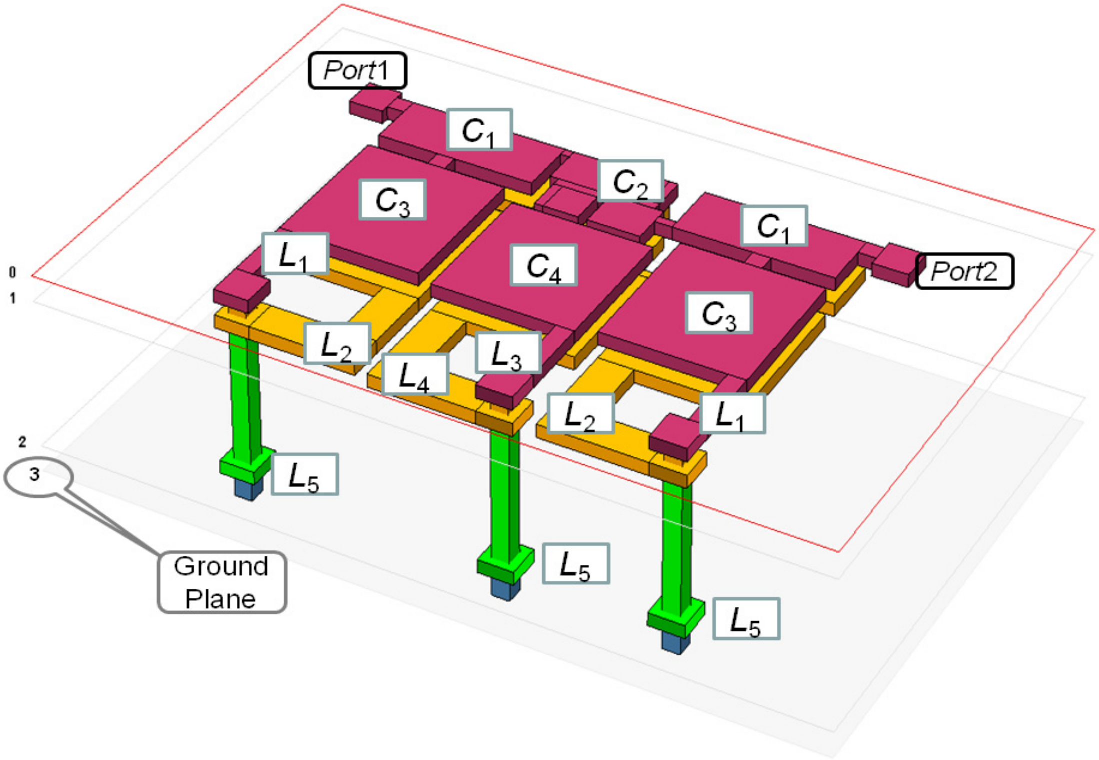

Figure 56. Layout of type3 5 GHz filter.

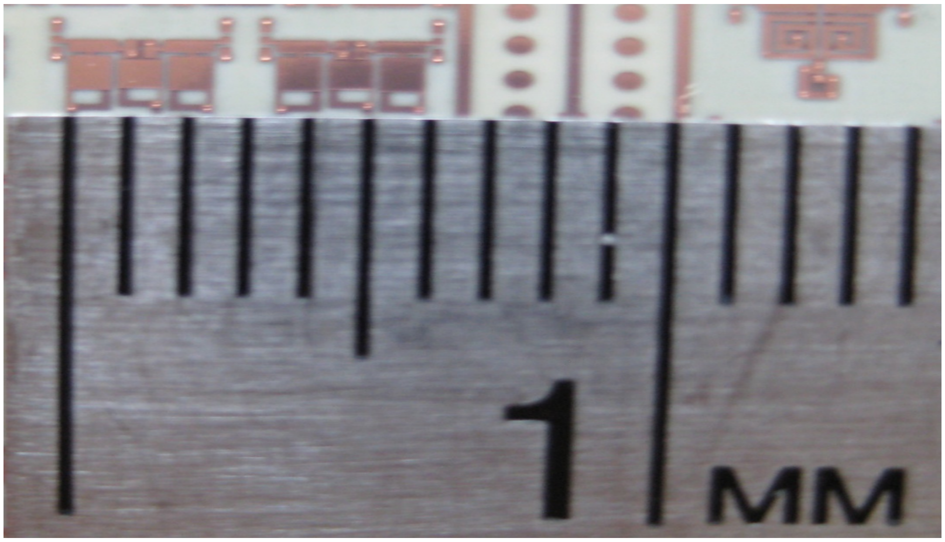

Figure 57. Fabricated 5 GHz 3rd order BPF.

As shown in Figure 58, the measured third-order 5 GHz filter exhibited a center frequency of 5.5 GHz with 3 dB bandwidth of 1.7 GHz. The return loss was 20 dB, and the insertion loss was 1.09 dB at the center frequency. Furthermore, **better than 31 dB attenuation at 4.4 GHz and 7.2 GHz** were achieved, which is ideal for rejecting unwanted signals and satisfying the challenging rejection specifications.

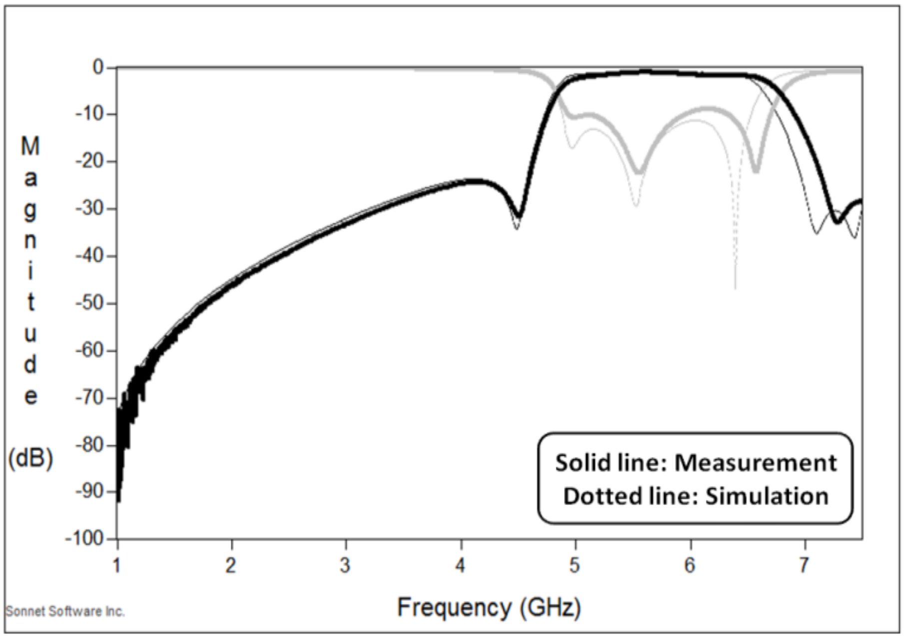

Figure 58. Measured result for type3 5 GHz BPF.

For 2 GHz, shunt inductor was added at the input port (before *C1*) to produce additional transmission zeros as shown in Figure 59. It is important to note that the high rejection filter is based on the proposed topology and method as well.

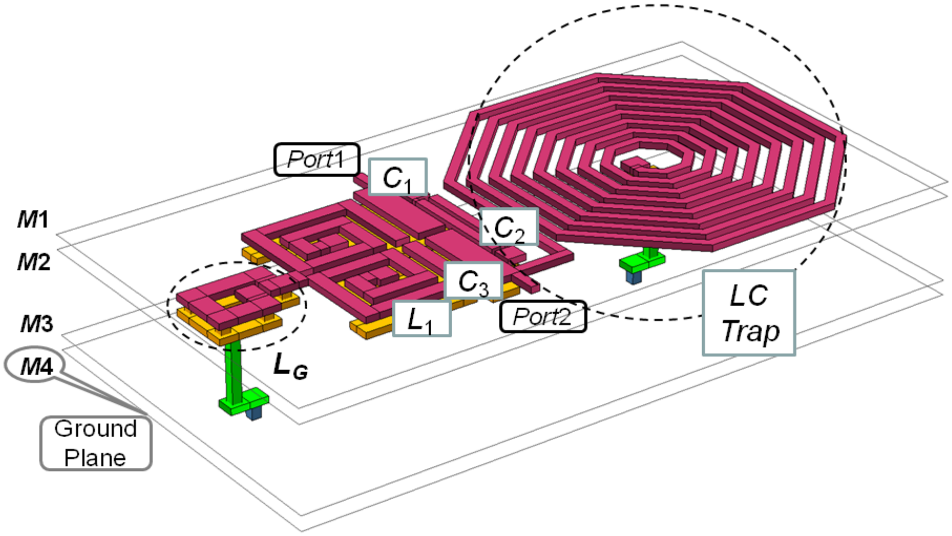

Figure 59. Layout of type3 2 GHz BPF.

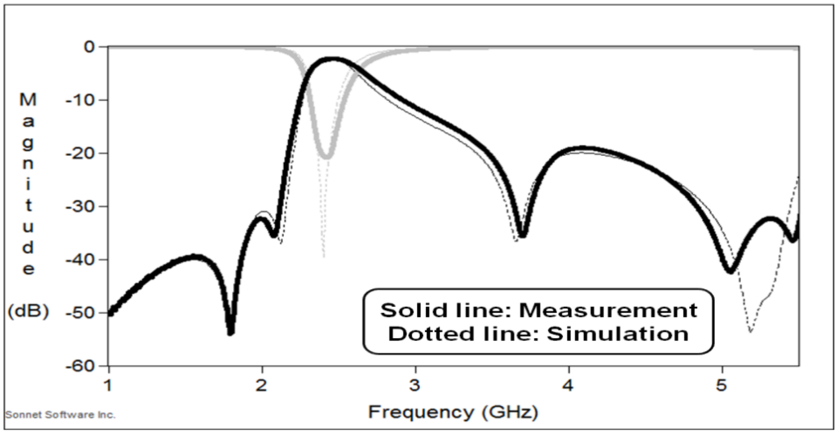

Figure 60. Measured result for type3 2 GHz BPF.

Figure 60 shows the measured results for the high rejection 2 GHz filters. Based on the measurement, the fabricated 2 GHz filter was centered at 2.46 GHz and had a 3 dB bandwidth of 200 MHz. The return loss was lower than 20 dB, and the insertion loss was 2.3 dB at the center frequency. Furthermore, 30 dB attenuation at 2.12 GHz and 29 dB attenuation at 4.8 GHz were achieved.

3.5 Summary

This chapter presented the world's smallest ultra-thin high-rejection WLAN RXP filters for the first time. High-rejection bandpass filter topologies for narrow and wide bands were developed by modifying resonator tank circuits and adding a grounding inductor. Multiple transmission zeros distributed lower and upper stopband relative to the center frequency were observed without increasing the size of the layout significantly because interconnects such as connections from capacitor to inductor were used as design parameters. Along with design equations for individual circuit elements, a graphical design methodology was also developed to predict the filter performance using the Z-parameters. The proposed bandpass filter schematic for enhanced stopband characteristics has been verified through design and measurement. RXP filters had low insertion loss while maintaining high rejection at both low and high stopbands. To summarize the results, Table 6 shows the performance summary based on the measurement data and comparison with comparable LTCC WLAN filter. The smallest volume of the designed 2 GHz filter was 2.2 mm × 3 mm × 0.191 mm (1.26 mm^3) and, 5 GHz filter was 1.85 mm × 1.6 mm × 0.191 mm (0.57 mm^3), which are more than nine times smaller than LTCC filters: 5.4 mm × 3.9 mm × 0.765 mm (16.11 mm^3) for 2 GHz [22], 3.3 mm × 2 mm × 0.8 mm (5.28 mm^3) for 5 GHz [18].

Table 6. Performance summary of measured RXP filters.

WLAN rejection slope (dB/100 MHz)
- 2.45 GHz: Lowband: 9.56
- 5.5 GHz: Lowband: 4.4 Highband:1.7

		F_c (GHz)	I.L. (dB)	BW	Rejection (dB/100 MHz)	Volume (mm^3)
RXP	Type1	2.4	2	250 MHz	9.78	3.6 x 2.4 x 0.191 (1.65)
	Type2	2.38	2.2	200 MHz	10.8	**2.2 x 3.0 x 0.191 (1.26)**
	Type3	2.46	2.3	200 MHz	11.25	3.6 x 6.9 x 0.191 (4.74)
	Type1	5.5	0.97	1.3 GHz	6.32, 2.93	2.55 x 2.45 x 0.191 (1.19)
	Type2	5.6	0.92	1.5 GHz	3.43, 3.38	1.85 x 1.6 x 0.191 (0.57)
	Type3	5.5	1.1	1.7 GHz	6.775, 4.85	**2.6 x 2.1 x 0.191 (1.04)**
LTCC [14]		2.45	1.8	430 MHz	10.8	5.89 x 3.25 x 1.08 (20.67)
LTCC [17]		5.5	1.1	1.2 GHz	1.67, 2.5	3.3 x 2.0 x 0.8 (5.28)

The best way to verify characterization results from Chapter 2 is to build a specific device such as a microwave filter. Six different bandpass filters were designed, fabricated, and measured in the four-metal layer RXP substrate using extracted material properties. Total of 96 RXP bandpass filters were measured and 93 filters worked for the first time of RXP fabrication. Good correlation between measurements and simulations was observed showing the accuracy of extracted material properties and the proposed design methodology.

The layout design of the lumped-element can be a difficult task in the microwave frequency. Hence, 3D stitched capacitor was proposed to make more symmetrical layout design than 3D conventional parallel-plate capacitor. Unbalanced shunt parasitics from the 3D conventional capacitor became balanced shunt parasitics in the 3D stitched capacitor, which was verified through the measurement. Based on the results, RXP filter can be an ideal solution for miniaturization in RF applications since they have high integration capability as well as high performance.

CHAPTER 4

DUAL-BAND BANDPASS FILTERS AND DUPLEXER IN RXP SUBSTRATE

Bandpass filter, which was discussed in the previous chapter, is an essential component in RF modules since there is always a need to filter out unwanted signals that come from non-linearity of the active devices. Moreover, the size of RF module depends largely on the size of passive devices, which are mainly filters. Therefore, miniaturizing and replacing or removing filters become critically important.

As described in the previous chapter, 5 GHz and 2.4 GHz signaling frequencies each have their advantages. In terms of its range, 2.4 GHz networks cover a substantially larger range than 5 GHz wireless networks since the higher frequency signal will have a shorter range. In particular, the 5 GHz networks do not penetrate solid objects nearly as well as do 2.4 GHz signals [76]. From the interference perspective, it is more likely the 2.4 GHz will pick up more interference from other appliances than the 5 GHz application because there are more consumer products using 2.4 GHz than 5 GHz frequency. Therefore, dual-band applications are required that combines the best of both frequency types into products, which become a very attractive solution for the next generation wireless applications.

This chapter proposes a solution to eliminate one or more filter components in the dual-band RF block diagram by supporting dual-band bandpass filters and duplexers. By making a single bandpass filter to operate as two bandpass filters, the RF module can be simplified and switch elements or matching circuits can be omitted. The proposed dual-band bandpass filter is based on lumped-element because the lumped-element has much better miniaturization capacity than the distributed-element, which also has a fundamental limitation in bandwidth and operating frequency.

As a rapidly increasing segment of communications industry, wireless communications have been a major aspect of everyday life. The consumer demand for accessing compact devices has been pushing RF engineers for low-cost, effective integration and miniaturization of RF components. There has been a considerable amount of effort in the past years to find and implement novel packaging technologies to achieve this goal. System-on-package (SoP) technology has been shown to provide low-cost highly-integrated modules for wireless applications. The recently developed SoP is shown in Figure 61, which is based on the chip-last embedded technology [43]. To successfully embed IC and connect IC to passive components, a duplexer based on high-rejection bandpass filters from Chapter 3 is proposed in this chapter.

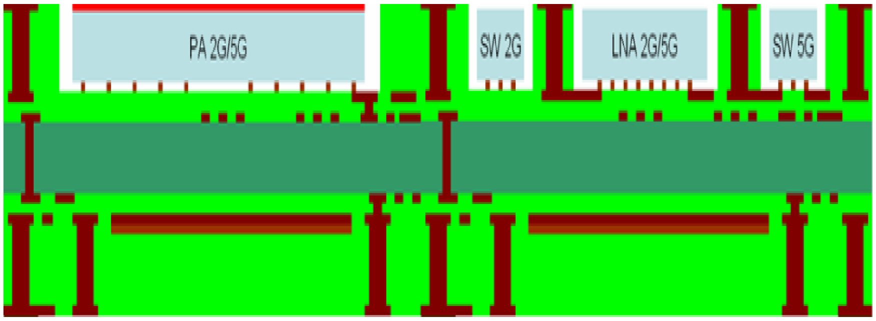

Figure 61. Multi-chip embedded SoP module.

This chapter focuses on the design of dual-band bandpass filters and duplexers using lumped-element components. The prior work on dual-band bandpass filter and drawbacks of a transmission line based method are explained in Section 4.1. A proposed dual-band topology along with design equations and measured results are presented in Section 4.2. Section 4.3 shows a miniaturized RXP duplexer with re-designed high-rejection bandpass filters from Chapter 3. Finally, the chapter is summarized in Section 4.4.

4.1 Drawbacks of Dual-Band Filters using Transmission Line Based Method

Similar to bandpass filter theory, there are two different ways to construct a dual-band behavior structure; namely, transmission line method and lumped-element method. The advantage of the transmission line method is its planar structure that makes the design easier than lumped-element, but there are several limitations and disadvantages compared to the lumped-element method. The transmission line method can be further classified into three categories such as stub-loaded, stepped impedance, and patch.

For the stub-loaded type of dual-band bandpass filters, numerous published works have been reported. A dual-band filter consisting of a bandstop and wide-band bandpass filter using a cascaded connection is reported in [77]. A coupled-serial-shunted line was used for bandstop filter and the wide-band bandpass filter was implemented by serial-shunted line. Since this solution essentially combines two different filters, the number of components, hence, size of the structure is increased. In [78], the stub-loaded open-loop resonators loaded by shunt open stubs are proposed to design dual-band bandpass filters. However, it requires external coupling structure and does not provide a controllability of the bandwidths. E-type resonator that is a short-circuited stub loaded hairpin was presented in [79]. Although the size of filter was smaller than other the distributed-element designs (7 mm x 5.1 mm), the bandwidth of the design was not enough to cover the minimum required bandwidth for WLAN applications.

In addition to the large size drawback in the stub-loaded type filters, the transmission line method has fundamental limitations. It was shown that both series and shunt stubs have a center frequency ratio (f_2/f_1) limitation of 3 [80]. In fact, the impedances of the open stubs are close to the termination impedance when the center frequency ratio is around 2. In order words, the filter needs inverters when the center frequency ratio exceeds 2, which requires additional quarter-wavelength transmission lines. Moreover, the center frequency ratio has a relationship with the maximum bandwidth ratio as shown in Figure 62.

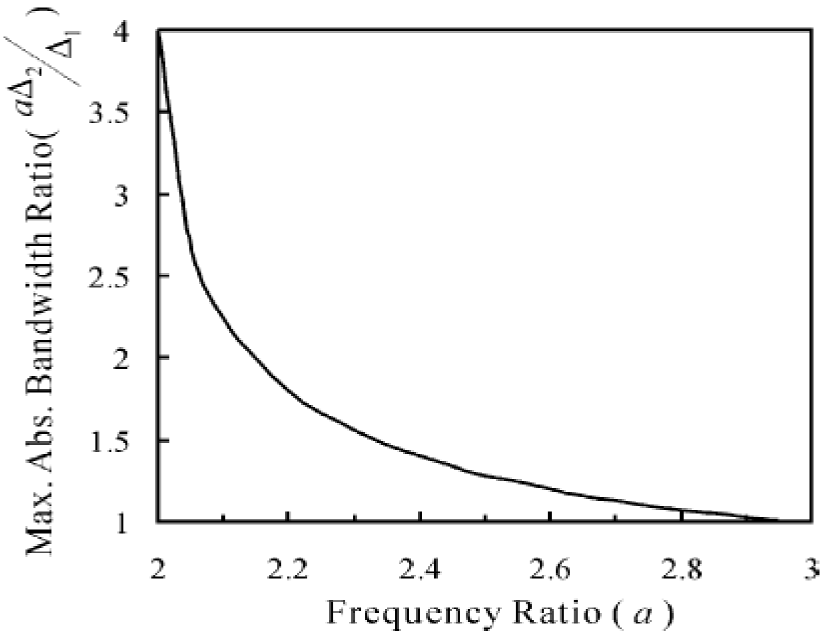

Figure 62. Maximum bandwidth ratio vs center frequency ratio [80].

As shown in Figure 62, the maximum bandwidth ratio is inversely proportional to the center frequency ratio. It is important to note that the maximum bandwidth ratio is only 4 when the center frequency ratio is at level 2. Since the bandwidth requirement in WLAN specification requires at least 5 for the maximum bandwidth ratio, the application of the stub-loaded type is very limited.

Because of the fabrication and design simplicity, the stepped impedance method was a popular solution for the dual-band bandpass filter designs. The modified half-wavelength stepped-impedance resonator was presented in [81]. Although the proposed design does not require external impedance-matching feeds, the overall size was more than 10 mm by 10 mm and measured insertion loss was not good. In [82], a ring dual-mode stepped impedance resonator was used, but the measured bandwidth was only 6 % while at least 20 % is required for 5 GHz. Quarter-wavelength stepped impedance resonator was proposed by using coupled short and open stepped impedance resonator [83]. Despite of its quarter-wave length resonator, the size of the layout was not miniaturized because the open stepped impedance resonator behaved as a half-wave resonator. Another type of ring resonator was used by a cascade of several microwave C-sections [84], which achieved 27.3 % less area than traditional ring resonator dual-band filters. Nevertheless, the proposed filter cannot be used in practical applications since the coupled section becomes an uncoupled section when the center frequency ratio is 2.

The last type of transmission line based method uses the square patch. The authors in [85] proposed a pair of slits embedded in the square patch in order to generate three transmission zeros for dual-band characteristics. Although the proposed design achieved 10 % bandwidth at the low passband, the center frequency ratio was less than 1.4.

4.2 Miniaturized Lumped-Element Dual-Band Bandpass Filter

The previous section showed previous work on dual-band bandpass filter design based on the transmission line based method and discussed its major drawbacks. The unguided wavelength at 5 GHz is 60 mm, which corresponds to 15 mm for the minimum quarter-wave length transmission line. Since the emerging wireless application keeps pushing the miniaturization limit, the transmission line based method is not suitable for the next generation dual-band bandpass filter design. In addition, the transmission line based method provides very limited bandwidth as well as center frequency ratio, as discussed earlier.

Therefore, this section describes the lumped-element based dual-band bandpass filter, which is compact and overcomes limitations on the bandwidth and the center frequency ratio as compared to using distributed element. Typically, lumped-element based method requires much more effort to make the layout since there are unpredicted interactions between inductors and capacitor, which can be realized in numerous ways.

The simplest way to realize the dual-band bandpass filter using lumped-element is to combine two separate bandpass filters. By taking the size advantage and multilayered capability from lumped-element method, authors in [86] presented a compact dual-band filter. However, it used four resonators that increase the circuit complexity and layout difficulty, which resulted in poor isolation level and correlation with the measurement.

To make the realization of the lumped-element layout easy and improve the dual-band performance, a new dual-band circuit topology is proposed as shown in Figure 63.

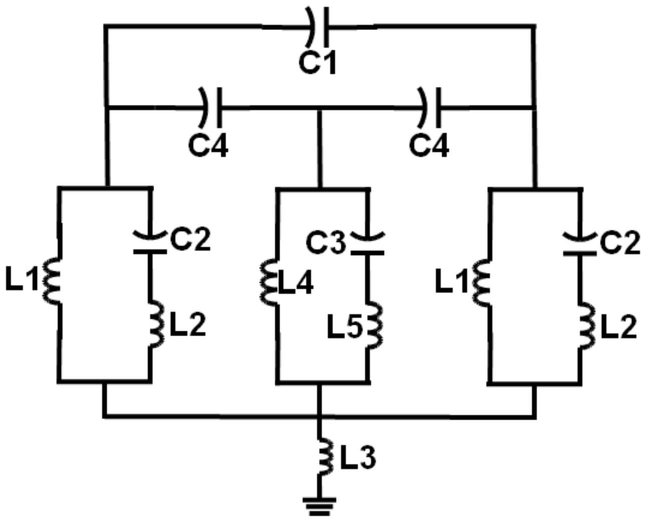

Figure 63. Proposed dual-band topology.

This proposed topology is similar to the high-rejection topology from Chapter 3 where the topology has been used for the third-order 5 GHz bandpass filter except the location of the grounding inductor (L3). The main idea of this proposed dual-band topology is to reorganize the location of the transmission zeros in order to obtain two separate pass-bands.

It has been shown that multiple transmission zeros can be generated using a combination of the series inductors (L2, L5), feedback capacitor (C1), and grounding inductors (L3) [39]. Since multiple transmission zeros are generated from individual inductors and capacitor, the location of transmission zeros can be predicted and controlled. Among the three modified resonators, the middle one can be designed to resonate at the desired second passband frequency. If the location of the transmission is controlled to be located at the isolation frequency between the two passbands, good dual-band filter performance can be obtained.

The design procedure starts with calculating each circuit element value. First, the low-passband components are calculated by ignoring the center resonator and the matching capacitors (C4). The corresponding schematic and its frequency response are shown in Figure 64.

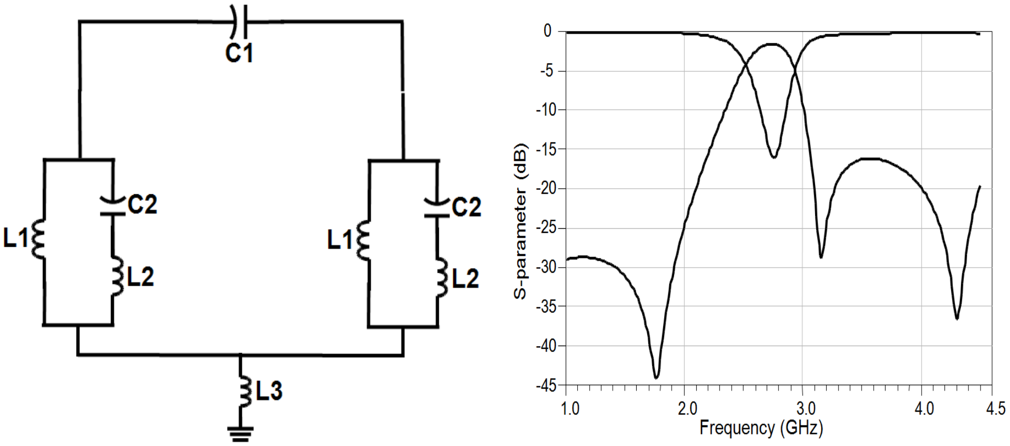

(a) (b)

Figure 64. (a) low-passband schematic and (b) its frequency response for low-passband.

The resonator capacitor (C2) can be calculated using the relationship between the input impedance near resonance of a parallel LC circuit and the transfer impedance of the resonator [62]. Therefore, C2 is obtained using

$$C2 = \frac{1}{2Z_0(f_2 + f_1)} \tag{32}$$

where f_2 and f_1 are high and low passbands, respectively. The series inductors (L2) are related to the transmission zero that is generated when C2 and L2 resonate, which can be calculated as

$$L2 = \frac{1}{(2\pi f_{1Z})^2 \cdot C2} \tag{33}$$

where f_{1z} is the frequency of the low-band transmission zero. The equivalent circuit in Figure 64 is a π-network before adding the grounding inductor (L3). The π-network creates the passband response when the impedance of the C1 and the modified resonator tanks become equal. In other words, the impedance of the modified resonator and C1 should be equal at the center frequency of the low passband. Therefore, the rest of circuit elements can be obtained using

$$\frac{2s^2 \cdot L1 \cdot (1 + s^2 \cdot C2 \cdot L2)}{1 + s^2 \cdot C2 \cdot (L1 + L2)} = \frac{1}{C1} \tag{34}$$

where s = $j2\pi f_{1c}$. Finally, the additional transmission zeros can be added to create isolation between low and high passband by including the grounding inductor (L3) using

$$L3 = \frac{C1}{Y^2 + 2Y \cdot s \cdot C1} \qquad \text{where } Y = \frac{1 + s^2 \cdot C2 \cdot (L1 + L2)}{s \cdot L1 \cdot (1 + s \cdot C2 \cdot L2)} \qquad (35).$$

The calculated component values are C1=0.99 pF, C2=1.15 pF, L1=0.87 nH, L2=1.77 nH, and L3=0.18 nH.

After obtaining the low-passband component values, the high-passband element can be added to complete the dual-band bandpass filter response. Since the low-passband provides two transmission zeros at the middle stopband, the high-passband can be constructed by a single modified resonator, which can generate a high-stopband transmission zero. The single modified resonator schematic and its frequency response are shown in Figure 65.

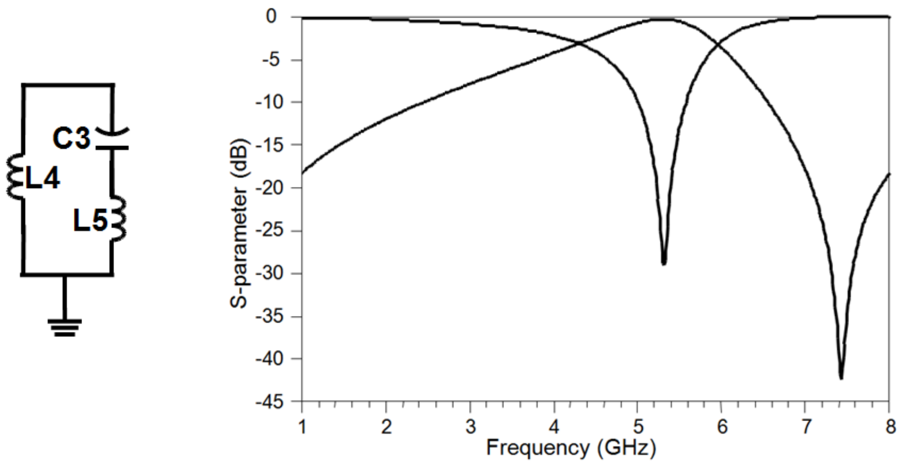

Figure 65. Single modified resonator and its frequency response for high passband.

Using the relationship between the input impedance near resonance of a parallel LC circuit and the transfer impedance of the resonator, C3 can be calculated as

$$C3 = \frac{1}{4Z_0 \cdot f_{2c}} \tag{36}$$

where f_{2c} is the center of high-passband. The series inductor (L5) will create the high-stopband transmission zero and it can be obtained using

$$L5 = \frac{1}{(2\pi f_{2Z})^2 \cdot C3} \qquad (37).$$

The single modified resonator creates a passband when the impedance of the inductors and capacitor become identical. Therefore, L4 can be found by

$$L4 = \frac{1}{(2\pi f_{2c})^2 \cdot C3} - L5 \qquad (38).$$

Matching capacitors (C4) should transform the shunt LC resonator into the series LC resonator in order to combine the low-passband and high-passband elements. Therefore, C4 can be found by using the admittance inverter equation as [87]

$$\Delta = \frac{f_{1S} - f_{1E}}{\sqrt{f_{1S} \cdot f_{1E}} = f_0} \tag{39a}$$

$$g_1 = \frac{2}{\sinh\left(\frac{\ln[\coth(\frac{ripple}{17.37})]}{2n}\right)} \sin\left(\frac{\pi}{2n}\right) \tag{40b}$$

$$J_{01} = \frac{1}{Z_0}\sqrt{\frac{\pi \cdot \Delta}{4 \cdot g_1}} \tag{41c}$$

$$C_4 = \frac{J_{01}}{2\pi f_0 \sqrt{1 - (Z_0 \cdot J_{01})^2}} \tag{42d}$$

where f_{1s} f_{1e} denotes the edges of the low-passband, ripple is in unit of dB, and n is the order of the low-passband filter. The final calculated component values are C3=0.91 pF, L5=0.504 pF, L4=0.48 nH, and C4=0.42 pF.

After obtaining all of lumped-element values, each element was replaced by the corresponding layout. The physical layout was realized using RXP technology with 6 metal layer stack-up as shown in Figure 66, and Table 7 summarizes the design rule and metallization thickness.

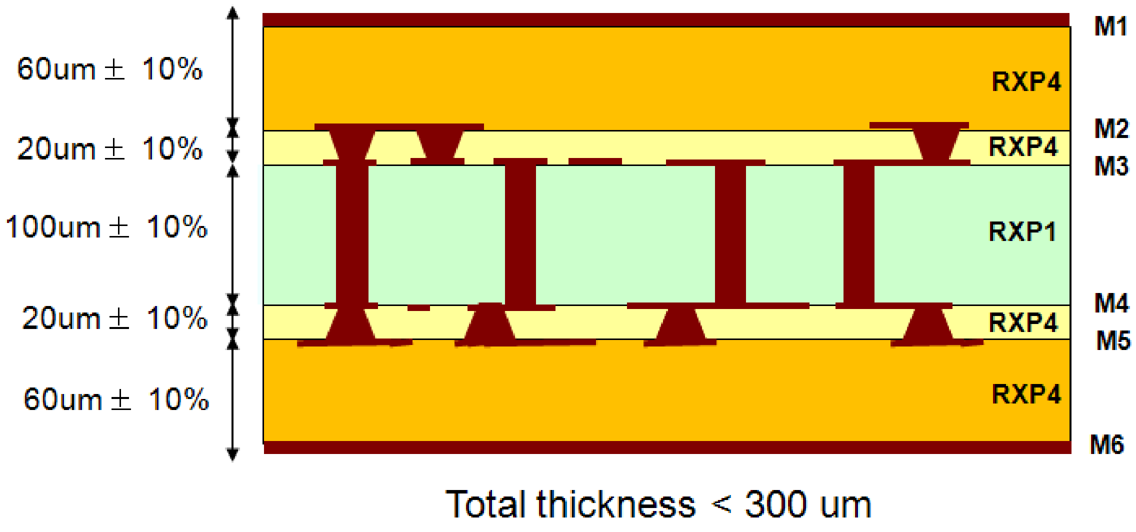

Figure 66. Six-metal layer RXP stack-up.

Table 7. Design rule for six-metal layer RXP substrate.

			Designed values
Metallization	M1,M2 M5,M6	Line Width / Spacing	50 um / 50 um
		Thickness	15 um ± 15%
	M3,M4	Line Width / Spacing	50 um / 50 um
		Thickness	10 um ± 15%
Via	Pad Diameter		200 um
	Via Diameter		100 um

The final layout and dimensions of the lumped-element components are shown in Figure 67 and Figure 68, respectively. The inductor and capacitor are only realized in metal layer 2, 3, and 4 (M2-M4) while M6 is used as the ground plane. The thickness from M1 to M2 is 60 µm, M2 to M3 is 20 µm, M3 to M4 is 100 µm, M4 to M5 is 20 µm, and M5 to M6 is 60 µm. Hence, the total thickness is only 260 µm. The minimum spacing is 50 µm, via diameter is 100 µm, and via pad is 200 µm.

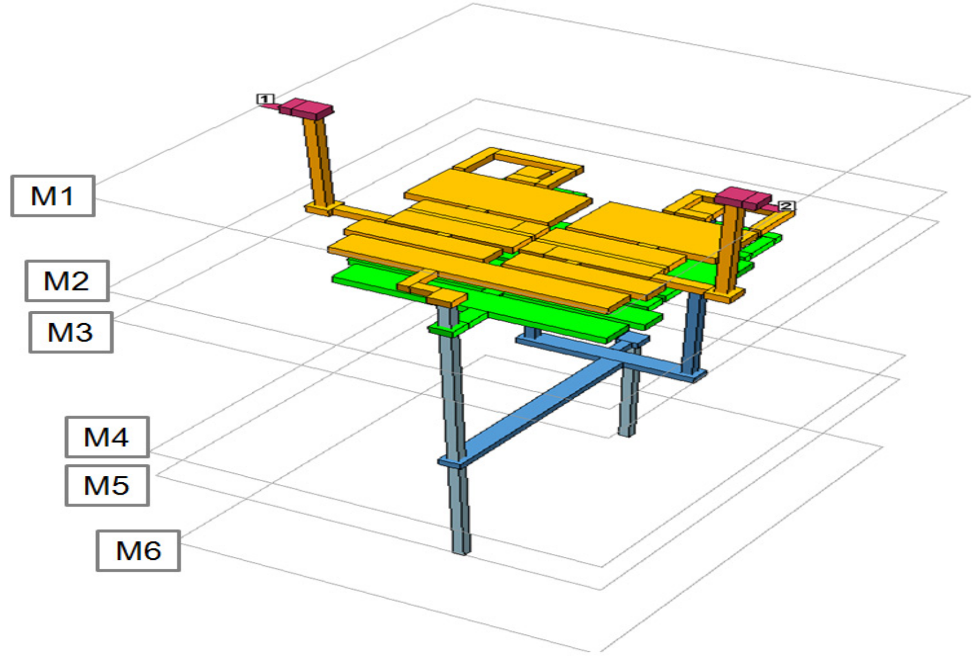

Figure 67. Physical layout of dual-band bandpass filter.

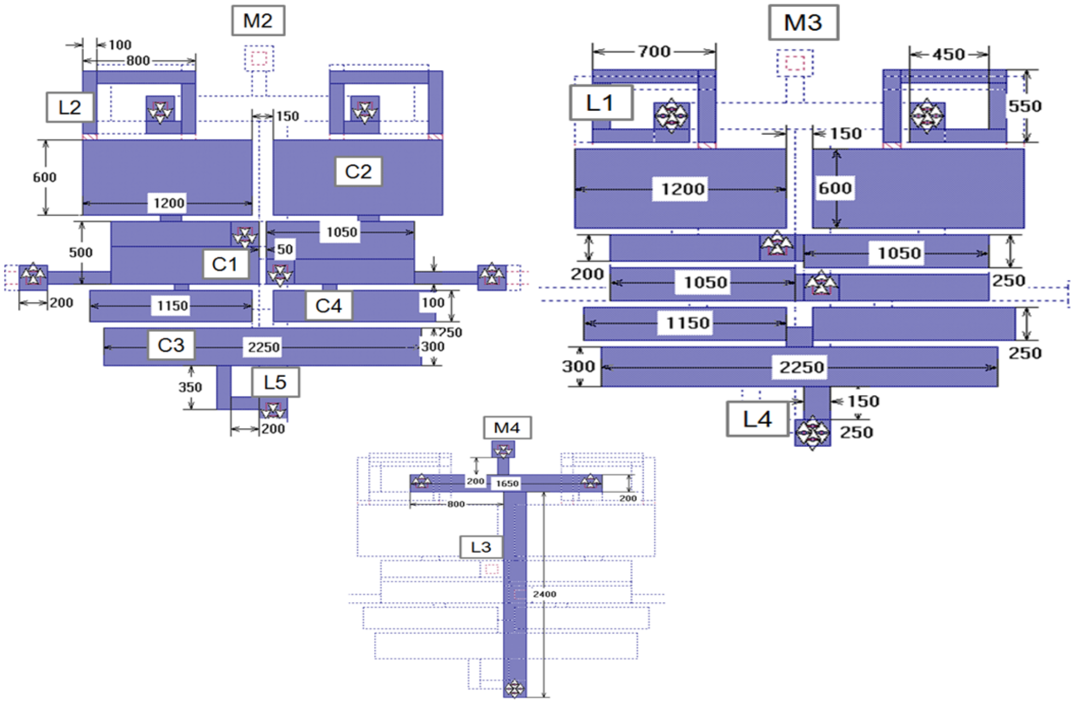

Figure 68. Dimension of the layout from metal layer two to four.

Figure 69 shows the x-ray photo of the fabricated filter showing very compact area of 2.55 mm by 2.8 mm, which is **the smallest WLAN dual-band filter** compare to any other prior designs.

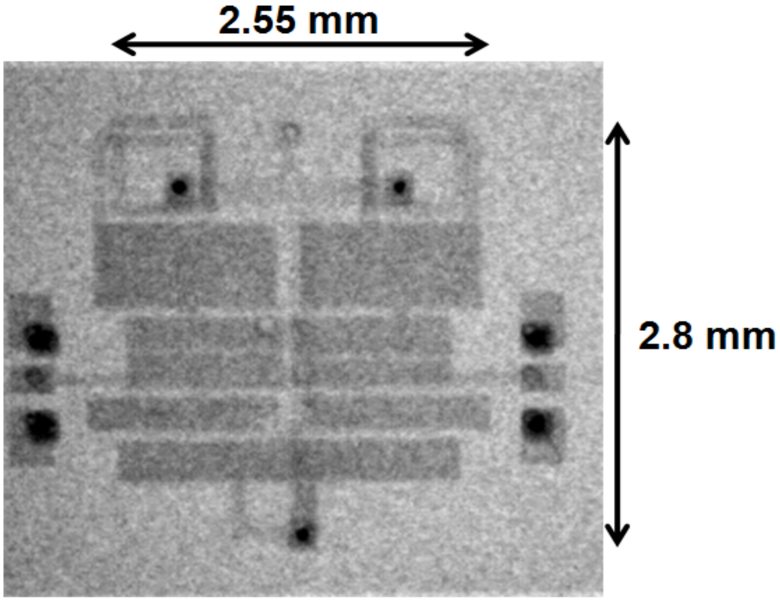

Figure 69. X-ray photo of the dual-band bandpass filter.

Figure 70 shows the correlation result with simulation and measurement for dual-band filter A. Based on the measurement, the measured result correlated almost perfectly with the simulation showing the effectiveness of the proposed topology. The measured dual-band filter A has the first passband at 2.65 GHz and a 3 dB bandwidth of 400 MHz. The return loss is lower than 11 dB, and the insertion loss is 1.65 dB at the center frequency. The second passband is centered at 5.5 GHz with 1.2 GHz 3 dB bandwidth while the return loss is better than 15 dB. The center frequency ratio is 2.07 while the fractional bandwidths are 14% and 22 % and the maximum bandwidth ratio is 3.

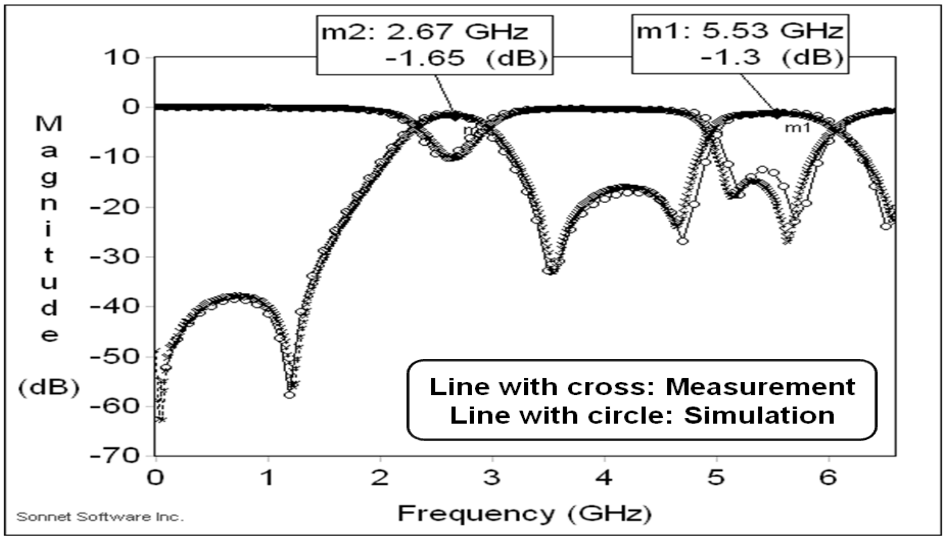

Figure 70. Measured and simulated result for dual-band filter A.

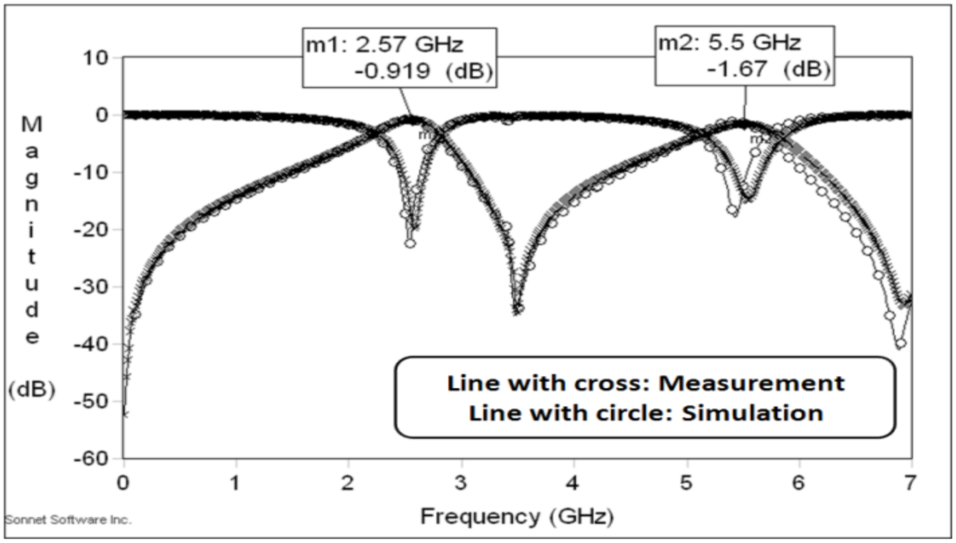

Figure 71. Measured and simulated result for dual-band filter B.

Dual-band filter B has been designed to show the controllability of bandwidth and center frequency of the proposed topology. Figure 71 shows the correlation result with simulation and measurement. Based on the measurement, the measured result correlated almost perfectly with the simulation as well. The measured dual-band filter B has the first passband at 2.57 GHz and a 3 dB bandwidth of 540 MHz. The insertion loss is 0.92 dB at the center frequency. The second passband is centered at 5.5 GHz with 3 dB bandwidth of 530 MHz. The center frequency ratio is 2.14 while the fractional bandwidths are 21% and 9.6 %.

Based on the narrow-band topology from Chapter 3, another dual-band bandpass filter was fabricated. Figure 72 shows the correlation result with simulation and measurement for dual-band filter C. Similar to the dual-band filter A and B, the measured result correlated almost perfectly as well. The measured dual-band filter C has the first passband at 2.46 GHz and a 3 dB bandwidth of 200 MHz. The return loss is lower than 20 dB, and the insertion loss is 2.3 dB at the center frequency. The second passband occured at 6.5 GHz with 800 MHz 3 dB bandwidth while the return loss is better than 25 dB. The center frequency ratio is 2.65 while the bandwidth ratio is 4, which are impossible to realize using the transmission line based method.

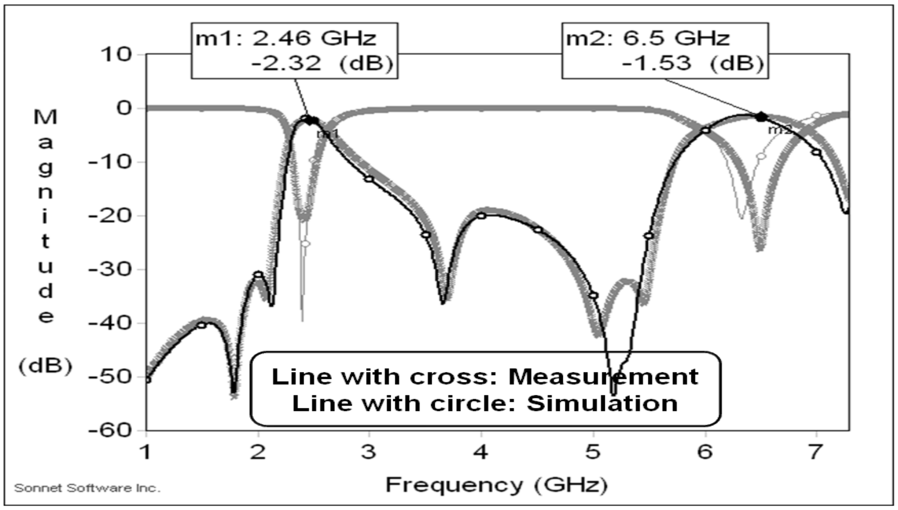

Figure 72. Measured and simulated result for dual-band filter C.

4.3 High-Rejection WLAN Duplexer in RXP

Using the high-rejection bandpass filters from Chapter 3, miniaturized high-rejection WLAN duplexer has been designed for the proposed dual-band module, which is shown in Figure 73. The major challenge in the proposed dual-band module is to design the duplexer as compact as possible as well as to maintain high performance because the passive component occupies the most area in the module while the duplexer is the most complicated, leading to the largest passive circuit.

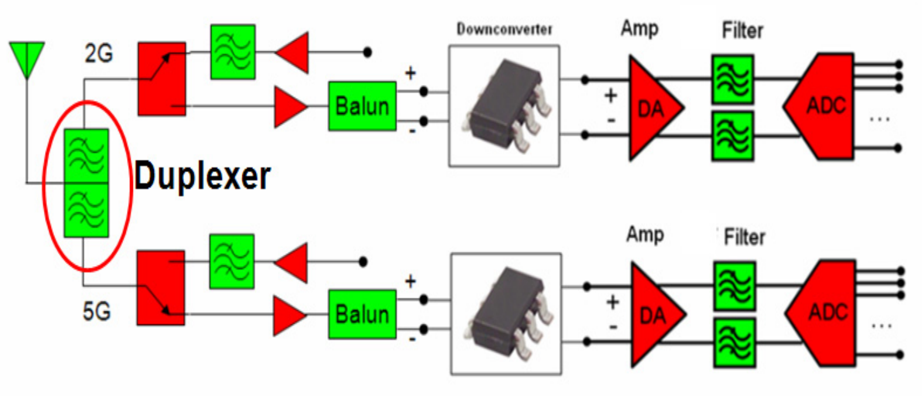

Figure 73. Block diagram of the proposed dual-band module.

The first step to design a miniaturized duplexer is to transport the 4-metal layer 2.4 & 5 GHz bandpass filters into 6-metal layer stack-up, which is shown in Figure 66. Since the top layer (M1 and M2) is thicker than the second layer (M2 and M3), the top metal layer has been avoided for layout because of the thicker substrate and larger 3D capacitor area. Taking the advantage of two additional layers from 6 metal layer stack-up, the size of 2.4 GHz BPF has been dramatically reduced. Since the grounding inductor in the 2.4 GHz layout does not need to be with other inductors and capacitors, it can be moved to other non-used layers such as the fourth metal layer (M4). By realizing the grounding inductor in M4 and optimizing other capacitors and inductors in M2 and M3, **41.6 % size reduction** has been made while high performance has been maintained as shown in Figure 74. For 5 GHz filter, 9.4 % size reduction has been achieved by moving the middle resonator to other side, as shown in Figure 75.

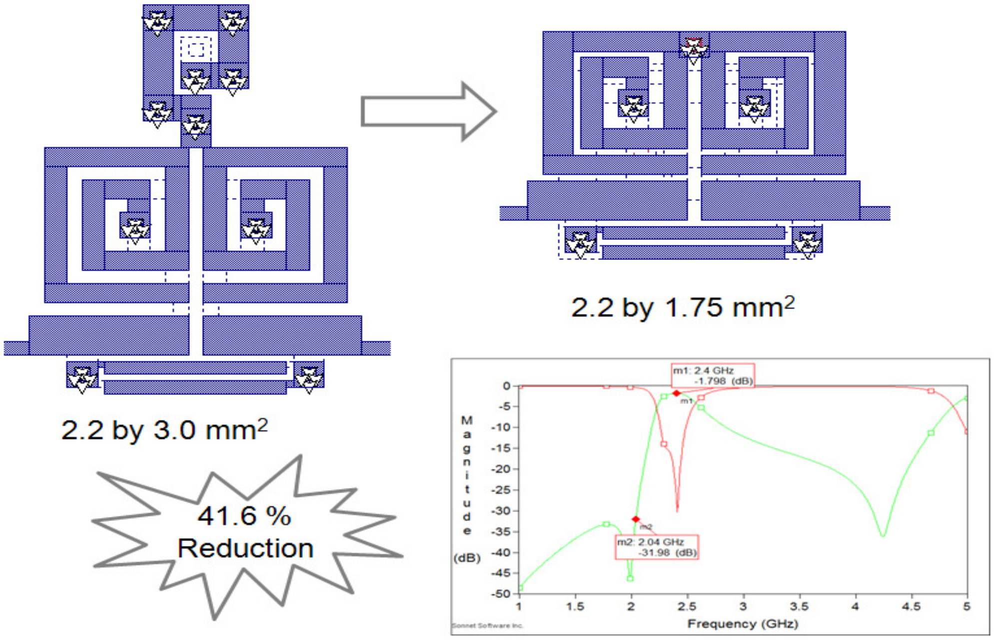

Figure 74. Size reduction for high-rejection 2.4 GHz BPF.

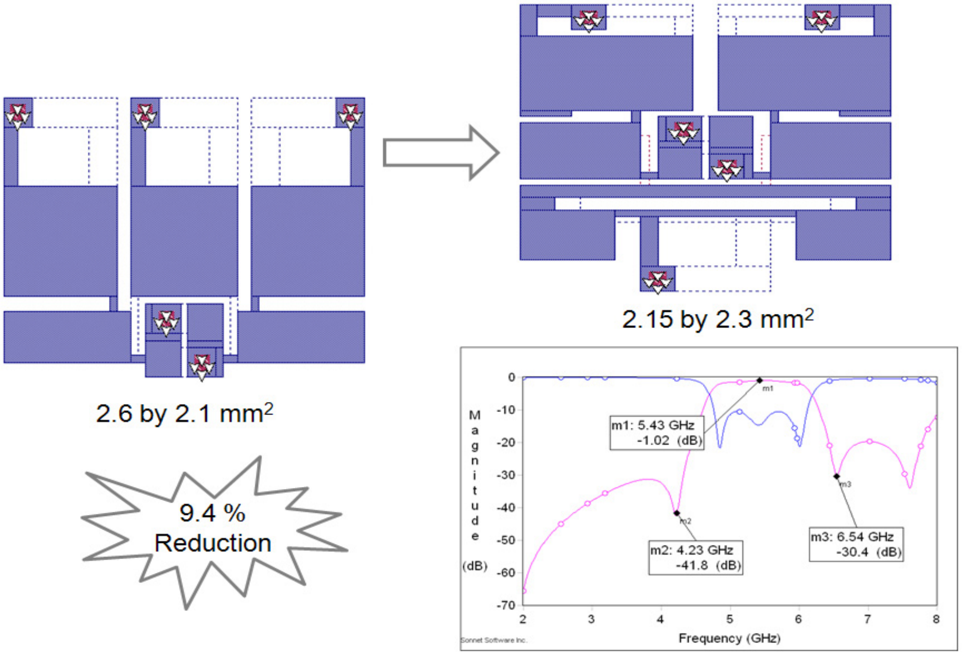

Figure 75. Size reduction for third-order 5 GHz BPF.

The next step is to design the matching circuit to connect the two separated band-pass filters. Since the matching circuit will introduce additional lumped-elements, it is necessary to minimize the number of inductors and capacitors in the matching circuit. The simplest matching circuit for the low-passband is to use the first-order LC lowpass filter while a highpass filter is used for the high-passband section. The initial inductor and capacitor for each low and highpass elements can be obtained using the classical design equation [73]. Then, each element should be tuned for optimization using the schematic shown in Figure 76.

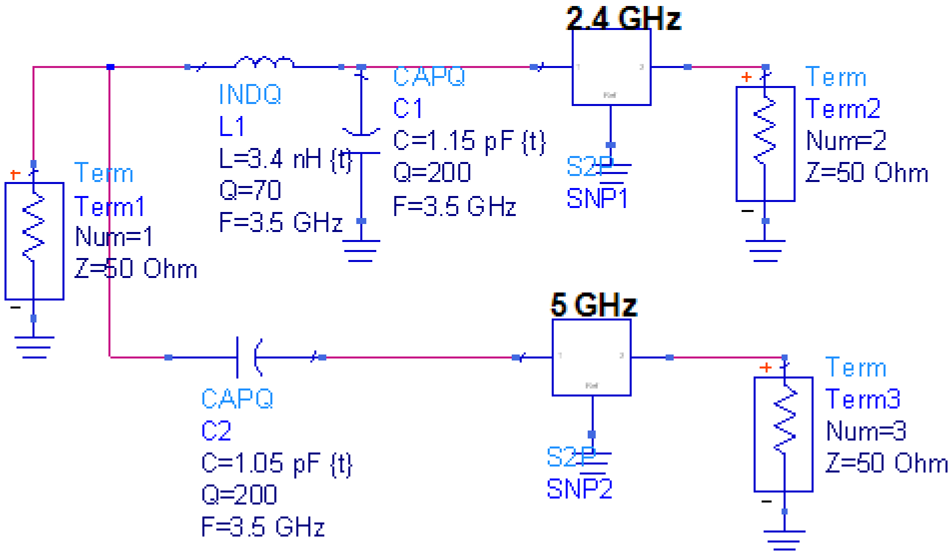

Figure 76. Matching circuit schematic in ADS.

Finally, two duplexers have been realized using the proposed bandpass filters and matching circuits. The duplexer A is composed of 2.4 GHz of Type 2 and 5 GHz of Type3 while duplexer B is made by connecting 2.4 GHz of Type 2 and 5 GHz of Type 2. The physical layout of duplexer A has a size of 2.9 mm by 4.0 mm as shown in Figure 77, and duplexer B only occupies 2.55 mm by 3.3 mm as shown in Figure 79. The measured results are shown in Figure 78 and Figure 80 where dotted lines are the simulation whereas solid lines with crosses are the measurement. Both duplexers have better than 3 dB insertion loss for 2.4 GHz and less than 1 dB insertion loss for 5 GHz. Although the 2.4 GHz was expected to have less than 2 dB insertion loss, the insertion loss has been affected mainly from the matching capacitor difference because of fabrication errors. Despite the fact that the measured results have been shifted by approximately 300 MHz to the right, the high rejection as well as good insertion loss has been maintained.

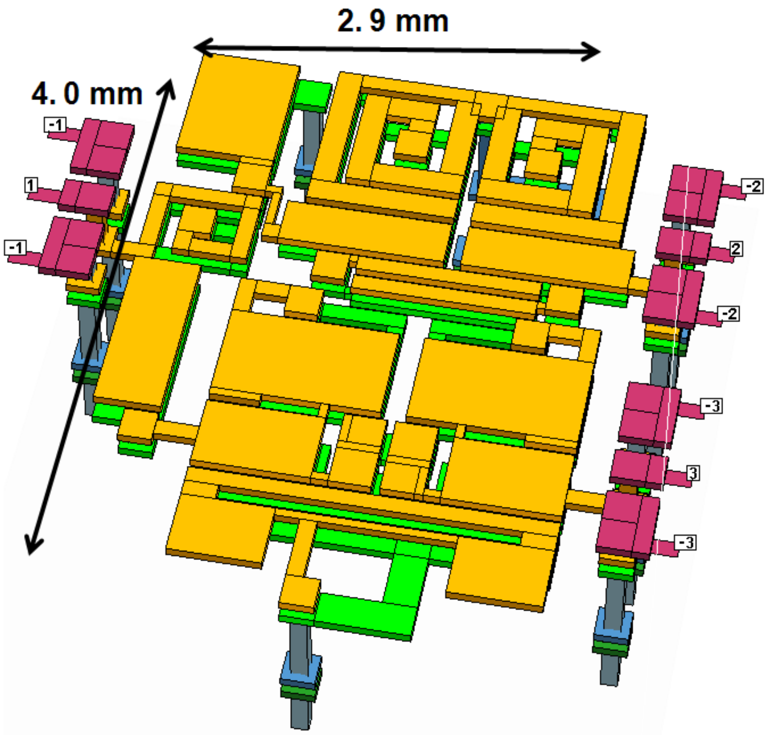

Figure 77. Physical layout of duplexer A.

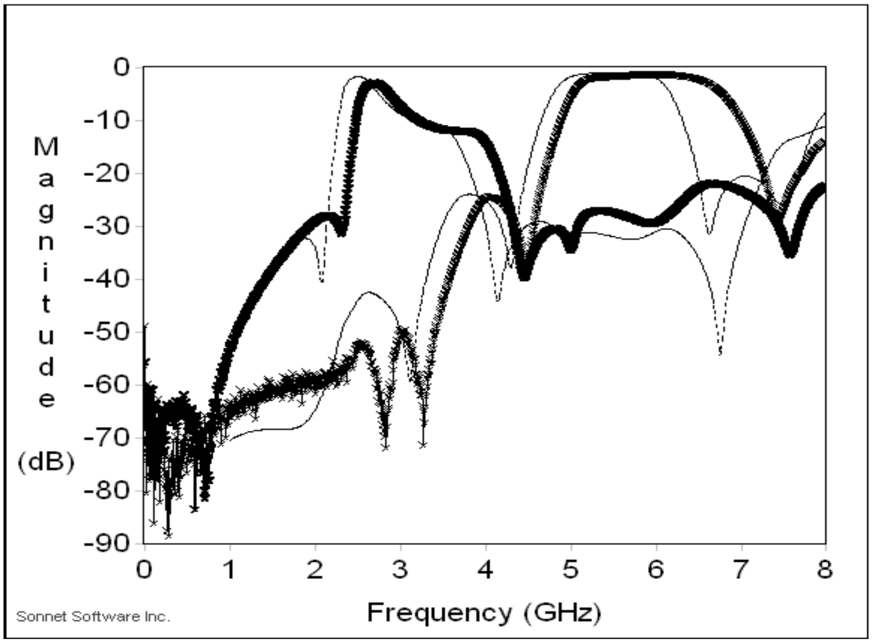

Figure 78. Correlation result of duplexer A.

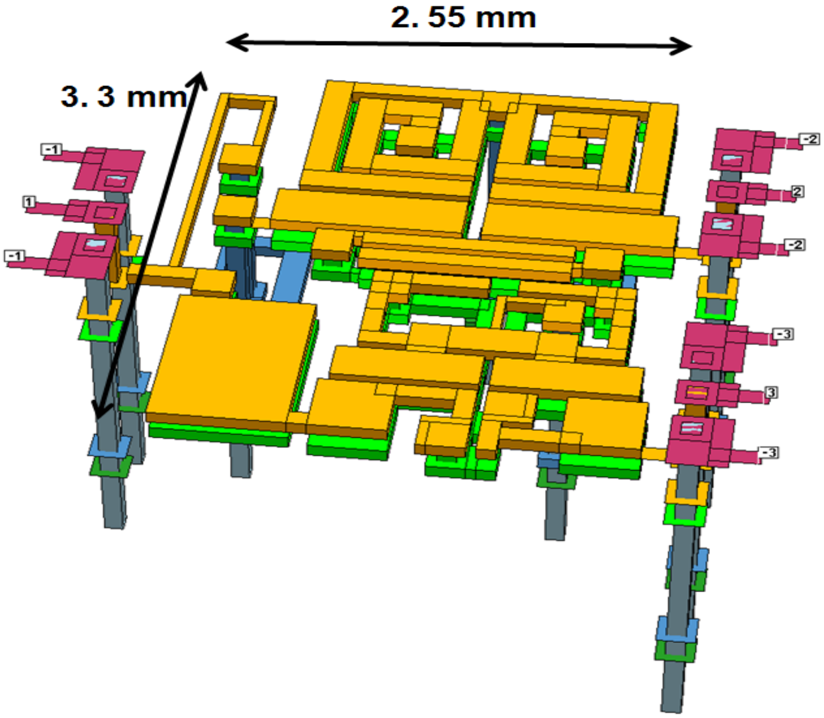

Figure 79. Physical layout of duplexer B.

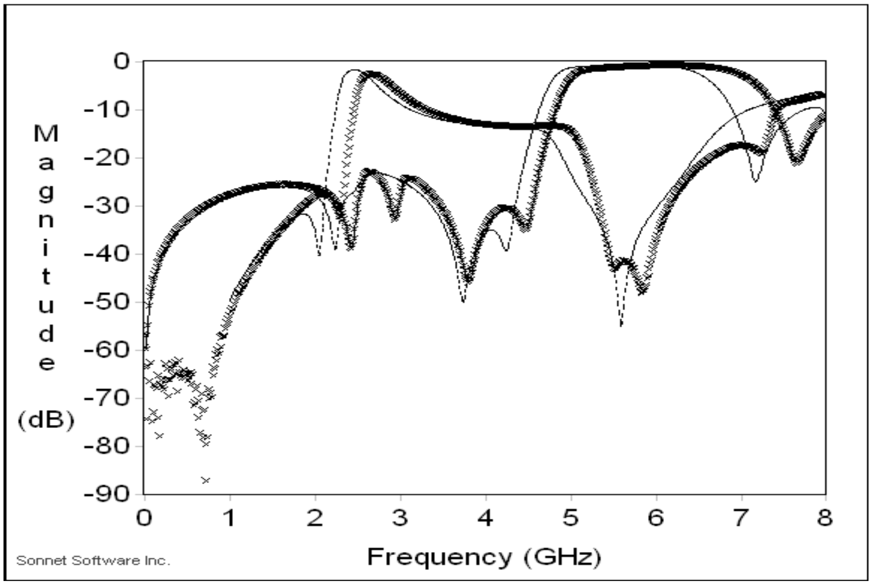

Figure 80. Correlation result of duplexer B.

4.4 Summary

This chapter presented lumped-element dual-band bandpass filters and duplexer using RXP technology for the first time. To overcome major limitations for the dual-band bandpass filter design using the transmission line based method, a new circuit topology that is based on a single high-rejection bandpass filter topology has been proposed. The design equations for individual lumped-elements have been provided and two dual-band bandpass filters have been designed and measured. The measured results showed excellent agreement with the simulation while the center frequency ratio of 2.65 and the bandwidth ratio of 4 were achieved, which are impossible to realize using the transmission line based method.

As an essential passive element in the dual-band module, highly miniaturized duplexer has been designed and measured. The high-rejection bandpass filters from Chapter 3 have been re-designed to utilize additional metal layers, which resulted in 41.6% size reduction for 2.4 GHz and 9.4% for 5 GHz. The resulting duplexer provides high-rejection performance, and it is the smallest duplexer reported up to date (3.3 mm x 2.55 mm x 0.26 mm).

CHAPTER 5

LUMPED-ELEMENT CIRCUITS AT MILLIMETER-WAVE FREQUENCY

Wireless communications have been a major aspect of everyday life, making it a rapidly increasing segment of communications industry. The evolution of wireless communications includes several indispensible technologies such as cellular communications, wireless local area networks (WLANs), and ultra wide band (UWB) technology spanning the frequency range from 800 MHz to 10 GHz. The consumer demand for accessing these radio technologies from a single handheld device has been pushing RF engineers for effective integration and miniaturization of RF components. There has been a considerable amount of effort in the past years to find and implement novel packaging technologies to achieve this goal.

Another technology operating around 60 GHz (V-band) has been emerging recently for high-speed short-range wireless communications and wireless personal area networks (WPANs). The miniaturization factors and high-speed communication that can be achieved at 60 GHz are especially attractive compared to those that can be achieved at WLAN/WiMAX frequencies. However, this emerging technology brings new challenges by widening the frequency range of interest for the mobile wireless industry to include millimeter-wave frequencies. Another issue arises regarding the performance and the maturity of the available integration techniques to support 60 GHz wireless communications.

Several packaging technologies have been proposed to achieve RF integration for the aforementioned wireless bands. RXP technology has a superior integration technique as discussed in Chapter 2 and 3. Therefore, RXP has been chosen for millimeter-wave integration. Figure 81 shows the integration techniques using multilayer RXP technology.

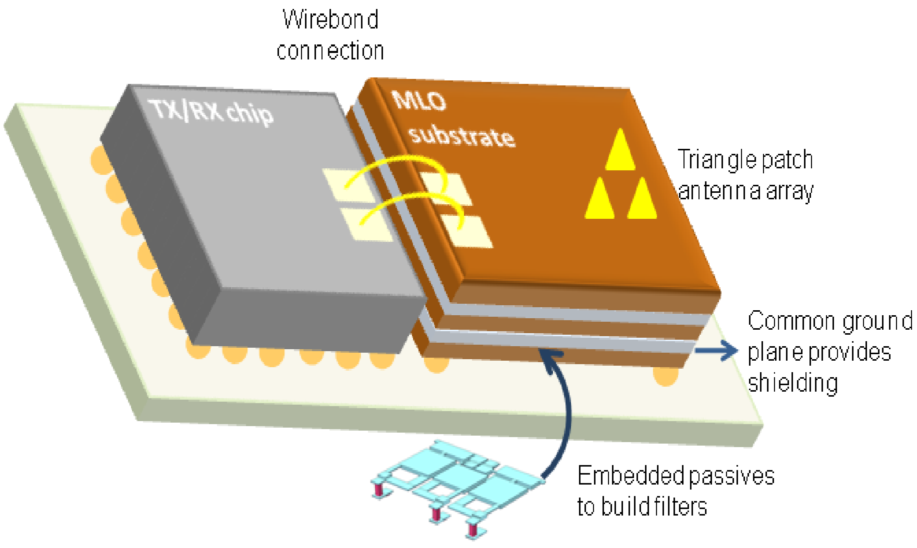

(a)

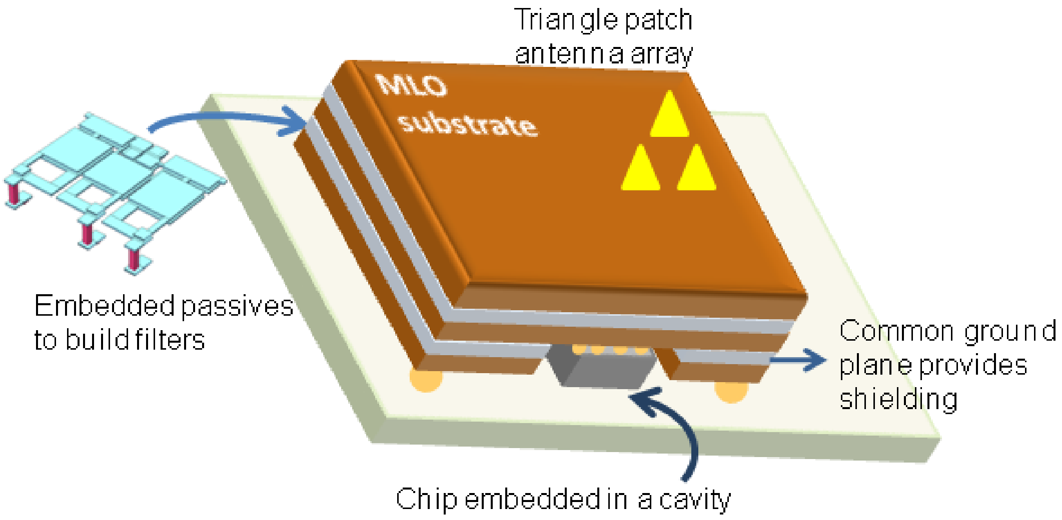

(b)

Figure 81. Conceptual integration techniques for RXP technology (a) A separate substrate passive components. (b) Chip embedded in a cavity.

As the first step, RXP substrates can be designed as a separate substrate for the antenna and the passive front-end components, as shown in Figure 81 (a). Next, the integration can be further improved by placing the chip in a cavity constructed in the RXP substrate, as shown in Figure 81 (b). To embed the chip inside of the RXP substrate, the four metal-layer RXP stack-up has been revised to the six metal-layer substrate.

This chapter focuses on the design of millimeter-wave passive circuits using lumped-element components. The proposed method to avoid the self-resonant frequency limitation for passive components is explained in Section 5.1. Simulated and measured 60 GHz lumped-element bandpass filter and dual-band bandpass filter are presented in Section 5.2 and Section 5.3, respectively. The simulated result of 57-64 GHz duplexer is shown in Section 5.4. Finally, the chapter is summarized in Section 5.5.

5.1 Limitation of Self-Resonant Frequency

Realization using embedded lumped-element filters for millimeter-wave application has not been reported before because of self-resonance frequency concern using lumped-elements. However, the barrier from self-resonance frequency can be overcome by using very small inductance and capacitance values. Passive components in millimeter-wave frequency requires much smaller inductance and capacitance than at lower frequency for the resonator behavior, and such small inductors and capacitors do not show self-resonance frequency up to very high frequencies.

To demonstrate the passive behavior at millimeter-wave frequency, a two-port equivalent circuit model can be used. As shown in Figure 82, capacitor or inductor can be represented as a π-network.

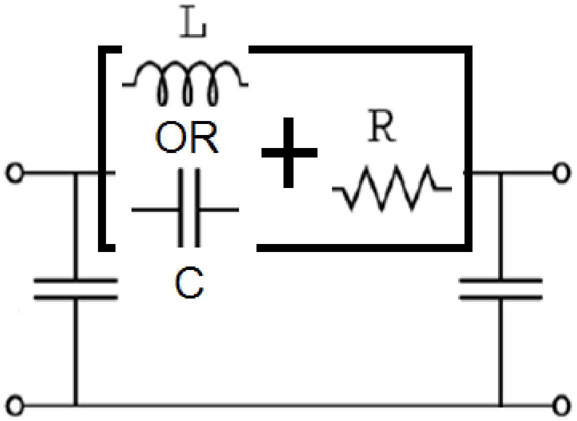

Figure 82. π-equivalent circuit model.

Since π-network can be expressed as admittance parameter as shown in Figure 40 from Chapter 3, Y21 can be calculated as

$$Y_{21} = \frac{-1}{j\omega L + R} \qquad \text{for the inductor} \qquad (43)$$

$$Y_{21} = \frac{-j\omega C}{1 + j\omega CR} \qquad \text{for the capacitor} \qquad (44).$$

Then, the frequency-dependent inductance and capacitance can be obtained using

$$L_{eff} = -\operatorname{Im}(\frac{1}{Y_{21}}) \cdot \frac{1}{\omega} \qquad (45)$$

$$C_{eff} = \frac{1}{\operatorname{Im}(\frac{1}{Y_{21}}) \cdot \omega} \qquad (46).$$

To verify the self-resonance frequency of 50 um by 150 um half turn inductor, the frequency-dependent inductor values are shown in the left axis of Figure 83. The inductor has 0.1185 nH at 1 GHz while it goes down to 0.1114 nH at 60 GHz. It is important to note that the inductor is still behaving as an inductor even at 100 GHz. The self-resonance frequency occurs at around 150 GHz. Moreover, the inductor has a quality factor of 145 because small metal strip is not affected by capacitance coupling, which is a major loss contribution for large spiral inductors.

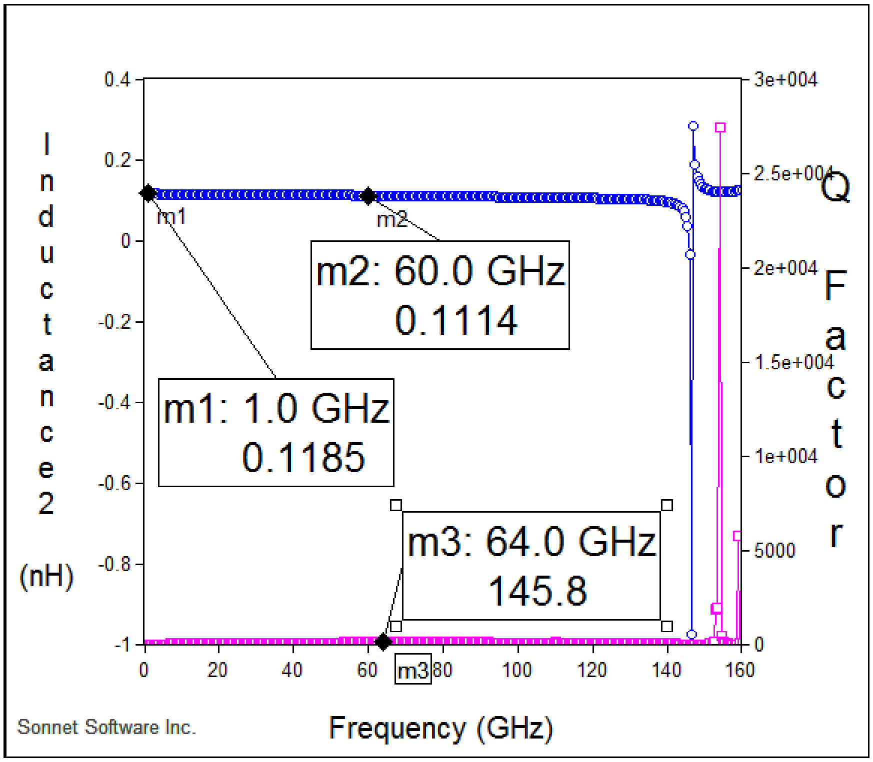

Figure 83. Inductance from 1 GHz to 160 GHz.

Similar to the inductor case, the self-resonance frequency does not occur before 100 GHz for the capacitor as well. Figure 84 shows the frequency response of the 50 um by 150 um parallel-plate capacitor. The 14 fF capacitor can resonate with 0.12 nH inductor at 122 GHz while the self-resonance frequency starts to occur only at 130 GHz.

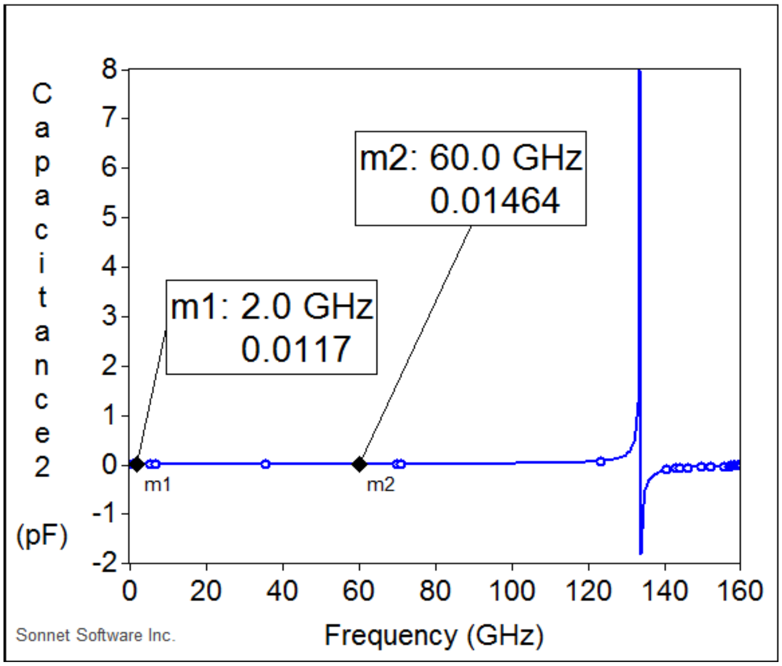

Figure 84. Capacitance from 1 GHz to 160 GHz.

Based on the behavior of <1 nH inductor and femto farad range capacitor, lumped-element passive circuits still can be realized at millimeter-wave frequency using the proposed technique.

5.2 Realization of 60 GHz Lumped-Element Bandpass Filter

As mentioned in Section 5.1, lumped-element bandpass filter in millimeter-wave frequency can still be realized. To find the circuit component values, the topology and design equations from Chapter 3 can be used. As shown in Figure 85, the capacitance values are in femto farad range while less than 1 nH inductance values are necessary. The corresponding component values are matching capacitor (C1) of 9.696 fF, feedback capacitor (C2) of 3.51 fF, resonator capacitor (C3) of 9.52 fF, resonator inductor (L1) of 0.305 nH, and grounding inductor of 0.1325 nH.

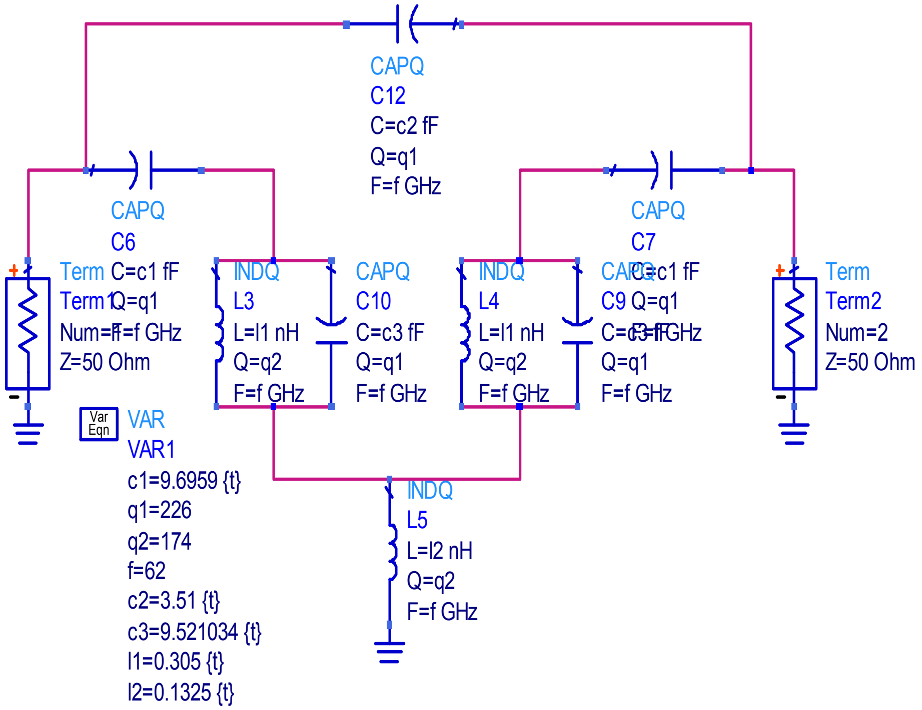

Figure 85. 60 GHz bandpass filter circuit schematic.

Figure 86 shows the simulation result of 60 GHz bandpass filter schematic. Two finite transmission zeros are generated and 3 dB bandwidth of 6 GHz is obtained. After verifying the bandpass behavior, physical layout is made using EM simulator. With the multilayer capability of RXP substrate, the lumped-elements can be realized by using a metal strip for the inductor and parallel plates for the capacitor. Figure 87 shows the physical layout, and Figure 88 shows its frequency response in EM simulator. Using the design rule in Figure 43 from Chapter 3, four metal-layer RXP substrate has been used for the layout. The blue metal corresponds to the top metal layer, the green metal represents the second metal layer, and the ground plane is located at the fourth metal layer (M4). The size of the layout is only 0.55 mm by 0.325 mm while less than 2 dB of insertion loss is maintained at the center frequency.

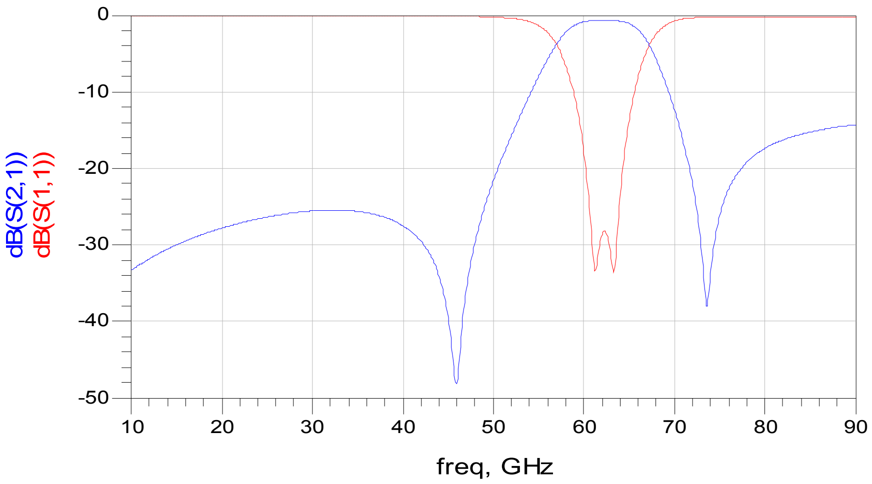

Figure 86. Simulation result of 60 GHz BPF in circuit simulator.

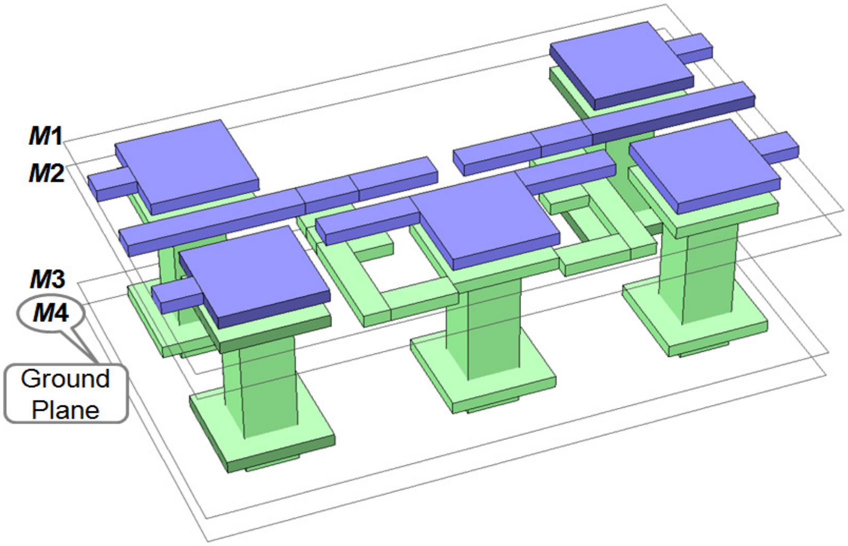

Figure 87. Physical layout of 60 GHz BPF.

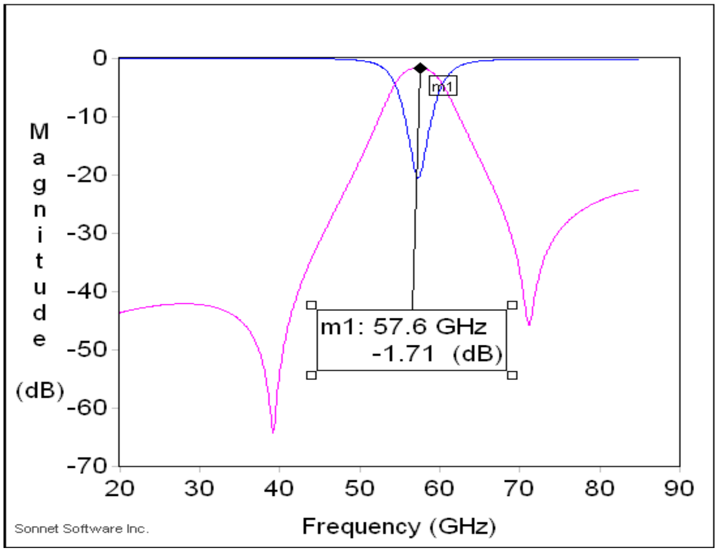

Figure 88. 60 GHz BPF response in EM simulator.

The measurement was carried out using short-open-load-thru (SOLT) calibration with Agilent PNA 8361C and GGB industries GSG-250 Pico probes. The prototype of 60 GHz BPF is shown in Figure 89 and correlation of measurement and simulation is presented in Figure 90. According to the measurement, the measured BPF responses had good correlation with the simulation in terms of operating frequency. This demonstrated that the extracted dielectric constant for RXP material from Chapter 2 was accurate. However, the measured result suffered from degraded insertion loss: the insertion loss from simulation was -1.7 dB whereas the measured insertion loss was -4.794 dB. The main reason of the insertion-loss degradation was the grounding probe contact. Because of fabrication misalignment, one of the ground probe tip could not contact perfectly on the ground pad. This resulted in almost open ground connection for the measurement. The reference plane becomes much more important at 60 GHz than < 10 GHz. Therefore, the measurement suffered from degraded insertion loss.

Figure 89. Fabricated 60 GHz BPF.

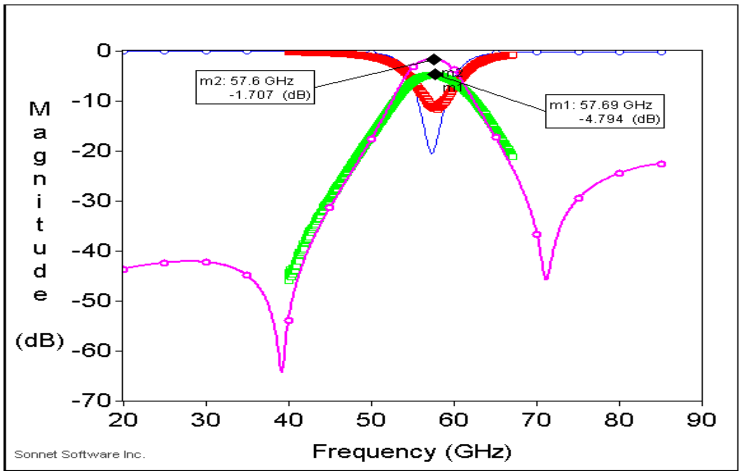

Figure 90. 60 GHz BPF measurement correlation.

5.3 Realization of 60 GHz Lumped-Element Dual-Band Bandpass Filter

Using the similar technique from Chapter 4, dual-band bandpass filter can be realized by utilizing transmission zero locations. The topology shown in Figure 91 has been used and the corresponding component values are matching capacitor (C_1) of 30 fF, feedback capacitor (C_2) of 4 fF, resonator capacitor (C_3) of 10 fF, resonator inductor (L_1) of 0.49 nH, series inductor (L_3) of 0.66 nH and grounding inductor (L_2) of 0.22 nH. To improve the second passband characteristic, the matching inductor (L_m) of 0.1 nH has been added. Figure 92 shows a simulation result of 60 GHz dual-band bandpass filter in the circuit simulator.

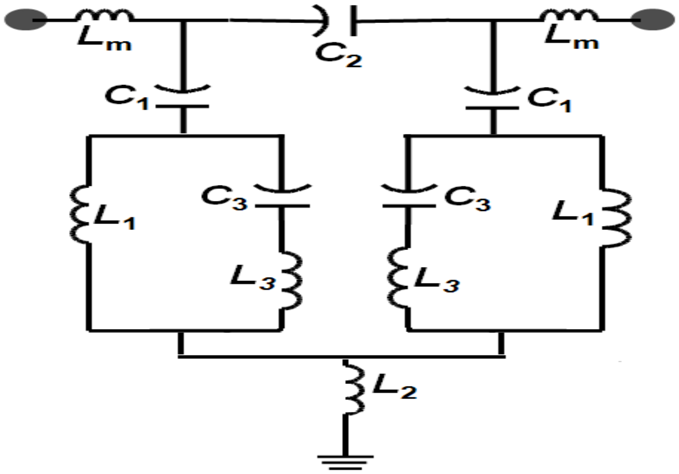

Figure 91. 60 GHz dual-band BPF topology.

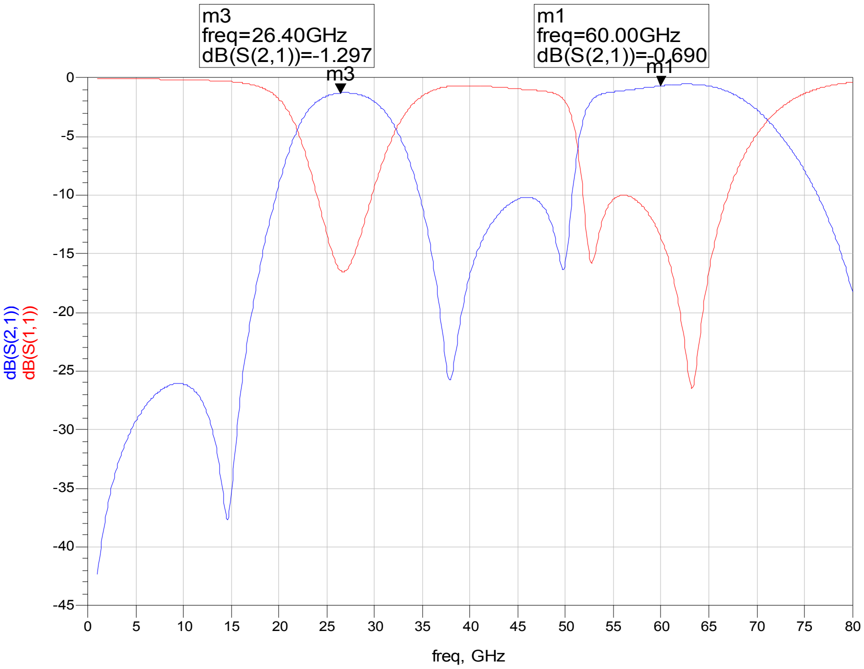

Figure 92. Simulation result of 60 GHz dual-band BPF in circuit simulator.

Since the proposed topology generates four transmission zeros, the four transmission zeros distributed at low and high passbands are observed in the millimeter-wave frequency as well. The low passband occurs at 26 GHz while the high passband is centered at 60 GHz. The center frequency of each passband can be scaled to a different frequency, but minimum passband spacing is about 20 GHz. After obtaining all of lumped-element values, each element is replaced by a corresponding layout. The layout has been done in six metal-layer RXP substrate as shown in Figure 93. Two 60 um RXP4 layers have been added for the purpose of embedding IC. Only M1 to M3 has been used for the layout while M6 serves as the ground plane.

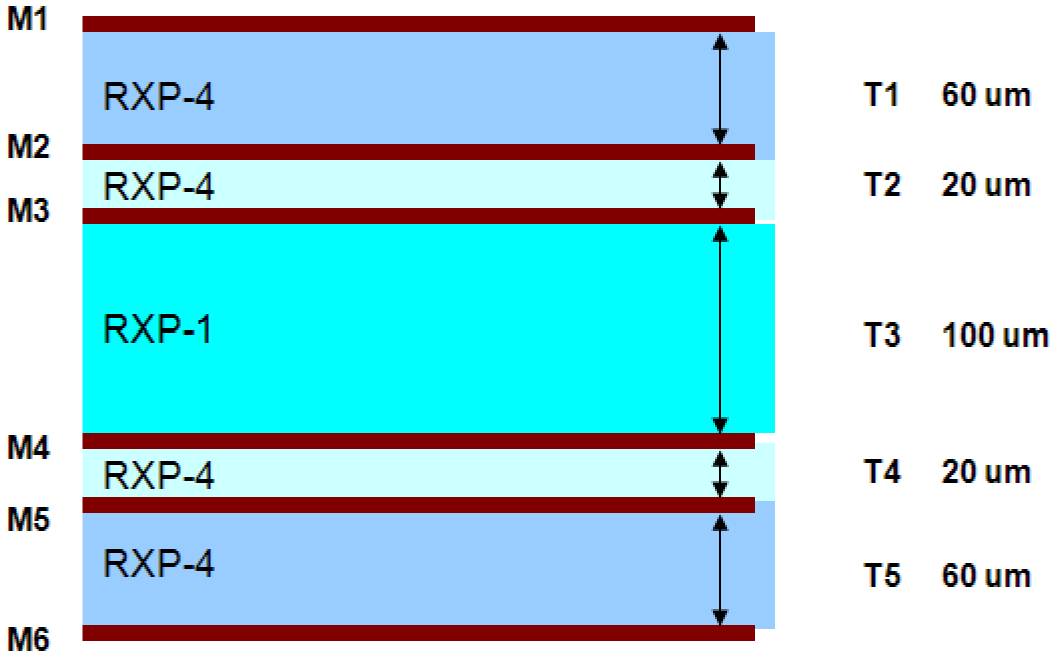

Figure 93. Six metal-layer RXP stack-up.

Figure 94 shows the physical layout where the each color represents the different metal layer: the red corresponds to the top metal layer, the yellow represents the second metal layer, and the green shows the third metal layer. Figure 95 shows the dimension of each lumped-element in $M1$ and $M2$. Parallel-plate capacitor is used for the resonator capacitor while a planar inter-digitated capacitor is used for the feedback capacitor. The size of the layout is 1.3 mm by 0.75 mm. The dimensions of inductors and capacitors are follows: W_{Lm} = 0.1 mm, L_{Lm} = 0.15 mm, W_{c1} = 0.2 mm, L_{c1} = 0.3 mm, W_{c2} = 0.1 mm, L_{c2} = 0.3 mm, W_{c3} = 0.3 mm, L_{c3} = 0.25 mm, W_{L1} = 0.25 mm, and L_{L1} = 0.175 mm. As shown in Figure 94, the series inductor (L_3) has been realized using a via from $M1$ to $M2$ with 200 μm by 50 μm metal strips. Likewise, the grounding inductor has been realized using a via from $M2$ to the ground layer. The simulated layout is expected to have 1 dB insertion loss at 30 GHz, and 1.8 dB at 62 GHz as shown in Figure 96.

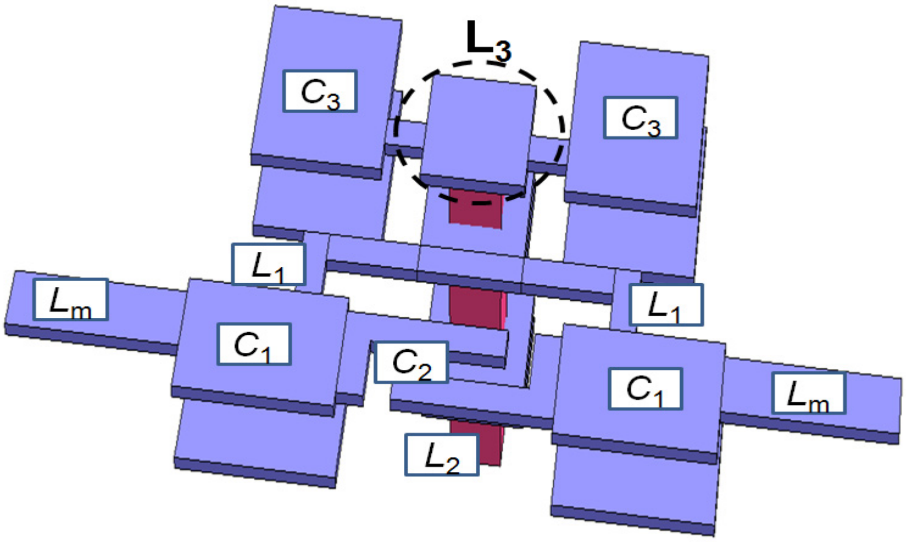

Figure 94. Physical layout of 60 GHz dual-band BPF.

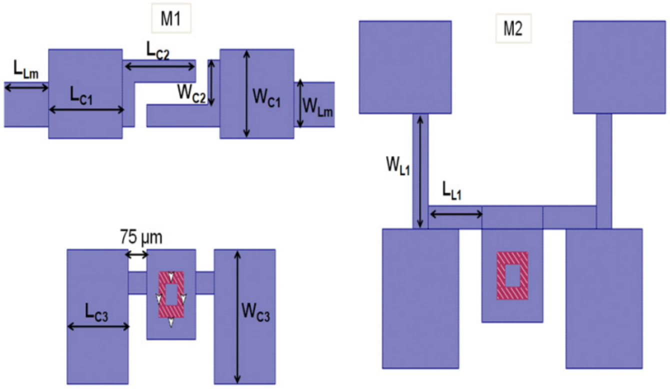

Figure 95. Dimensions of layout from M1 to M2.

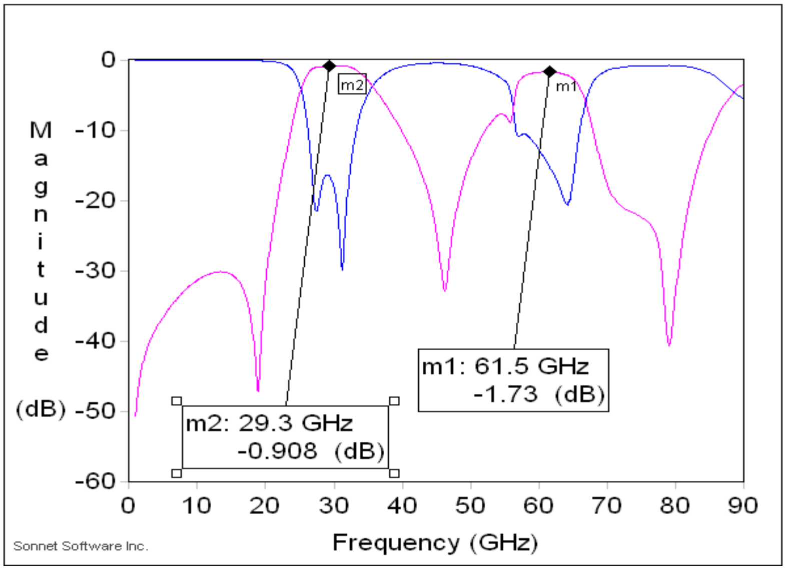

Figure 96. Frequency response of 60 GHz dual-band BPF in EM simulator.

The measurement was carried out using short-open-load-thru (SOLT) calibration with Agilent PNA 8361C and GGB industries GSG-250 Pico probes. The fabricated prototype is shown in Figure 97 and the correlation with measurement and simulation is presented in Figure 98. Compared to the fabrication quality from Chapter 3, the six metal-layer RXP substrate was not fabricated as accurate as the first tape out. As shown in Figure 97, the via diameter was more than twice bigger than what it was designed (100 µm), which will significantly affect the inductance values for L3 and L2 especially at the millimetre-wave frequency. In addition, the line width was not maintained uniformly, which will affect the passive values.

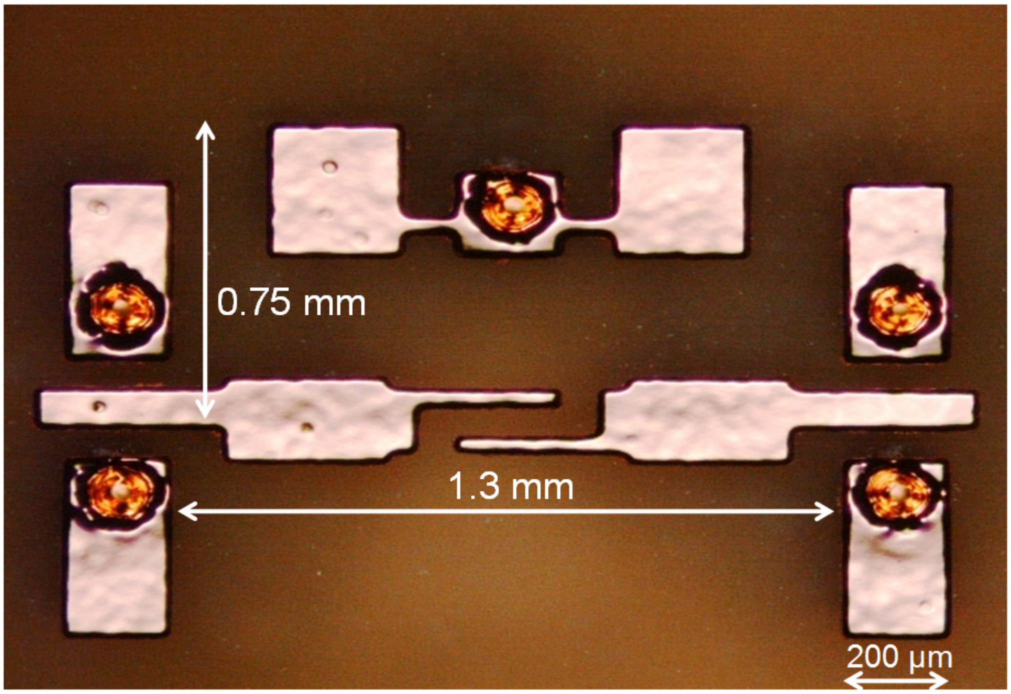

Figure 97. Fabricated 60 GHz dual-band BPF.

Since the prototype was not fabricated as designed, good correlation result could not be obtained. Figure 98 shows the measurement correlation with simulation result. The grey line with crosses shows the measured results whereas the black line with circles represents the simulated results. As it can be seen in Figure 98, there are about 2 GHz shift in the first passband while the insertion loss is affected in the second passband.

These effects mainly come from the inaccurate matching capacitance and large passive values from the resonance tank, which was caused by the fabrication error. However, the overall performance still validates the proposed topology and design idea by **showing a dual-band response in millimeter-wave frequency** as shown in Figure 99. The measured insertion loss for the first passband was 1.36 dB while the measured insertion loss for the second passband was -3.79 dB at the center frequency.

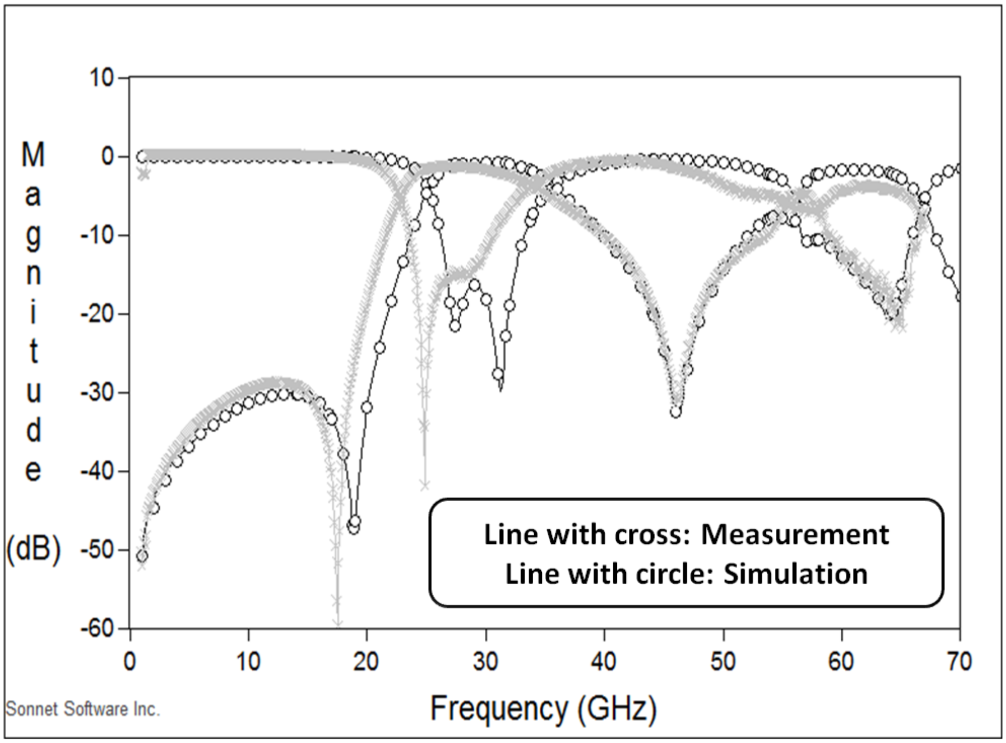

Figure 98. Correlation result with measurement.

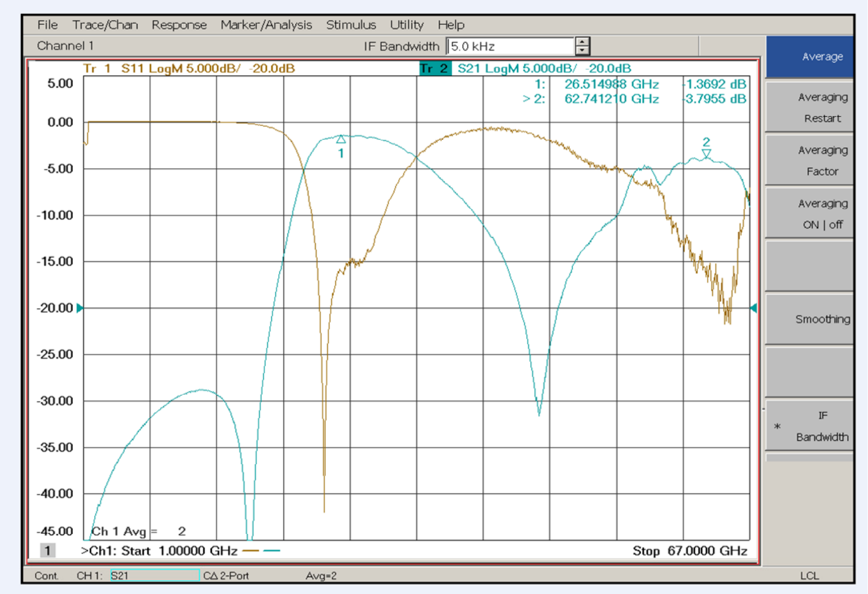
IF Bandwidth 5.0 kHz

Tr 1 S11 LogM 5.000dB/ -20.0dB

Tr 2 S21 LogM 5.000dB/ -20.0dB

1: 26.514988 GHz -1.3692 dB

> 2: 62.741210 GHz -3.7955 dB

Ch 1 Avg = 2

>Ch1: Start 1.00000 GHz

Stop 67.0000 GHz

Cont. CH 1: S21 C∆ 2-Port Avg=2 LCL

Figure 99. Screen shot of VNA for dual-band 60 GHz BPF.

5.4 Design of 60 GHz Duplexer

There are several challenges such as low insertion loss and sharp cut-off response outside of the passband for the integration of 60 GHz duplexer. A duplexer with RX (57-60GHz) and TX (62-66GHz) bands consisting of two bandpass filters and matching networks was also designed with the size of 1.05 mm x 1.38 mm x 0.2 mm using a similar duplexer design procedure from Chapter 4. Figure 100 shows a physical layout of the duplexer and a simulated frequency response of the duplexer is shown in Figure 101. From the simulation results, the insertion loss was 2 dB at 58.5 GHz and 1.9 dB at 64.2 dB while it provided high rejection at the outside of the passband.

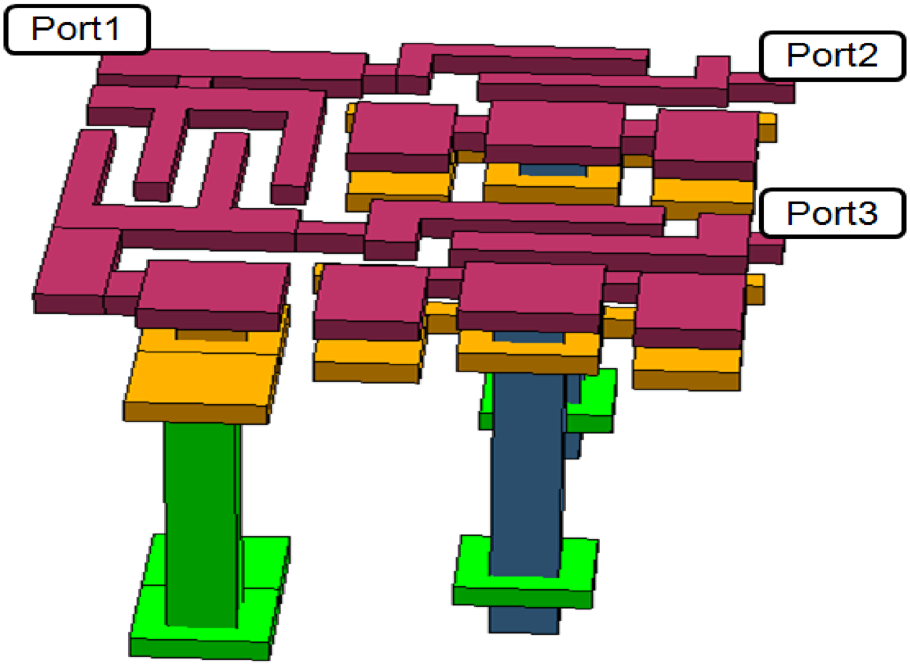

Figure 100. Layout of 60 GHz duplexer.

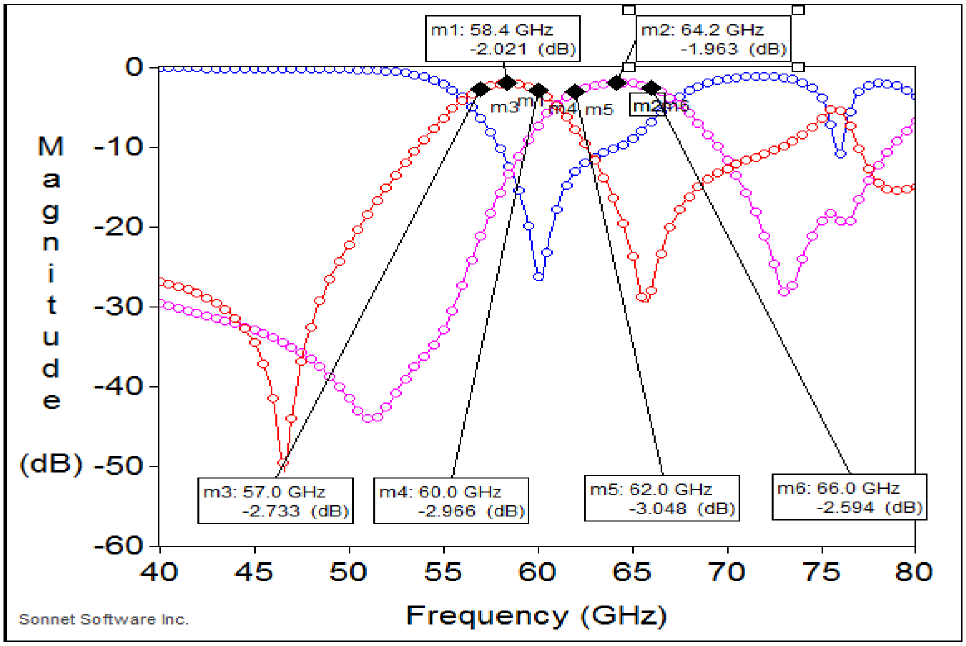

Figure 101. Simulated response of 60 GHz duplexer.

5.5 Summary

This chapter presented lumped-element passive circuits at millimeter-wave frequency (20-67 GHz) for the first time. The lumped-element passive circuits in millimeter-wave frequencies were not conducted before because of the self-resonance frequency concern. However, the proposed idea of shifting the self-resonance frequency into 100 GHz range and advanced fabrication technology enables the design of lumped-element passive circuits at millimeter-wave frequency.

As proof of concept, 60 GHz lumped-element bandpass filter was designed at center frequency of 57.6 GHz and correlated with the measurement result. The measured responses overlapped well with the simulation, which demonstrates that the extracted dielectric constant for RXP material from Chapter 2 was accurate. However, the measured performance was degraded especially for the insertion loss because of the measurement pad issue from the fabrication. Using the same idea from Chapter 4, 60 GHz dual-band bandpass filter was realized as well. The measured insertion loss for the first passband was 1.36 dB at 27 GHz while the measured insertion loss for the second passband was 3.79 dB at 63 GHz. Although insertion loss at 63 GHz was deteriorated because the prototype was not fabricated as designed, the measured result validates the proposed idea since it shows a dual-band response at millimeter-wave frequency. Finally, the simulation result of 57-64 GHz high-rejection duplexer has been shown. Another design fabrication with high accuracy is recommended as a part of the future work.

CHAPTER 6

FILTER DESIGN IN SILICON INTERPOSER USING THROUGH-SILICON VIA (TSV) TECHNOLOGY

Passive circuits from Chapter 3 to Chapter 5 have focused on organic low-loss substrate because RF passive components such as capacitors, filters, antennas, and high-Q inductors are best supported in SoP-based low-loss substrate rather than on silicon. For example, the highest Q factors reported on silicon are about 10-25, in contrast to 100-200 achieved in SoP substrate [10]. In addition, the loss in organic based capacitor is at least 10 times smaller than high-loss inorganic substrate such as silicon.

Low cost system has been a key for the product success. Although SoP-based organic technology provides better passive performance, silicon technology has been the major driving force for low-cost system integration. Recently, silicon based 3D system in package (SiP) technology has got attention because of through-silicon via (TSV) technology and high density integration possibilities. Along with high integration capability of silicon technology, silicon interposer can provide next packaging technology step with TSV technology as shown in Figure 102. In addition, thin-film integrated passive technology in silicon is currently being investigated, which is similar to organic embedded technology [88]. According to [88], the commercialization of interposers will arrive in two year and the article noted that TSV can offer miniaturization opportunities, higher performance, and power reduction.

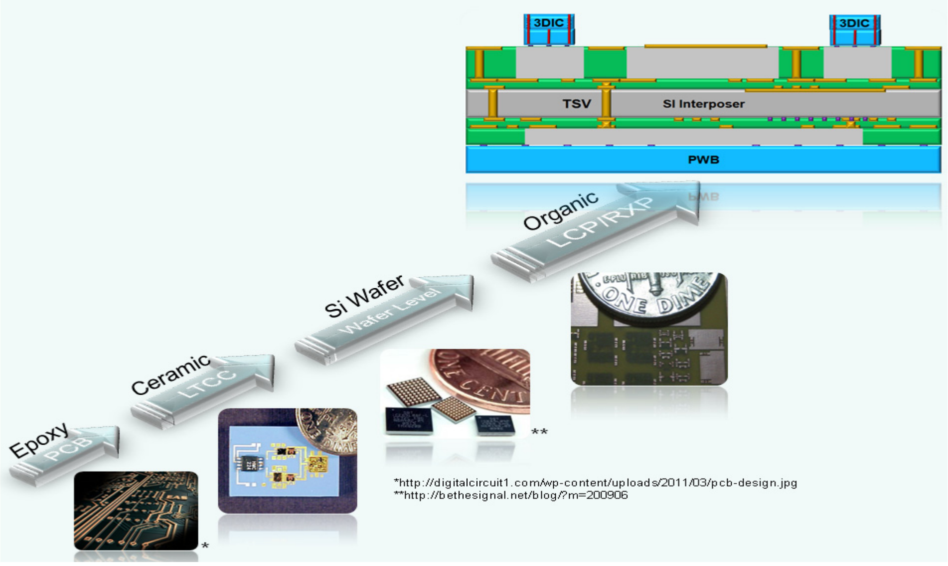

*http://digitalcircuit1.com/wp-content/uploads/2011/03/pcb-design.jpg
**http://bethesignal.net/blog/?m=200906

Figure 102. Roadmap of package technology.

TSV technology has been well known for better electrical characteristics of smaller parasitic than wirebonds [89]. TSV can enable 3D chip stacking for increasing signal-processing speed and decreasing power consumption [90]. However, the conventional filter design in silicon interposer is difficult because the high-loss from the silicon substrate leads to insertion loss degradation for the passband response.

This chapter focuses on filter design methodology for silicon interposer with TSV technology. The following section discusses the effect of substrate loss for filter performance using the conventional filter topology. Section 6.2 presents a new design methodology for filter realization on high-loss substrate. The validation based on high-loss FR4 substrate using through-hole via is presented in Section 6.3. Section 6.4 shows RF characteristic of TSV compared to the through-hole via and provides an analysis of different TSV characteristic. Filter layout in silicon interposer using TSV and its simulation results are shown in Section 6.5, and the chapter is summarized in Section 6.6.

6.1 Effect of Substrate Loss on Conventional Filter Design

Insertion losses from high-loss material such as PCB and silicon become a major issue at frequency beyond 1 GHz. For example, typical FR4 substrate begins to exhibit high insertion loss at approximately 1.5 GHz when distributed filters and circuits or microstrip topologies are used [91]. This kind of insertion loss degradation mainly affects the passband performance in the filter response. As discussed in Chapter 4, there are two types of filter design method, namely distributed-element and lumped-element. Although both methods have their own topology and design procedure, the filter performance of both methods degrades due to the substrate loss.

To show the effect of the substrate loss on distributed-elements, simulation results of edge-coupled microstrip bandpass filter [69] is shown in Figure 103.

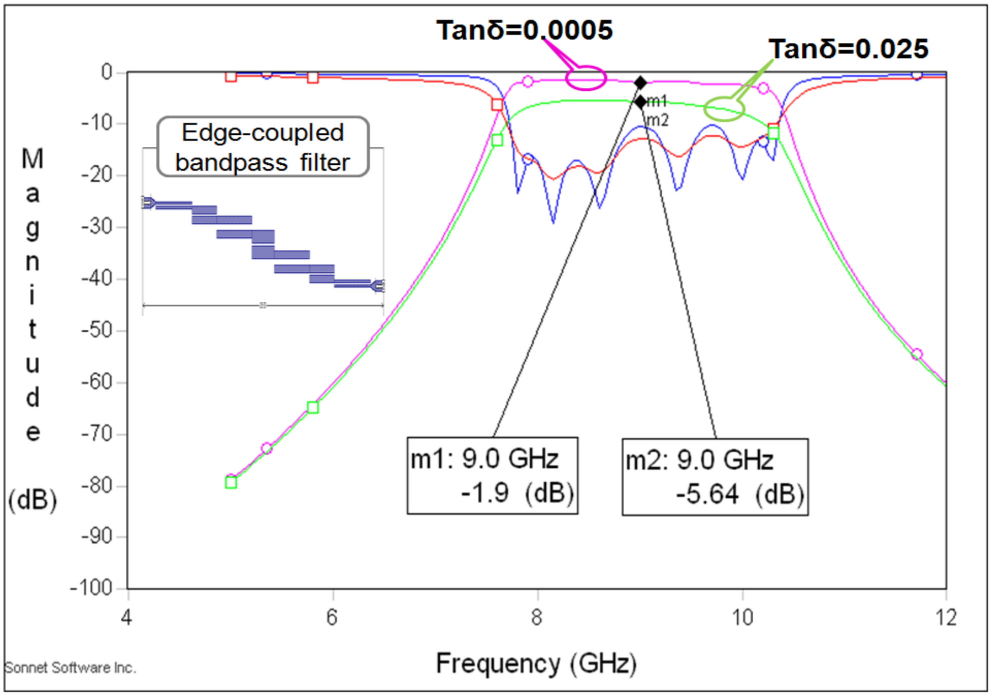

Figure 103. Simulation result of edge-coupled bandpass filter.

The filter is realized on alumina substrate with dielectric constant of 9.9 and loss tangent of 0.0005. The size of filer is 25.53 mm x 3.175 mm, which is significantly larger than lumped-element filters. The pink line is the insertion loss from loss tangent of 0.0005 while the green line shows the insertion loss from FR4 loss tangent of 0.025. Without changing any layout geometry, it is clear to see that the passband response is severely degraded from -1.9 dB to -5.64 dB because of the substrate loss.

The substrate loss also affects the passband response on the lumped-element filter. To illustrate the substrate effect at the circuit level, the narrow-band filter topology that includes the inductor quality factor as series resistances (R5, R6, R7) and the capacitor quality factor as shunt resistances (R1, R2, R3, R4, R8) is shown in Figure 104. The frequency response shown in Figure 104 is based on using lossless components: C1= 0.5 pF, C2=0.23 pF, C3=1.35 pF, L1=1.98 nH, L2= 0.9 nH.

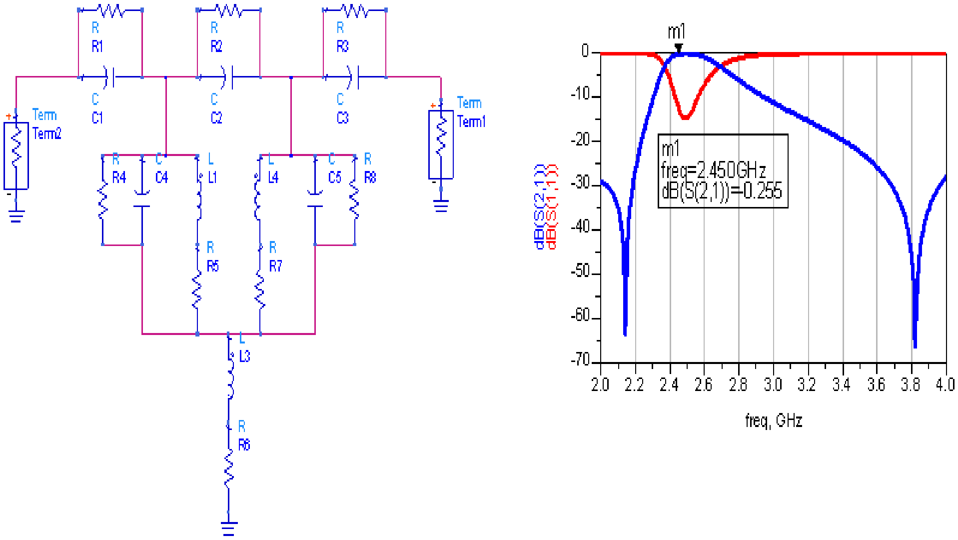

Figure 104. Conventional filter topology with dielectric loss.

The series and parallel resistances can be calculated using quality factor equation as

$$R_{series} = \frac{2\pi f \cdot L}{Q} \tag{47}$$

$$R_{parallel} = \frac{Q}{2\pi f \cdot C} \tag{48}$$

Assuming the best quality factor (Q @ 2.4 GHz) from a high-loss substrate is 40, 754 mΩ series and 5.3 kΩ parallel resistances are added for inductors and capacitors, respectively. After adding the series resistance only, the insertion loss is degraded from -0.255 dB to -3.044 dB as shown in Figure 105 (a). For the capacitor case, the insertion loss deteriorates to -2.305 dB. From this behavior, it can be stated that the inductor Q is more sensitive to insertion loss than the capacitor Q. If the lumped-element filter is designed on high-loss substrate, the passband response is significantly degraded as shown in Figure 105 (c).

In case of the low-loss substrate, the realizable Q is 70 for the inductor and 400 for the capacitor. These quality factors correspond to 430 mΩ series and 53 kΩ parallel resistances using (47) and (48). Figure 105 (d) shows that the insertion loss is changed to -1.88 dB by including the low-loss inductor whereas the insertion loss is slightly increased to -0.47 dB for the low-loss capacitor as shown in Figure 105 (e). Although, the inductor Q is more sensitive to insertion loss than capacitor Q, the good passband response is maintained by using low-loss capacitor from a low-loss substrate because the loss effect from capacitor (-0.470 dB) is much smaller than the loss effect from inductor (-1.886 dB).

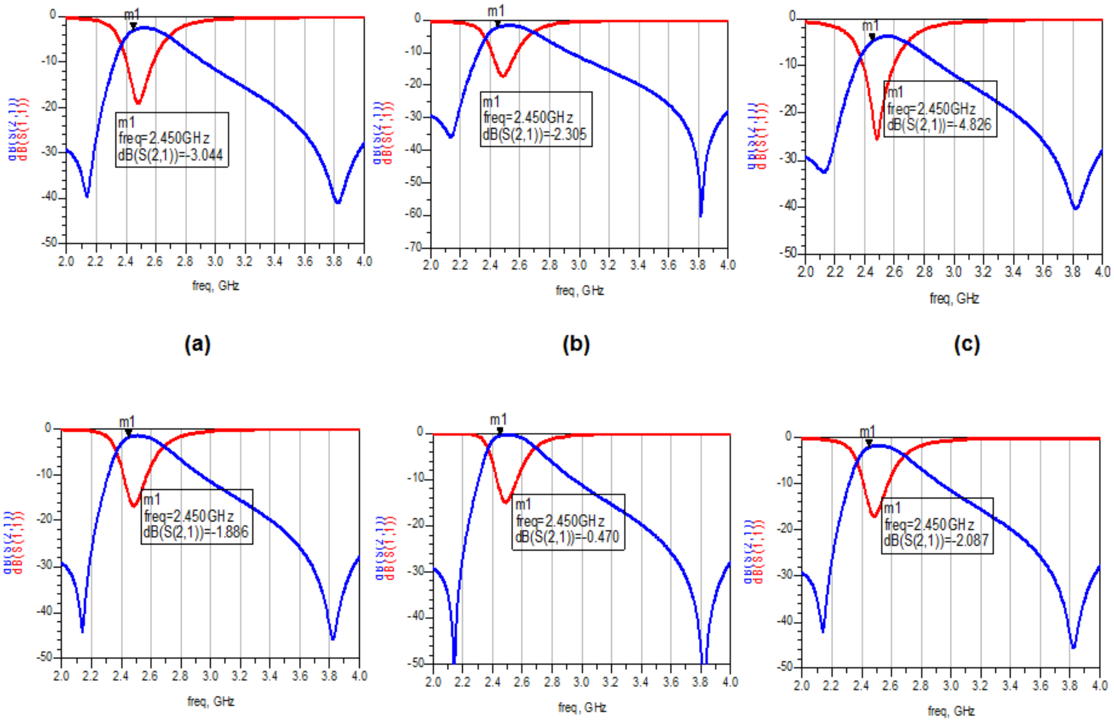

(a) (b) (c)

(d) (e) (f)

Figure 105. Effect of dielectric loss on filter performance. (a) High-loss L (b) High-loss C (c) High-loss L&C (d) Low-loss L (e) Low-loss C (f) Low-loss L&C

6.2 Filter Design in High-Loss Substrate

From Section 6.1, two design guidelines can be obtained to achieve good insertion loss for the high-loss substrate. The first one is to avoid the use of strip inductor since the loss in the inductor is more sensitive to insertion loss than the capacitor. The second is to reduce number of capacitor elements because the loss in the capacitor is more affected than the inductor by using the high-loss substrate.

Considering the second design guideline, an important filter passband characteristic can be observed by looking at the filter response as a frequency-dependent capacitor.

Figure 106 represents the filter response as a frequency-dependent capacitance. The filter is based on 5 GHz 3rd order filter from Chapter 3 except that the loss tangent has been changed from 0.004 to 0.025 in order to model the high-loss substrate. The pink line is the insertion loss, the blue line is the return loss, and the red line shows the capacitance as a function of frequency. It can be seen that the good passband response has deteriorated because of the high substrate loss.

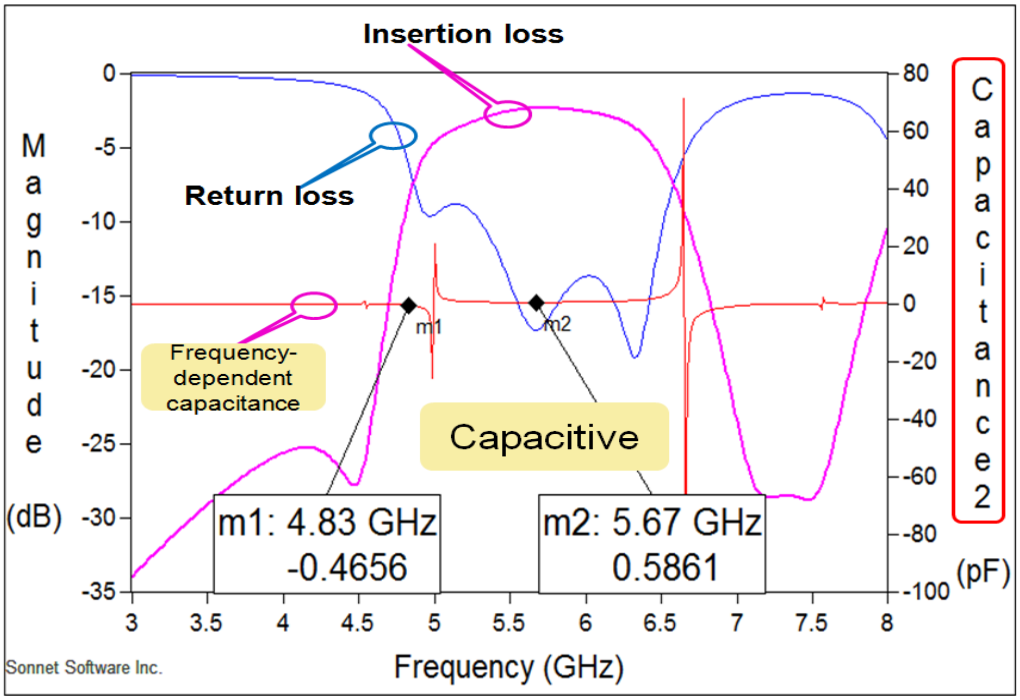

Figure 106. Filter response in terms of capacitor.

The capacitance is negative before the passband, which represents an inductive behavior. It should be noted that the passband starts or ends when the inductive region approaches the first resonant frequency or the capacitive region approaches the second resonant frequency, which is the fundamental principle of the passband creation. Since the passband is in the capacitive region and the quality factor of the capacitor is inversely proportional to the substrate loss, good insertion loss performance from the low-loss substrate will significantly degrade by using the high-loss substrate.

To avoid and minimize the high-loss substrate effect, the filter can be designed so that the passband is in the inductive region. It has been shown that the passband starts when the passive component approaches the self resonant frequency. Therefore, a capacitor can be designed in such way that the self-resonant frequencies occur at start and end of passband frequencies. For instance, a single capacitor can be used to obtain good insertion loss with wide bandwidth. As shown in Figure 107, simulation result of a capacitor realized in FR4 substrate (tanδ=0.025) shows the passband insertion loss of -0.38 dB while two notches in the return loss come from the first and second self resonance frequencies of the capacitor.

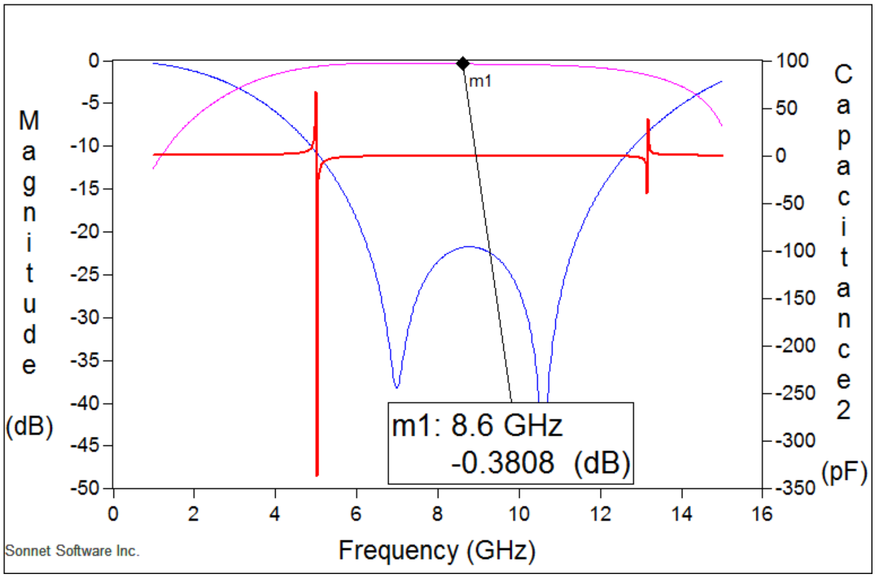

Figure 107. Wideband bandpass response using a capacitor.

The first guideline stated that the strip inductor should be avoided because it is most sensitive to the insertion loss. The major loss of the strip inductor comes from the fringing capacitance between the lines and to the ground, which also relates to the substrate loss. However, the substrate-loss effect can be eliminated by using the via as an inductor. Because the via is a vertical structure going through dielectric material, fringing capacitance can be minimized.

The concept of using the via as an inductor can be extended to the coupling between vias. If the coupling between two vias gets strong, the substrate-loss effect will be minimized since the fringing capacitance will be very small. Good insertion loss can be obtained especially at high frequency since coupling is increased as the frequency goes higher. Therefore, a passband characteristic can be obtained without using a resonator structure. This proposed idea is useful for the TSV structure which has stronger coupling between TSVs than through-hole via. Details regarding via and TSV coupling characteristics are explained in Section 6.4.

6.3 Validation using FR4 Substrate on PCB

To support the filer design method for high-loss substrate from the previous section, two bandpass filters are realized in commercially available PCB (FR4) technology. The stack-up used has two 43 μm metal layers with a single 62 mils thick FR4 substrate. The bottom metal layer is used for the ground plane so that the top metal layer is selected for the layout. Dielectric constant of 4.6 and loss tangent of 0.025 have been used for the FR4 substrate. The minimum space and line width are 6 mils, and 14 mils through-hole via with 31 mils pad has been used.

Since only one metal layer is used for layout, interdigitated capacitor [92] has been used to make the passband into the inductive region. As mention in [93], an equivalent circuit model for the interdigitated capacitor is available in commercial circuit simulator such as ADS [75]. However, the model is only valid before the first resonant frequency because multiple couplings between fingers are difficult to model at the circuit level. Therefore, full-wave simulator should be used to observe the first and second resonant frequency of the interdigitated capacitor. The basic design guideline is that the bandwidth between the first and the second resonant frequency can be increased or decreased by reducing or increasing the number of fingers. In addition, if the number of coupled fingers is increased, the center frequency can be shifted to the lower frequency.

Figure 108 shows the physical dimension of the interdigitated capacitor and its measurement correlation result with the simulation. The measured ultra-wide band FR4 filter is centered at 7.5 GHz with **3 dB bandwidth of 8 GHz**. **The measured insertion loss was -0.285 dB** while the return loss was better than -19 dB. Moreover, the size of the filter is only 5.029 mm x 1.067 mm. Therefore, the measurement result clearly verifies that the effect of the dielectric loss can be eliminated if the passband is in inductive region.

The concept of using the via as an inductor has also been verified through the second design. Figure 109 represents the proof-of-concept FR4 filter that is realized by using interdigitated capacitor and two vias. The bandwidth of the filter has been controlled by placing two inductors using through-hole vias. **The measured insertion loss at 4.2 GHz was -0.45 dB**. Considering the measured insertion losses for 18 mils wide and 150 mils long transmission line are -0.235 dB @ 1 GHz and -1.87 dB @ 4.2 GHz, the passband response is fairly decent. The VNA screen shots of both filters are shown in Appendix.

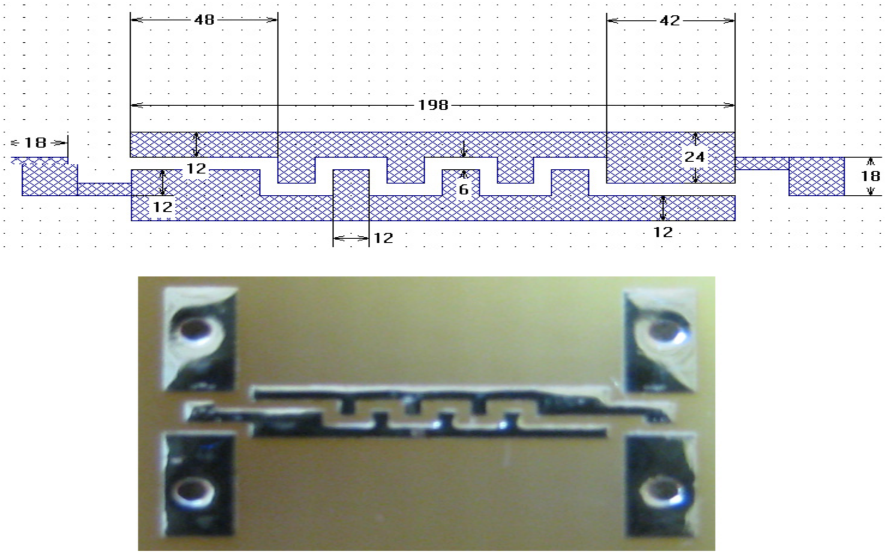

(a)

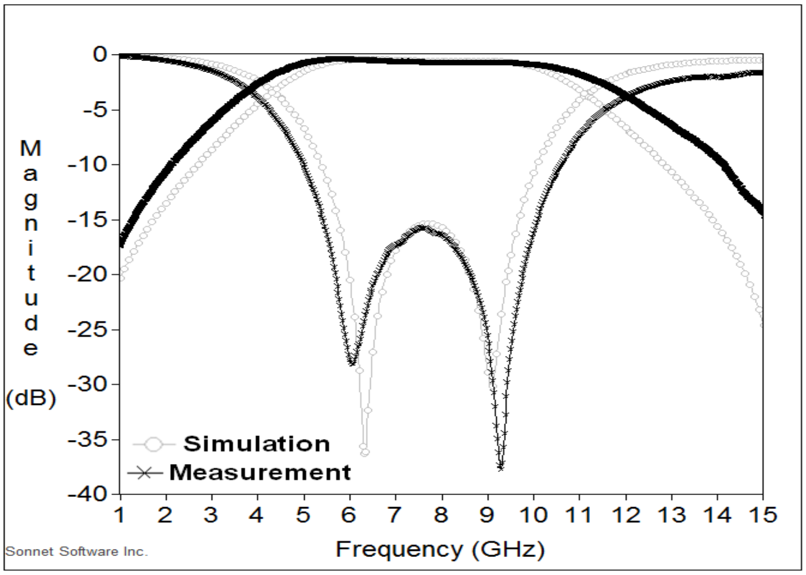

(b)

Figure 108. (a) Physical layout and (b) measured result of UWB FR4 filter.

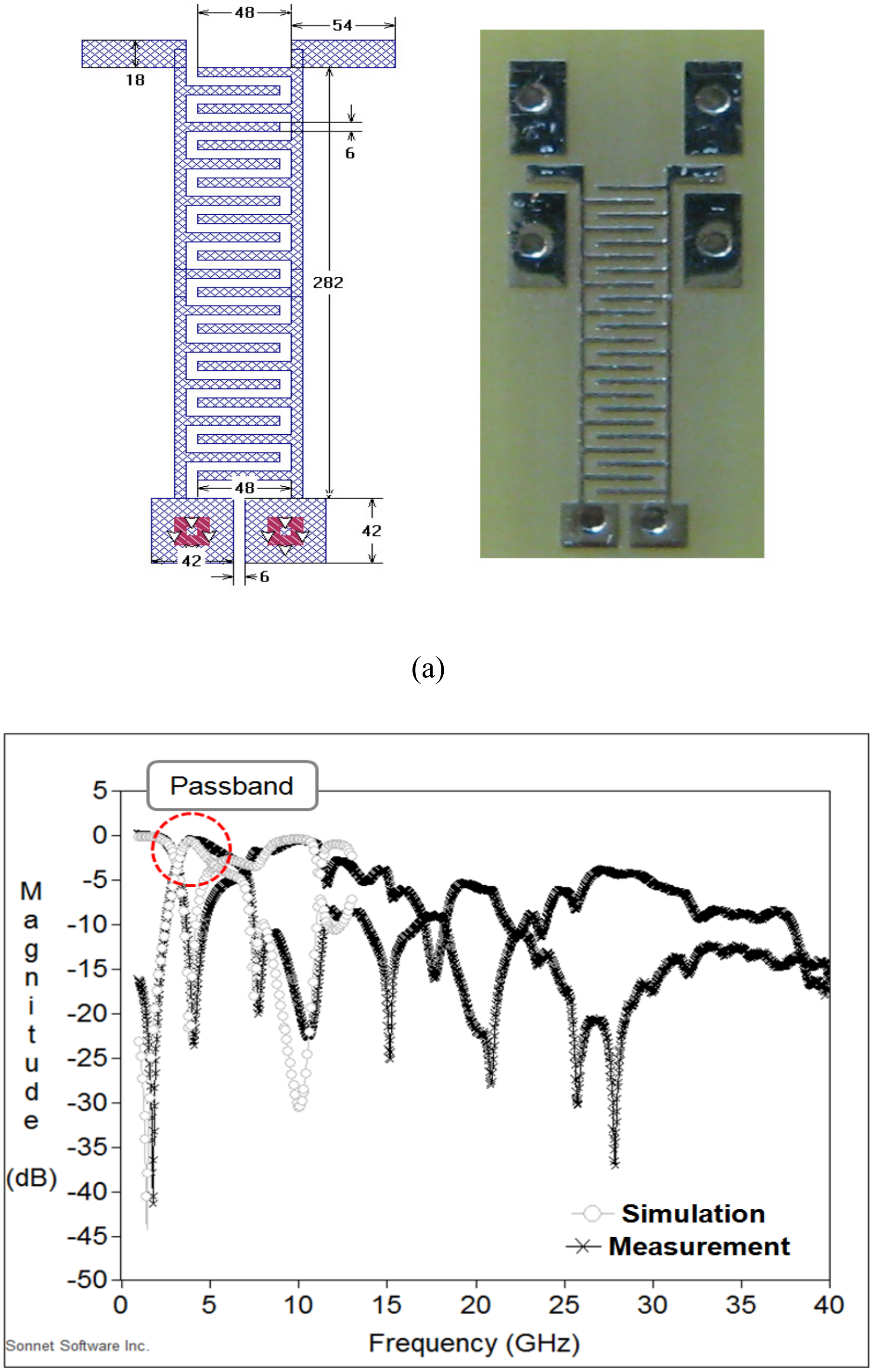

(a)

(b)

Figure 109. (a) Physical layout and (b) measured result of FR4 bandpass filter.

6.4 RF Characteristics of Through-Silicon Via (TSV)

The two design guidelines can be applied to silicon interposer with two additional advantages. The first advantage is a miniaturization effect that resulted from high dielectric constant in silicon interposer. The other advantage is different RF characteristic in through-silicon via (TSV), which shows higher coupling between TSVs than through-hole via based on low-loss organic substrate.

The electrical modeling of TSV requires careful consideration of its complex electrical behavior because of the insulating oxide liner around the conductor. Using accurate TSV modeling method and tool [94], RF characteristics of the TSV has been compared with the via in organic substrate. The simulated via has a radius of 15 μm, a thickness of 100 μm, and distance between two vias (pitch) of 50 μm. Figure 110 shows the geometry of the simulated vias where from P1 to P4 represents the port location, and Figure 111 represents S-parameter responses from 1 GHz to 100 GHz. Oxide thickness of 0.7 μm and 10 S/m silicon conductivity are used, and dielectric constant of silicon and silicon dioxide used are 11.9 and 3.9, respectively.

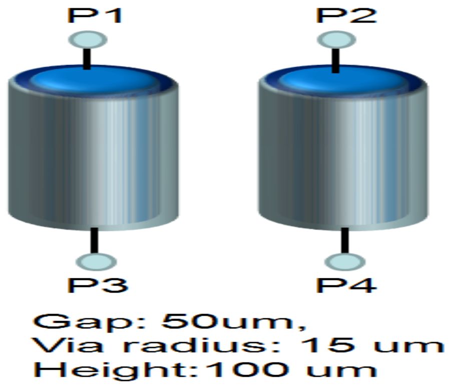

Figure 110. Geometry of simulated vias.

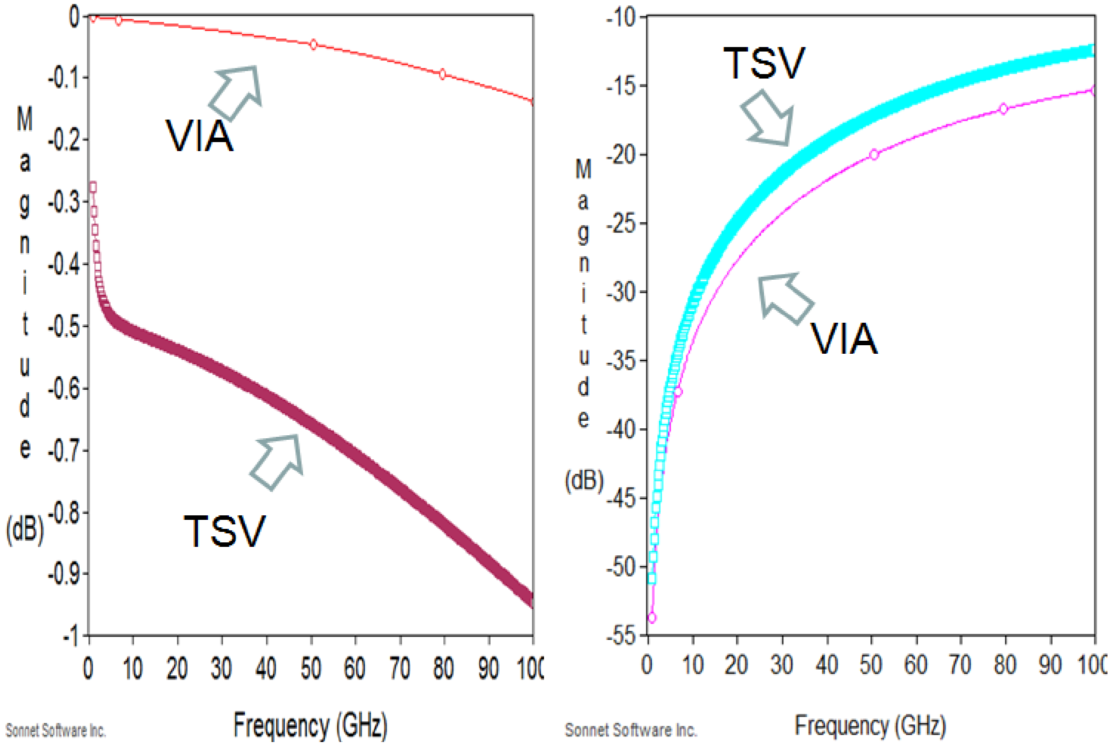

(a) (b)

Figure 111. (a) S31 (IL) and (b) S21 (NEXT) of conventional vias and TSVs.

The S31 (the signal integrity through the via) shows that the conventional via based on low-loss organic substrate has better signal performance than TSV because of the oxide thickness and silicon conductivity [94]. On the other hand, S21 (the coupling between vias: near end cross talk) of TSV always lies above the S21 of the conventional via. That is, TSV has stronger coupling than the conventional vias, and this coupling characteristic is increased as the frequency goes higher. To quantify what cause the difference, the frequency-dependent circuit parameter of two parallel TSVs is shown in Figure 112.

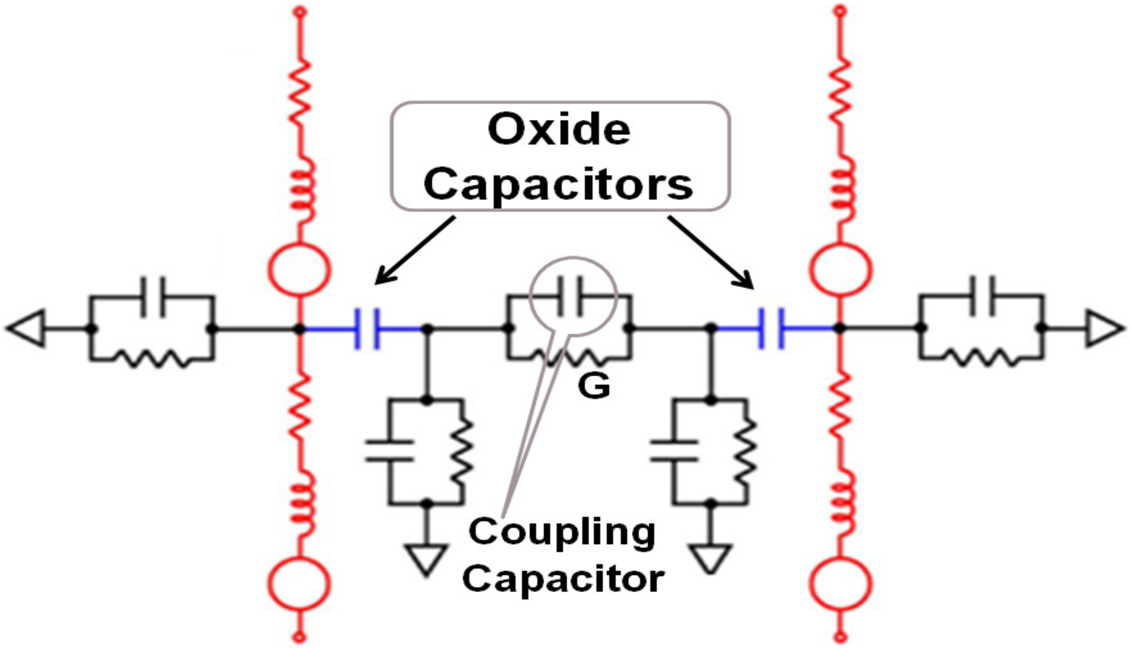

Figure 112. Model equivalent circuit of two TSVs [94].

For the silicon substrate, there are oxide capacitors between two TSV equivalent circuits. It was shown that this oxide capacitance is important to model the TSV accurately. These oxide capacitances will decrease the coupling capacitance between two TSVs because they are in series connection. Moreover, the capacitance of the frequency-dependent coupling capacitor is significantly decreased as the frequency increases. Therefore, the oxide capacitance is not the source of coupling enhancement because the coupling impedance is increased.

Since the TSV behaves differently compared to the via because of the oxide thickness and silicon conductivity, the effect of oxide thickness and silicon conductivity on the coupling has been studied. The geometry of TSV remains the same while the oxide thickness of 0.1 and 1 μm and the silicon conductivity of 1 and 100 S/m have been simulated. The simulation results from 1 to 10 GHz with different oxide thickness and silicon conductivity are shown in Figure 113: Blue line is the reference, pink line is the oxide thickness of 0.1 µm, green line is the oxide thickness of 1 µm, black line is the silicon conductivity of 100 S/m, and cyan line is the silicon conductivity of 1 S/m.

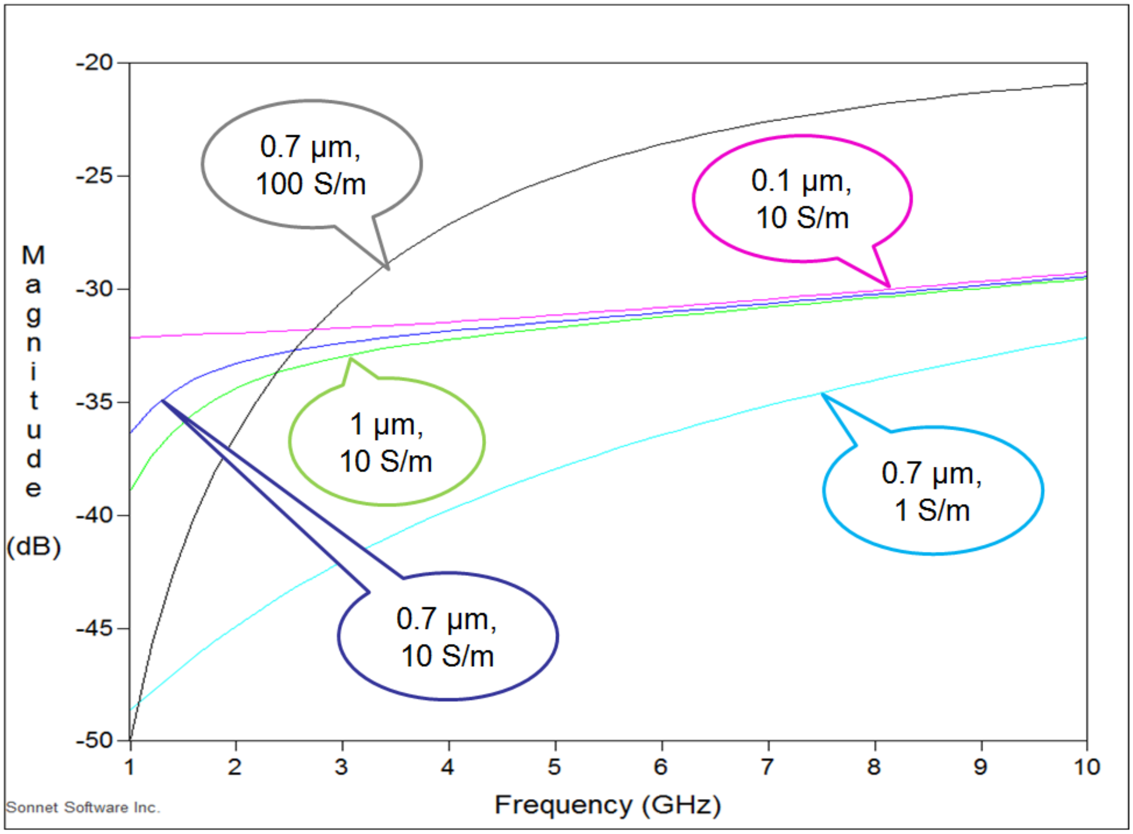

Figure 113. TSV coupling by varying oxide thickness and silicon conductivity.

As it expected, the different oxide thicknesses have little effect on the coupling. The thinner oxide thickness provides higher coupling because the oxide capacitance will be greater than the thicker oxide thickness, which will contribute to higher coupling capacitance. In contrast to the oxide thickness, the silicon conductivity mainly affects the coupling. The silicon conductivity is determined by the level of doping. The low-conductivity substrate has similar characteristics to organic substrate while high-conductivity silicon substrate has considerable substrate coupling [94]. Hence, the coupling impedance of TSV is smaller than the conventional via because of the silicon conductivity. The coupling can be even stronger if the pitch becomes smaller. The example of TSV based filter is discussed in the next section.

6.5 Filter Design in Silicon Interposer using TSV

Ultra wide-band filter based on 'passband in inductive region' design guideline can be applied to silicon interposer as well. Since silicon substrate has higher dielectric constant than FR4 substrate, the size of capacitor can be further miniaturized. As shown in Figure 114, the simulation result of 1.88 mm x 0.914 mm planar capacitor shows 10 GHz 3dB bandwidth and good insertion loss in silicon interposer.

By using TSV coupling characteristics, a highpass filter can be realized in silicon interposer. Since the coupling in TSV becomes stronger as the frequency goes higher, the cutoff frequency (-3 dB coupling point) can be obtained from increasing the coupling by reducing the pitch between TSVs and adding a capacitor between TSV. To demonstrate the highpass filter using TSV, two highpass filters have been designed using 100 μm diameter TSVs with 25 μm pitch as shown in Figure 115. The cutoff frequency can be controlled by changing the capacitance value or TSV pitch. Both highpass filters show less than 0.2 dB insertion loss after the cutoff frequency.

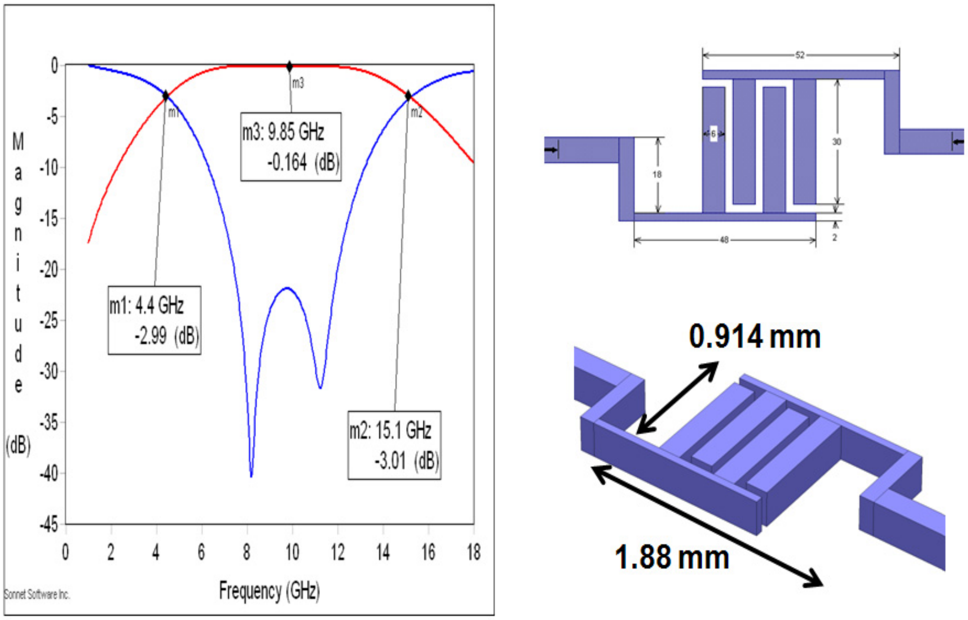

(a) (b)

Figure 114. Simulation result of UWB filter in silicon interposer. (a) Filter response and (b) physical layout.

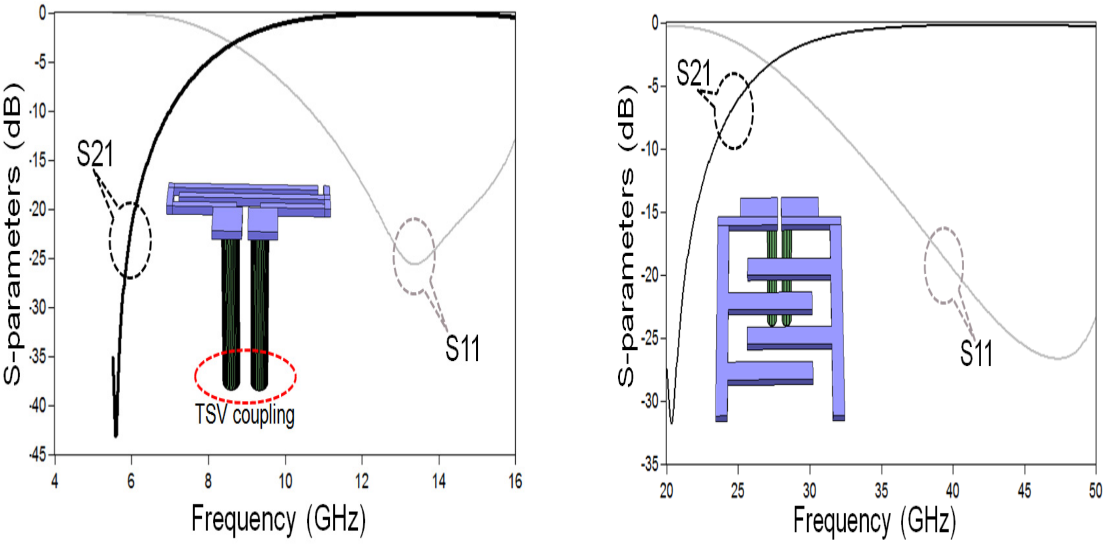

(a) (b)

Figure 115. Highpass filter using TSV coupling. (a) 8.5 GHz cutoff frequency (b) 27 GHz cutoff frequency.

The barrier of low Q inductor in silicon can be avoided by using a novel filter schematic, which the filter performance does not heavily rely on Q of the inductor. Figure 116 represents a high-rejection highpass filter by additional capacitor and inductors. The dimension of TSV used for the simulation is a radius of 15 µm with thickness of 100 µm and 50 µm pitch.

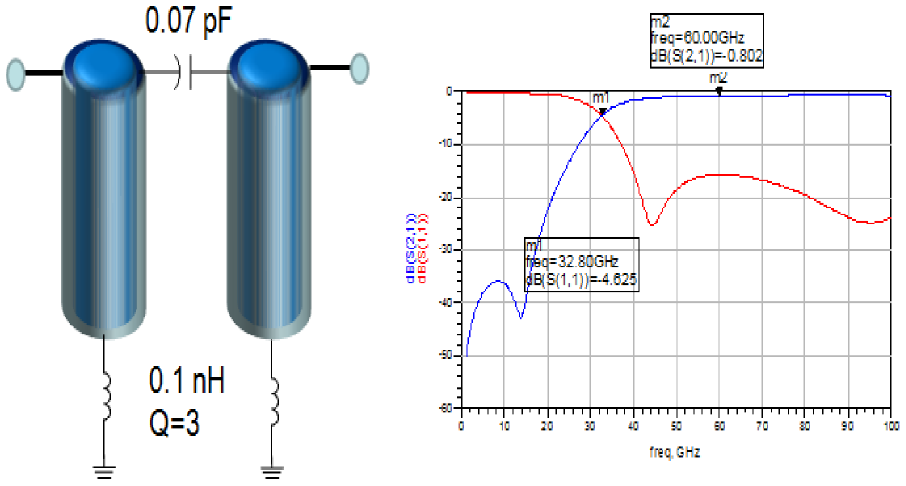

Figure 116. High-rejection highpass filter by TSV.

As shown in Figure 116, a good highpass filter response is obtained by adding a small capacitor between TSVs while low Q inductors are attached to the bottom of TSVs. The cutoff frequency is also adjustable by tweaking the capacitor between TSVs. In addition, the insertion loss in the passband region is not much affected by the Q of the inductors since the passband relies on the coupling between two TSVs.

Beside of the coupling characteristics of TSV, this proposed method is to use the TSV as a passive element such as an inductor. Since the major difficulty of filter realization in the silicon substrate is the low Q inductor performance, the filter performance especially insertion loss can be improved by applying TSVs to millimeter-wave region (>

25 GHz) where a small inductance value is required for the filter response. As shown in Figure 117, a preliminary bandpass filter response is obtained by grounding the bottom of TSVs and connecting a capacitor between TSVs.

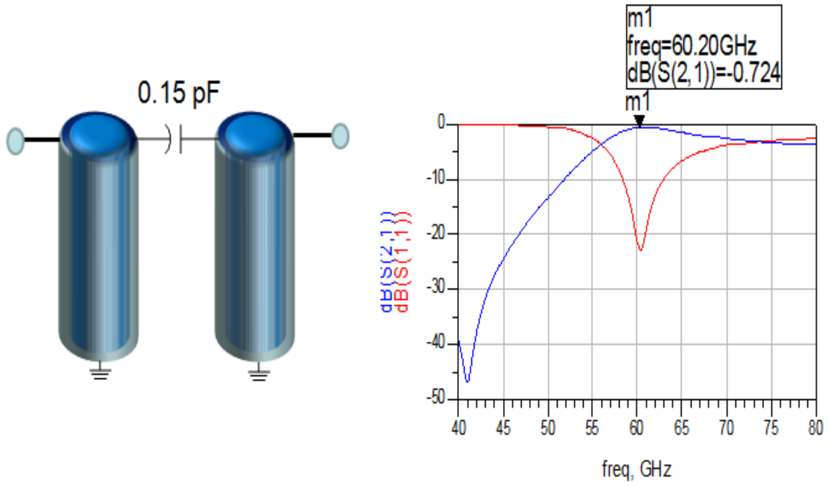

Figure 117. Bandpass response in 60 GHz by TSV.

6.6 Summary

This chapter presented filter design method for the high-loss substrate such as FR4 and silicon interposer. The effect of the substrate loss for insertion loss has been discussed and avoiding substrate-loss effect has been proposed by making the passband in the inductive region. The proposed idea can be extended to silicon interposer with TSV technology. As proof of concept, ultra wideband bandpass and typical bandpass filters have been realized in high-loss FR4 substrate. Measured insertion loss showed extremely good passband responses (< 0.3 dB @ 6 GHz and <0.7 dB @ 10 GHz), which verified that the proposed method can be used for the high-loss substrate.

Silicon interposer and TSV technology have had so much attention. To apply the proposed method to the silicon technology, the unique RF characteristic of TSV has been compared with the via in organic substrate. Finally, the simulation result of TSV based filter has been shown. The fabrication of TSV based filter and development of a new high-rejection filter topology based on the proposed method are recommended as a part of the future work.

CHAPTER 7

CONCLUSIONS

Wireless application has evolved dramatically due to the demand for low cost, compact size, and high performance solutions. Increasing system complexity has brought the need for higher levels of integration in RF front-end module. The passive component occupies most of the area in wireless products. Therefore, system on package (SoP) has been used as a solution for supporting the convergence of multiple RF front-end components by providing more functionality in the package through integration of passive components such as inductors, capacitors, and resistors

The goal of the research in this dissertation was to realize high-performance passive circuits along with developing techniques for system-on-package integration using ultra-thin advanced polymers called RXP (Rogers experimental polymer), material characterization, and filter design for high-loss substrate up to millimeter-wave frequency applications. In Chapter 2, the material characterization method for extracting organic and inorganic substrate properties has been presented. Using the extracted material property, high-performance miniaturized bandpass filter, dual-band filter, and duplexer were designed from WLAN to millimeter-wave frequency and their performance was verified through measurement from Chapter 3 to Chapter 5. For the high-loss substrate such as FR4 and silicon interposer, a new method to design passive circuits has been presented.

In conclusion, the new ultra-thin RXP substrate is a promising solution for next generation wireless application. Section 7.1 presents the contributions in this dissertation, and future work for millimeter-wave design using RXP and improved TSV filter is addressed in Section 7.2. The final section shows published papers and inventions.

7.1 Contributions

The contributions of this research are summarized as follows:

Major Contributions:

- Efficient and accurate material characterization method for frequency-dependent material property extraction
- Extraction of ultra-thin RXP material properties from 1 GHz to 110 GHz for the first time
- Development of high-rejection bandpass filter topology for narrow and wide band applications and realization of the world's smallest high-rejection bandpass filters in RXP substrate
- A new method of designing filter in silicon interposer with TSV

Minor Contributions:

- A new capacitor design called 3D stitched capacitor to provide balanced shunt parasitics and layout symmetry
- Design of lumped-element dual-band bandpass filter using the proposed single bandpass filter topology for the dual-band module application

- Realization of miniaturized high-rejection WLAN duplexer for chip-last embedded technology
- Design of lumped-element passive circuits for millimeter-wave frequency

7.2 Future Work

Passive circuits based on lumped-element for millimeter-wave application has been presented in Chapter 5. To further validate the proposed idea of using lumped-elements at millimeter-wave frequency, two-port inductor and capacitor model can be designed so that the inductance and capacitance along with the quality factor can be measured. Then, bandpass filters, dual-band filters, and duplexers can be designed with much better accuracy by optimizing the process. To minimize the measurement parasitic, the probe pitch of less than 250 μm is recommended.

Filter design method for high-loss substrate can be extended to high-performance filter for the silicon interposer using TSV technology. The proposed method in Chapter 6 showed a way to achieve good passband characteristics, which was not possible using the conventional filter topology. The capacitor that was used as an inductor for the passband in inductive region technique can be miniaturized using high dielectric constant from silicon property. In addition, highpass filter designs using via or TSV coupling needs to be verified by measurement.

7.3 Publications

In the course of the dissertation research, the following journal articles, conference papers, and invention disclosures have been published.

7.3.1 Refereed Journal Articles

- **Seunghyun Hwang**, Sunghwan Min, Venkatesan Venkatakrishnan, Madhavan Swaminathan, Hunter Chan, Fuhan Liu, Venky Sundaram, Scott Kennedy, Dirk Baars, Benjamin Lacroix, Yuan Li, and John Papapolymerou, "Characterization of next generation thin low-k and low-loss organic dielectrics from 1 to 110 GHz", *IEEE Transactions on Advanced Packaging*, vol. 33, no. 1, pp. 180-188, Aug. 2009
- **Seunghyun Hwang**, Sunghwan Min, Madhavan Swaminathan, Venky Sundaram, and Rao Tummala, "Thin-film high rejection filter integration in low-loss organic substrate", will be published in *IEEE Transactions on Component, Packaging, and Manufacturing Technology*, 2011
- **Seunghyun Hwang,** Madhavan Swaminathan and Ki Jin Han, "Filter design techniques for high-loss substrate including silicon interposer with through-silicon via (TSV)", to be submitted to *IEEE Microwave and Wireless Components letters*
- **Seunghyun Hwang**, and Madhavan Swaminathan, "Miniaturized Lumped-Element Dual-Band Bandpass Filters from WLAN to Millimeter-Wave Applications", to be submitted to *IEEE Transactions on Microwave Theory and Techniques*

7.3.2 Conference Papers

- **Seunghyun Hwang**, Madhavan Swaminathan, and Venkatesan Venkatakrishnan, "Extraction of material properties for low-k and low-loss dielectric using cavity resonator and efficient finite difference solver up to 40GHz", *Electrical Design of Advanced Packaging and Systems,* pp. 53-56, Korea, Dec. 2008
- Sunghwan Min, **Seunghyun Hwang**, Daehyun Chung, Madhavan Swaminathan, Vivek Sridharan, Hunter Chan, Fuhan Liu, Venky Sundaram, and Rao R. Tummala*,* "Filter integration on ultra thin organic substrate via 3D stitched capacitor", *Electrical Design of Advanced Packaging and Systems*, pp. 1-4, Hong Kong, Dec. 2009
- **Seunghyun Hwang**, Sunghwan Min, Hunter Chan, Venky Sundaram, and Madhavan Swaminathan*,* "A compact third-order 5 GHz bandpass filter with enhanced stopband characteristics in ultra thin organic substrate", *Radio and Wireless Symposium*, pp. 452-455, New Orleans, Jan. 2010
- Madhavan Swaminathan, **Seunghyun Hwang**, and Nevin Altunyurt*,* "RF system integration and miniaturization using advanced polymers", *International Microwave Symposium*, pp 1708-1711, Anaheim, May 2010
- Madhavan Swaminathan, Nevin Altunyurt**,** and **Seunghyun Hwang**, "Advanced polymers for advanced RF packaging applications", *European Microwave Conference*, pp 695-698, Paris, Sept. 2010
- Vivek Sridharan, Sunghwan Min, Venky Sundaram, Vijay Sukumaran, **Seunghyun Hwang**, Hunter Chan, Fuhan Liu, Christian Nopper, and Rao la, "Design and fabrication of bandpass filters in glass interposer with through-

package-vias", Electronic Components and Technology Conference , pp. 530-535, Las Vegas, June 2010

7.3.3 Invention Disclosure

- Sunghwan Min, **Seunghyun Hwang**, Daehyun Chung, and Madhavan Swaminathan, "Stitched capacitor for filter integration", GTRC ID: 4877, July 2009, Provisional Application filed by Georgia Tech

APPENDIX

Figure 118 shows the VNA screen shots of filter response demonstrating good insertion loss performance on FR4 substrate.

```
 1:   3.769000 GHz  -3.0716 dB
 2:  12.037000 GHz  -3.9751 dB
 3:   5.680000 GHz -0.28551 dB
 4:   7.708000 GHz -0.59176 dB
> 5:  9.580000 GHz -0.74889 dB
```

(a)

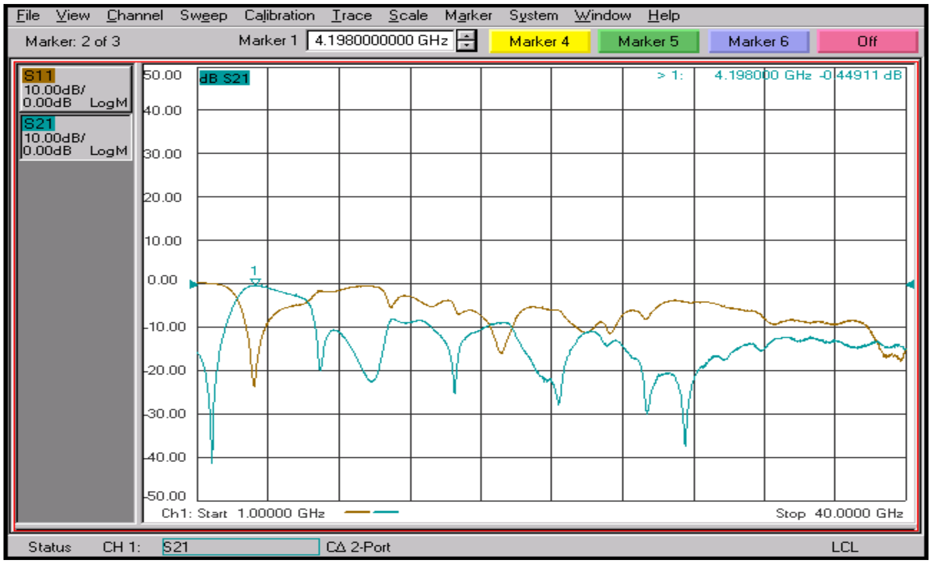

```
> 1:  4.198000 GHz -0.44911 dB
```

(b)

Figure 118. VNA screen shots of (a) UWB and (b) via as an inductor FR4 filters.

REFERENCES

[1] R. R. Tummala, “Moore's law meets its match (system-on-package),” *Spectrum, IEEE,* vol. 43, no. 6, pp. 44-49, 2006.

[2] GigaCircuits. "http://www.gigacircuits.com/technology.html," 24 Oct. 2010.

[3] R. Tummala, and M. Swaminathan, *Introduction to System-on-Package (SOP)*: McGraw-Hill, 2008.

[4] R. Tummala, and L. Joy, “Gigabit wireless: system-on-a-package technology,” *IEEE Proceedings,* vol. 92, no. 2, pp. 376-387, Feb 2004.

[5] "Packaging Research Center," 10 Sept. 2010.

[6] M. Swaminathan, A. Bavisi, W. Yun, V. Sundaram, V. Govind, and P. Monajemi, “Design and fabrication of integrated RF modules in liquid crystalline polymer (LCP) substrates,” in IEEE Indust. Elect. Society Conf., 2005, pp. 6.

[7] J. v. Beeck, M. v. Delden, A. Jansman, A. Boogaard, A. Kemmeren, N. Pulsford, and A. d. Dekker, “The integration of RF passives using thin-technology on high-ohmic Si in combination with thick-film interconnect,” in Int. Microelectronics and Packaging Soc. Conf., Baltimore, Oct 2001, pp. 467-470.

[8] W. Yun, A. Bavisi, V. Sundaram, M. Swaminathan, and E. Engin, “3D integration and characterization of high Q passives on multilayer liquid crystalline polymer (M-LCP) based substrate,” in Asia-Pacific Microwave Conf., Dec. 2005, pp. 4.

[9] I-Micronews. "http://www.i-micronews.com/analysis/Is-time-thin-film-IPDs,3504.html," 24 Oct. 2010.

[10] W. Yun, V. Sundaram, and M. Swaminathan, “High-Q embedded passives on large panel multilayer liquid crystalline polymer-based substrate ” *IEEE Trans. Adv. Packag.,* vol. 30, no. 3, pp. 580-591, Aug. 2007.

[11] L. Yo-Shen, L. Chien-Chang, L. Ko-Mai, and C. Chun Hsiung, “Design of an LTCC tri-band transceiver module for GPRS mobile applications,” *IEEE Trans. Microwave Theory Tech.,* vol. 52, no. 12, pp. 2718-2724, 2004.

[12] L. Jong-Hoon, G. DeJean, S. Sarkar, S. Pinel, L. Kyutae, J. Papapolymerou, J. Laskar, and M. M. Tentzeris, “Highly integrated millimeter-wave passive components using 3-D LTCC system-on-package (SOP) technology,” *IEEE Trans. Microwave Theory Tech.,* vol. 53, no. 6, pp. 2220-2229, 2005.

[13] W. Gangqiang, E. C. Folk, F. Barlow, and A. Elshabini, “Fabrication of microvias for multilayer LTCC substrates,” *Electronics Packaging Manufacturing, IEEE Transactions on,* vol. 29, no. 1, pp. 32-41, 2006.

[14] B. Yuan, W. Yu, H. Sun, and X. Lv, “LTCC band pass filter for wireless applications ” in IEEE Internat. Symp. Microw. Ant. Prop. for Wireless Communications 2009, pp. 470-472.

[15] C.-W. Tang, and H.-C. Hsu, “Development of multilayered bandpass filters with multiple transmission zeros using open-stub/short-stub/serial semilumped resonators ” *IEEE Trans. Microwave Theory Tech.,* vol. 58, no. 3, pp. 624-634, March 2010.

[16] M.-C. Wu, and S.-J. Chung, “A small SiP module using LTCC 3D circuitry for dual band WLAN 802.11 a/b/g front-end solution,” in IEEE Silicon Monol. Integrated Circuits Jan. 2006, pp. 4.

[17] K.-B. Lee, and J.-Y. Lee, “5.2GHz band 2nd-order band-pass filter using LTCC multi-layer technology,” in Asia-Pacific Microwave Conf., Dec. 2005, pp. 4.

[18] W. Yu, B. Yuan, and H. Sun, “A compact quasi-lumped LTCC band pass filter for C-band wireless application,” in IEEE Internat. Conf. Microw. Millim. Wave Tech. , 2008, pp. 1488-1490.

[19] Y. H. Cho, D. Y. Jung, Y. C. Lee, J. W. Lee, M. S. Song, E.-S. Nam, S. Kang, and C. S. Park, “A fully embedded LTCC multilayer BPF for 3-D integration of 40-GHz radio,” *IEEE Trans. Adv. Packag.,* vol. 30, no. 3, pp. 521-525, Aug. 2007.

[20] L. K. Yeung, and K.-L. Wu, “A compact second-order LTCC bandpass filter with two finite transmission zeros,” *IEEE Trans. Microwave Theory Tech.,* vol. 51, no. 2, pp. 337-341, Feb. 2003.

[21] C.-W. Tang, “Harmonic-suppression LTCC filter with the step-impedance quarter-wavelength open stub,” *IEEE Trans. Microwave Theory Tech.,* vol. 52, no. 2, pp. 617-624, Feb. 2004.

[22] Y.-H. Jeng, S.-F. R. Chang, and H.-K. Lin, “A high stopband-rejection LTCC filter with multiple transmission zeros,” *IEEE Trans. Microwave Theory Tech.,* vol. 54, no. 2, pp. 633-638, Feb. 2006.

[23] J.-H. Lee, N. Kidera, G. DeJean, S. Pinel, J. Laskar, and M. M. Tentzeris, “A V-band front-end with 3-D integrated cavity filters/duplexers and antenna in LTCC technologies,” *IEEE Trans. Microwave Theory Tech.,* vol. 54, no. 7, pp. 2925-2936, July 2006.

[24] D. C. Thompson, O. Tantot, H. Jallageas, G. E. Ponchak, M. M. Tentzeris, and J. Papapolymerou, “Characterization of liquid crystal polymer (LCP) material and

transmission lines on LCP substrates from 30 to 110 GHz," *IEEE Trans. Microwave Theory Tech.,* vol. 52, no. 4, pp. 1343-1352, April 2004.

[25] S. Dalmia, F. Ayazi, M. Swaminathan, M. Sung Hwan, L. Seock Hee, K. Woopoung, K. Dongsu, S. Bhattacharya, V. Sundaram, G. White, and R. Tummala, "Design of inductors in organic substrates for 1-3 GHz wireless applications," in Microwave Symposium Digest, 2002 IEEE MTT-S International, 2002, pp. 1405-1408.

[26] S. Dalmia, L. Carastro, R. Fathima, V. Govind, J. Dekosky, S. Lapushin, R. Wu, B. Bayruns, and G. White, "A compact dual band 802.11n front-end module for MIMO applications using multi-layer organic technology," in Microwave Symposium Digest, 2008 IEEE MTT-S International, 2008, pp. 89-92.

[27] S. Dalmia, J. M. Hobbs, V. Sundaram, M. Swaminathan, L. Seock Hee, F. Ayazi, G. White, and S. Bhattacharya, "Design and optimization of high Q RF passives on SOP-based organic substrates," in Electronic Components and Technology Conference, 2002. Proceedings. 52nd, 2002, pp. 495-503.

[28] S. Dalmia, V. Sundaram, G. White, and M. Swaminathan, "Liquid crystalline polymer (LCP) based lumped-element bandpass filters for multiple wireless applications," in Microwave Symposium Digest, 2004 IEEE MTT-S International, 2004, pp. 1991-1994 Vol.3.

[29] J. Dekosky, S. Lapushin, S. Dalmia, W. Czakon, and G. White, "The Stacking of Integrated Passive Devices, Substrates, and RFICs to make ultra-thin modules using Organic Liquid Crystalline Polymer (LCP) Technology," in Microwave Symposium Digest, 2006. IEEE MTT-S International, 2006, pp. 1257-1260.

[30] V. Govind, P. Monajemi, L. Carastro, S. Lapushin, C. Russell, S. Dalmia, J. Vickers, V. Sundaram, and G. White, "Design of Novel Highly Integrated Passive Devices for Digital Broadcasting Satellite / 802.11 Home Networking Solution in Liquid Crystal Polymer (LCP) Based Organic Substrates," in Microwave Symposium Digest, 2006. IEEE MTT-S International, 2006, pp. 1157-1160.

[31] S. Mukherjee, S. Dalmia, B. Mutnury, and M. Swaminathan, "Layout-level synthesis of RF bandpass filter on organic substrates for wi-fi applications," in Microwave Conference, 2004. 34th European, 2004, pp. 1377-1380.

[32] S. Mukherjee, M. Swaminathan, and S. Dalmia, "Synthesis and diagnosis of RF filters in liquid crystalline polymer (LCP) substrate," in Microwave Symposium Digest, 2005 IEEE MTT-S International, 2005, pp. 4 pp.

[33] S. Dalmia, V. Govind, J. Dekosky, V. Sundaram, G. White, and M. Swaminathan, "Design and implementations of RF systems and sub-systems in LCP-type

multilayer technology," in Electronic Components and Technology Conference, 2006. Proceedings. 56th, 2006, pp. 5 pp.

[34] V. Govind, S. Dalmia, J. Choi, and M. Swaminathan, "Design and implementation of RF subsystems with multiple embedded passives in multi-layer organic substrates," in Radio and Wireless Conference, 2003. RAWCON '03. Proceedings, 2003, pp. 325-328.

[35] Y. Wansuk, V. Govind, S. Dalmia, V. Sundaram, M. Swaminathan, and G. E. White, "An integrated double balanced mixer on multilayer liquid crystalline polymer (M-LCP) based substrate," in Microwave Conference, 2005 European, 2005, pp. 4 pp.

[36] Y. Wansuk, V. Sundaram, and M. Swaminathan, "A Triple Balanced Mixer in Multi-layer Liquid Crystalline Polymer (LCP) Substrate," in Electronic Components and Technology Conference, 2007. ECTC '07. Proceedings. 57th, 2007, pp. 2000-2005.

[37] MyDigitalLife. "http://www.mydigitallife.info/2009/11/10/samsung-unveiled-ultra-slim-nand-flash-memory-chip-for-smartphone-market/," 27 Oct. 2010.

[38] D. Athreya, V. Sundaram, M. Iyer, and R. Tummala, "Ultra high Q embedded inductors in highly miniaturized family of low loss organic substrates," in IEEE Elect. Compon. Technol. Conf., 2008, pp. 2073-2080.

[39] S. Hwang, S. Min, H. Chan, V. Sundaram, and M. Swaminathan, "A compact third-order 5 GHz bandpass filter with enhanced stopband characteristics in ultra thin organic substrate," in IEEE Radio and Wireless Symp., New Orleans, LA, Jan. 2010.

[40] S. Hwang, S. Min, M. Swaminathan, V. Venkatakrishnan, H. Chan, F. Liu, and V. Sundaram, "Characterization of next generation thin low-k and low-loss organic dielectrics from 1 to 110 GHz," *IEEE Trans. Adv. Packag.,* vol. 33, no. 1, pp. 180-188, Feb. 2010.

[41] S. Hwang, M. Swaminathan, and V. Venkatakrishnan, "Extraction of material properties for low-K and low-loss dielectrics using cavity resonator and efficient finite difference solver up to 40GHz," in IEEE Elect. Design Adv. Packag. Syst. Symp., Seoul, S. Korea, pp. 53-56.

[42] G. Krishnan, F. Liu, V. Sundaram, R. Pucha, S. Kennedy, and D. Baars, "High performance organic dielectrics and high density substrates for next generation system on a package (SOP) technology," in IEEE Elect. Compon. Technol. Conf., 2008, pp. 2101-2104.

[43] F. Liu, V. Sundaram, S. Min, V. Sridharan, H. Chan, N. Kumbhat, B.-W. Lee, R. Tummala, D. Baars, S. Kennedy, and S. Paul, "Chip-last embedded actives and passives in thin organic package for 1-110 GHz multi-band applications," in Electronic Components and Technology Conference (ECTC), 2010 Proceedings 60th, 2010, pp. 758-763.

[44] S. Min, S. Hwang, D. Chung, M. Swaminathan, V. Sridharan, H. Chan, F. Liu, V. Sundaram, and R. R. Tummala, "Filter integration in ultra thin organic substrate via 3D stitched capacitor," in IEEE Elect. Design Adv. Packag. Syst. Symp., Shatin, Hong Kong, Dec. 2009.

[45] F. Liu, V. Sundaram, H. Chan, G. Krishnan, S. Jintang, J. Dobrick, J. Neill, D. Baars, S. Kennedy, and R. Tummala, "Ultra-high density, thin core and low loss organic system-on-package (SOP) substrate technology for mobile applications," in Electronic Components and Technology Conference, 2009. ECTC 2009. 59th, 2009, pp. 612-617.

[46] A. Deutsch, T.-M. Winkel, G. V. Kopcsay, C. W. Surovic, B. J. Rubin, G. A. Katopis, and B. J. Chamberlin, "Extraction of $\varepsilon_r(f)$ and $\tan\delta(f)$ for printed circuit board insulators up to 30 GHz using the short-pulse propagation technique," *IEEE Trans. Adv. Packag.,* vol. 28, no. 1, pp. 4-12, Feb. 2005.

[47] J. Baker-Jarvis, R. G. Geyer, J. H. Grosvenor, Jr. , M. D. Janezic, C. A. Jones, B. Riddle, C. M. Weil, and J. Krupka, "Dielectric characterization of low-loss materials a comparison of techniques," *IEEE Trans. Dielect. Elect. Insulation,* vol. 5, no. 4, pp. 571-577, Aug. 1998.

[48] X. Fang, D. Linton, C. Walker, and B. Collins, "A tunable split resonator method for nondestructive permittivity characterization," *IEEE Trans. on Instrument. Measurement,* vol. 53, no. 6, pp. 1473-1478, Dec. 2004.

[49] L. S. Napoli, and J. J. Hughes, "A simple technique for the accurate determination of the microwave dielectric constant for microwave integrated circuit substrates (Correspondence)," *IEEE Trans. Microwave Theory Tech.,* vol. 19, no. 7, pp. 664-665, July 1971.

[50] X. Fang, D. Linton, C. Walker, and B. Collins, "Dielectric constant characterization using a numerical method for the microstrip ring resonator," *Microw. Optical Tech. lett.,* vol. 41, no. 1, pp. 14-17, April 2004.

[51] L. Chen, V. V. Varadan, C. K. Ong, and C. P. Neo, *Microwave Electronics: Measurement and Materials Characterization*, pp. 26, 2004.

[52] A. E. Engin, A. Tambawala, M. Swaminathan, S. Bhattacharya, P. Pramanik, and K. Yamazaki, "Causal modeling and extraction of dielectric constant and loss

tangent for thin dielectrics," *Electromagnetic Compatibility IEEE international Symposium*, July, 2007.

[53] A. Deutsch, A. Huber, G. V. Kopcsay, B. J. Rubin, R. Hemedinger, D. Carey, and W. Becker, "Accuracy of dielectric constant measurement using the full-sheet-resonance technique," in IEEE Elect. Perform. Electron. Packag., 2002, pp. 311-314.

[54] H. Braunisch, X. Gu, A. Camacho-Bragado, and L. Tsang, "Off-chip rough-metal-surface propagation loss modeling and correlation with measurements," in IEEE Elect. Compon. Technol. Conf., 2007, pp. 785-791.

[55] X. Chen, "EM modeling of microstrip conductor losses including surface roughness effect," *IEEE Microw. Wireless Comp. Lett.,* vol. 17, no. 2, pp. 94-96, Feb. 2007.

[56] EVDO/EVDV. "http://ecee.colorado.edu/~ecen4242/evdo/evdowebpage.htm," 24 Oct. 2010.

[57] M.-C. Wu, and S.-J. Chung, "A small SiP module using LTCC 3D circuitry for dual band WLAN 802.11 a/b/g front-end solution," in Silicon Monolithic Integrated Circuits in RF Systems, 2006. Digest of Papers., 2006, pp. 4.

[58] C.-W. Tang, C.-W. Shen, and P.-J. Hsieh, "Design of low-temperature co-fired ceramic bandpass filters with modified coupled inductors," *IEEE Trans. Microwave Theory Tech.,* vol. 57, no. 1, pp. 172-179, Jan. 2009.

[59] C. W. Tang, "Design of four-ordered cross-coupled bandpass filters with low-temperature co-fired ceramic technology," *IET Microwaves, Antennas & Propagation* vol. 3, no. 3, pp. 402-409, Apr. 2009.

[60] A. Afsahi, A. Behzad, V. Magoon, and L. E. Larson, "Linearized dual-band power amplifiers with integrated baluns in 65 nm CMOS for a 2 x 2 802.11n MIMO WLAN SoC " *IEEE Journal of Solid-State Circuits,* vol. 45, no. 5, pp. 955-966, April 2010.

[61] K.-B. Lee, and J.-Y. Lee, "5.2GHz band 2nd-order band-pass filter using LTCC multi-layer technology," in Asia-Pacific Conference Proceedings Microwave Conference Proceedings (APMC), 2005, pp. 4.

[62] D. M. Pozar, *Microwave Engineering*: Wiley, 2005.

[63] M. Swaminathan, and A. E. Engin, *Power Integrity Modeling and Design for Semiconductors and Systems*, pp. 117-122: Prentice Hall, 2007.

[64] A. E. Engin, K. Bharath, and M. Swaminathan, “Multilayered Finite-Difference Method (MFDM) for modeling of package and printed circuit board planes,” *IEEE Trans. Electromagn. Compat.,* vol. 49, no. 2, pp. 441-447, May 2007.

[65] S. Groiss, “Numerische Analyse verlustbehafter Hohlraumresonatoren,” Ph.D. Dissertation, Technische Universitaet Graz, Austria, 1996.

[66] A. E. Engin, A. Tambawala, M. Swaminathan, S. Bhattacharya, P. Pramanik, and K. Yamazaki, “Dielectric constant and loss tangent characterization of thin high-k dielectric using corner-to-corner plane probing,” in IEEE Elect. Perform. Electron. Packag., 2006, pp. 29-32.

[67] B. Gustavsen, and A. Semlyen, “Rational approximation of frequency domain responses by vector fitting,” *IEEE Trans. Power Delivery,* vol. 14, no. 3, pp. 1052-1061, July 1999.

[68] J. C. Lagarias, J. A. Reeds, M. H. Wright, and P. E. Wright, “Convergence properties of the Nelder-Mead simplex method in low dimensions,” *SIAM Journal of Optimization,* vol. 9, no. 1, pp. 112-147, 1998.

[69] *Sonnet Suites V12*, North Syracuse, NY.

[70] H. W. Bode, *Network Analysis and Feedback Amplifier Design*: New York: Van Nostrand, 1945.

[71] S. Hwang, M. Swaminathan, and V. Venkatakrishnan, “Extraction of material properties for low-K and low-loss dielectrics using cavity resonator and efficient finite difference solver up to 40GHz,” in IEEE Elect. Design Adv. Packag. Syst. Symp., Seoul, S. Korea, Dec. 2008, pp. 53-56.

[72] V. Sundaram, H. Chan, F. Liu, R. Tummala, H. Roberts, S. Lamprecht, K. Matejat, A. Oezkoek, S. Kennedy, J. Dobrick, and D. Baars, “Super high density two metal layer ultra-thin organic substrates for next generation system-on-package (SOP), SiP and ultra-fine pitch flip-chip packages,” in Pan Pacific Microelectronics Symposium, Hawaii, 2009.

[73] G. L. Matthaei, L. Young, and E. M. T. Jones, *Microwave filters impedance matching networks and coupling structures*, pp. 481-485: New York:McGraw-Hill, 1980.

[74] S.-H. Min, C.-S. Seo, A. M. Yepes, C. Ward, S. Dalmia, G. White, and M. Swaminathan, “RF design methodology for design-cycle-time reduction using parameterization of embedded passives on multilayer organic substrates,” in IEEE MTT-S Int. Microwave Symp. Dig., Atlanta, Ga, June 2008, pp. 1397-1400.

[75] Agilent, *ADS (Advanced Design System) 2009.*

[76] Wireless/Networking(About.com). "http://compnetworking.about.com/od/wirelessfaqs/f/5ghz-gear.htm," 8 Feb. 2011.

[77] L.-C. Tsai, and C.-W. Hsue, “Dual-band bandpass filters using equal-length coupled-serial-shunted lines and Z-transform technique,” *IEEE Trans. Microwave Theory Tech.,* vol. 52, no. 4, pp. 1111-1117, April 2004.

[78] P. Mondal, and M. K. Mandal, “Design of Dual-Band Bandpass Filters Using Stub-Loaded Open-Loop Resonators,” *IEEE Trans. Microwave Theory Tech.,* vol. 56, no. 1, pp. 150-155, January 2008.

[79] M. Zhou, X. Tang, and F. Xiao, “Compact Dual Band Bandpass Filter Using Novel E-Type Resonators With Controllable Bandwidths,” *IEEE Microw. Wireless Comp. Lett.,* vol. 18, no. 12, pp. 779-781, December 2008.

[80] C.-M. Tsai, H.-M. Lee, and C.-C. Tsai, “Planar filter design with fully controllable second passband,” *IEEE Trans. Microwave Theory Tech.,* vol. 53, no. 11, pp. 3429-3439, November 2005.

[81] S. Sun, and L. Zhu, “Compact dual-band microstrip bandpass filter without external feeds,” *IEEE Microw. Wireless Comp. Lett.,* vol. 15, no. 10, pp. 644-646, October 2005.

[82] T.-H. Huang, H.-J. Chen, C.-S. Chang, L.-S. Chen, Y.-H. Wang, and M.-P. Houng, “A novel compact ring dual-mode filter with adjustable second-passband for dual-band applications,” *IEEE Microw. Wireless Comp. Lett.,* vol. 16, no. 6, pp. 360-362, June 2006.

[83] P. K. Singh, S. Basu, and Y.-H. Wang, “Miniature Dual-Band Filter Using Quarter Wavelength Stepped Impedance Resonators,” *IEEE Microw. Wireless Comp. Lett.,* vol. 18, no. 2, pp. 88-90, February 2008.

[84] Y.-C. Chiou, C.-Y. Wu, and J.-T. Kuo, “New Miniaturized Dual-Mode Dual-Band Ring Resonator Bandpass Filter With Microwave C-Sections,” *IEEE Microw. Wireless Comp. Lett.,* vol. 20, no. 2, pp. 67-69, February 2010.

[85] Y. Sung, “Dual-Mode Dual-Band Filter With Band Notch Structures,” *IEEE Microw. Wireless Comp. Lett.,* vol. 20, no. 2, pp. 73-75, February 2010.

[86] A. Bavisi, M. Swaminathan, and E. Mina, “Liquid Crystal Polymer-Based Planar Lumped Component Dual-Band Filters For Dual-Band WLAN Systems,” in IEEE Radio and Wireless Symp., January 2007, pp. 539-542.

[87] J.-S. Hong, and M. J. Lancaster, *Microstrip Filters for RF/microwave Applications*, 2001.

[88] ELECTROIQ. "3D roadmaps begin to converge," 24 Feb. 2011.

[89] H.-C. Bae, K.-S. Choi, Y.-S. Eom, B.-O. Lim, K.-J. J. Sung, S. Kim, Byeung-Gee, I.-S. Kang, and J.-T. Moon, "3D SiP module using TSV and novel solder bump maker " in IEEE Elect. Compon. Technol. Conf., June 2010, pp. 1637-1641.

[90] M. Koyanagi, T. Fukushima, and T. Tanaka, "High-density through silicon vias for 3-D LSIs," *Proceedings of the IEEE,* vol. 97, no. 1, pp. 49-59, 2009.

[91] C. W. Sayre, *Complete Wireless Design*, 2008.

[92] G. D. Alley, "Interdigital capacitors and their application to lumped-element microwave integrated circuits," *IEEE Trans. Microwave Theory Tech.,* vol. 18, no. 12, pp. 1028-1033, Dec. 1970.

[93] E. Pettenpaul, H. Kapusta, A. Weisgerber, H. Mampe, J. Luginsland, and I. Wolff, "CAD models of lumped elements on GaAs up to 18 GHz," *IEEE Trans. Microwave Theory Tech.,* vol. 36, no. 2, pp. 294-304, Feb. 1988.

[94] K. J. Han, M. Swaminathan, and T. Bandyopadhyay, "Electromagnetic modeling of through-silicon via (TSV) interconnections using cylindrical modal basis functions," *IEEE Trans. Adv. Packag.*, June 2010.

VITA

Seunghyun Hwang was born in New Haven, the United States. He received his B.S. degree in Electrical Engineering from University of Washington, Seattle in 2007, and the M.S. degree from the Georgia Institute of Technology, Atlanta in 2009 where he is pursuing his Ph.D. degree in the School of Electrical and Computer Engineering department.

In the spring of 2010, he trained 16 Indian engineers to be able to design and layout multilayer embedded passives. In the summer of 2010, he interned at Intel Corporation where he was involved in the investigation of signal integrity problem and the design of microwave passive components for the graphic card application. He is currently a graduate research assistant in Mixed Signal Design Group at the Georgia Institute of Technology, Atlanta. From June 2011, he will be with NVIDIA as a hardware engineer.

His research interests include RF/microwave/millimeter-wave design, high-frequency and high-speed mixed signal board/package design and modeling, material characterization, high-speed signal/power integrity, and silicon interposer with through-silicon via (TSV) technology.